AFRL-RY-WP-TR-2017-0151

THERMAL AND THERMO-MECHANICAL CHARACTERISTICS OF CRYOGENIC MICROCOOLER FOR OPTIMUM PERFORMANCE AND RELIABILITY

Bongtae Han

University of Maryland

OCTOBER 2017
Final Report

AIR FORCE RESEARCH LABORATORY
SENSORS DIRECTORATE
WRIGHT-PATTERSON AIR FORCE BASE, OH 45433-7320
AIR FORCE MATERIEL COMMAND
UNITED STATES AIR FORCE

NOTICE AND SIGNATURE PAGE

Using Government drawings, specifications, or other data included in this document for any purpose other than Government procurement does not in any way obligate the U.S. Government. The fact that the Government formulated or supplied the drawings, specifications, or other data does not license the holder or any other person or corporation; or convey any rights or permission to manufacture, use, or sell any patented invention that may relate to them.

This report is the result of contracted fundamental research deemed exempt from public affairs security and policy review in accordance with SAF/AQR memorandum dated 10 Dec 08 and AFRL/CA policy clarification memorandum dated 16 Jan 09. This report is available to the general public, including foreign nationals.

Copies may be obtained from the Defense Technical Information Center (DTIC) (http://www.dtic.mil).

AFRL-RY-WP-TR-2017-0151 HAS BEEN REVIEWED AND IS APPROVED FOR PUBLICATION IN ACCORDANCE WITH ASSIGNED DISTRIBUTION STATEMENT.

AGRESTA.DONALD.L.1207349760
Digitally signed by AGRESTA.DONALD.L.1207349760
DN: c=US, o=U.S. Government, ou=DoD, ou=PKI, ou=USAF, cn=AGRESTA.DONALD.L.1207349760
Date: 2017.09.22 12:23:16 -04'00'

*DONALD L. AGRESTA, Program Manager
Electro-Optic Components Branch
Aerospace Components & Subsystems Division

CASTO.MATTHEW.J.1259265246
Digitally signed by CASTO.MATTHEW.J.1259265246
Date: 2017.10.16 08:13:43 -04'00'

MATTHEW J. CASTO, Chief
Electro-Optic Components Branch
Aerospace Components & Subsystems Division

SATTLER.JAMES.MICHAEL.1236824515
Digitally signed by SATTLER.JAMES.MICHAEL.1236824515
Date: 2017.10.18 16:19:38 -04'00'

JAMES M. SATTLER, Lt Col, USAF
Deputy
Aerospace Components & Subsystems Division
Sensors Directorate

This report is published in the interest of scientific and technical information exchange, and its publication does not constitute the Government's approval or disapproval of its ideas or findings.

*Disseminated copies will show "//Signature//" stamped or typed above the signature.

REPORT DOCUMENTATION PAGE

Form Approved
OMB No. 0704-0188

1. REPORT DATE ***(DD-MM-YY)***
October 2017

2. REPORT TYPE
Final

3. DATES COVERED ***(From - To)***
17 April 2015 – 17 April 2017

4. TITLE AND SUBTITLE
THERMAL AND THERMO-MECHANICAL CHARACTERISTICS OF CRYOGENIC MICROCOOLER FOR OPTIMUM PERFORMANCE AND RELIABILITY

5a. CONTRACT NUMBER
FA8650-15-1-7526

5b. GRANT NUMBER

5c. PROGRAM ELEMENT NUMBER
62716E

6. AUTHOR(S)
Bongtae Han

5d. PROJECT NUMBER
N/A

5e. TASK NUMBER
N/A

5f. WORK UNIT NUMBER
Y18P

7. PERFORMING ORGANIZATION NAME(S) AND ADDRESS(ES)
University of Maryland
Department of Mechanical Engineering
3147 Glenn L. Martin Hall, Building 088
College Park, MD 20742

8. PERFORMING ORGANIZATION REPORT NUMBER

9. SPONSORING/MONITORING AGENCY NAME(S) AND ADDRESS(ES)

Air Force Research Laboratory
Sensors Directorate
Wright-Patterson Air Force Base, OH 45433-7320
Air Force Materiel Command
United States Air Force

Defense Advanced Research Projects Agency
DARPA/MTO
675 North Randolph Street
Arlington, VA 22203

10. SPONSORING/MONITORING AGENCY ACRONYM(S)
AFRL/RYDP

11. SPONSORING/MONITORING AGENCY REPORT NUMBER(S)
AFRL-RY-WP-TR-2017-0151

12. DISTRIBUTION/AVAILABILITY STATEMENT
Approved for public release; distribution is unlimited.

13. SUPPLEMENTARY NOTES
This report is the result of contracted fundamental research deemed exempt from public affairs security and policy review in accordance with SAF/AQR memorandum dated 10 Dec 08 and AFRL/CA policy clarification memorandum dated 16 Jan 09. This material is based on research sponsored by Air Force Research laboratory (AFRL) and the Defense Advanced Research Agency (DARPA) under agreement number FA8650-15-1-7526. The U.S. Government is authorized to reproduce and distribute reprints for Governmental purposes notwithstanding any copyright notation herein. The views and conclusions contained herein are those of the authors and should not be interpreted as necessarily representing the official policies of endorsements, either expressed or implied, of Air Force Research Laboratory (AFRL) and the Defense Advanced Research Agency (DARPA) or the U.S. Government. Report contains color.

14. ABSTRACT
This report details the characterization of cryogenic microcoolers for optimum thermal performance and thermo-mechanical reliability when employed for high power laser diodes (LDs). The goal was achieved by conducting two specific tasks: Development of Cryogenic Microcooler and Apparatus for High-Power LD Bar (Part I) and PoF-based Reliability Assessment of LD/Microcooler Subassembly Subjected to Cryogenic Operating Conditions (Part II). In Part I, an open-loop liquid nitrogen cooler for the cryogenic operation of LD bars was developed and tested. In Part II, the reliability of LD/microcooler subassemblies subjected to cryogenic operating conditions was assessed by proposing a hierarchical physics-of-failure-based reliability assessment model.

15. SUBJECT TERMS
laser diode, cryogenic microcooler, spectral power distribution

16. SECURITY CLASSIFICATION OF:			17. LIMITATION OF ABSTRACT:	18. NUMBER OF PAGES	19a. NAME OF RESPONSIBLE PERSON (Monitor)
a. REPORT	b. ABSTRACT	c. THIS PAGE			Donald Agresta
Unclassified	Unclassified	Unclassified	SAR	98	19b. TELEPHONE NUMBER *(Include Area Code)* N/A

Table of Contents

Section **Page**

Section **Page**

List of Figures

Figure **Page**

Figure **Page**

Figure **Page**

List of Tables

Table **Page**

1. EXECUTIVE SUMMARY

Cryogenic microcoolers was characterized for optimum thermal performance and thermo-mechanical reliability when employed for high power laser diodes (LDs). The goal was achieved by conducting two specific tasks: Development of Cryogenic Microcooler and Apparatus for High-Power LD Bar (Part I) and PoF-based Reliability Assessment of LD/Microcooler Subassembly Subjected to Cryogenic Operating Conditions (Part II).

In Part I, an open-loop liquid nitrogen cooler for the cryogenic operation of LD bars was developed and tested. During design of the cooler, consideration was paid to the needs and conditions under which a field-deployed system would operate. While an open-loop design presented particular challenges for the precise characterization of cooler performance, it dispensed with the bulk, complexity, and power consumption associated with a closed nitrogen refrigeration system. In keeping with this design direction, modifications to the test loop were made to reduce system startup time and prevent ice buildup on the LD emitter surface. These included an aerogel insulation layer and nitrogen shield gas sourced from the LN_2 reservoir, as opposed to isolating the test loop within a high-vacuum chamber. An internally-routed bypass system demonstrated a reduction in the time for cool-down from a room temperature to as little as four minutes, compared to previous hour-long startups. These resulted in compact, coolant-efficient, and responsive system. The results from cryogenic testing of a mounted LD bar showed that the cryogenic cooler and its housing added only 20% additional thermal resistance to that of the commercial block-mounted LD bar. The base of this block mount was brought to -180°C under a dissipated power load of 55 W.

In Part II, the reliability of LD/microcooler subassemblies subjected to cryogenic operating conditions was assessed by proposing a hierarchical PoF-based reliability assessment model. In the model, three aspects of the reliability were considered: optical reliability, LD bar reliability, and thermal reliability. The junction temperature distribution measurement was essential for the model. A hybrid experimental/numerical method was proposed and implemented to predict the junction temperature distribution of a high power LD bar first. Then, a novel method was developed to predict the spectral power distributions (SPDs) of individual emitters by deconvoluting the SPD of an LD array. This method was utilized to predict the SPD change caused by the die attach crack of the LD bar. Thermal and mechanical models were subsequently developed to predict thermo-mechanical stresses of the subassembly and thus to be able to predict the potential failure locations and the crack propagation within the die attach during test conditions. Finally, the effect of die attach crack on the SPD change was calculated for the physics-of-failure (PoF)-based reliability assessment.

2. PART I: DEVELOPMENT OF CRYOGENIC MICROCOOLER AND APPARATUS FOR HIGH-POWER LD BAR

Detailed heat transfer data for two-phase nitrogen flow in complex structures (e.g. microfluidic coolers) is underrepresented in literature. With little prior work on which to model the cryogenic cooler, considerable attention was paid to predicting cooler performance, choosing a candidate design, and characterizing the fabricated cooler prior to integrating the LD bar for final testing. This chapter summarizes those efforts, and concludes by detailing the results of cryogenic operation of the LD bar.

2.1 Development of Cryogenic Microcooler

2.1.1 Prediction of Pin-Fin Thermo-fluid Characteristics

The use of microcoolers, relying on evaporation and two-phase flow through arrays of micro pin fins, is not yet established in the electronic cooling community and little research has been done to quantify and correlate the heat transfer rates and pressure drops for such configurations. The available correlations include no LN_2 data, and – like many other two-phase flow correlations – rarely provide better than an accuracy of +/- 30%. Nonetheless, these correlations can still identify general thermofluid trends for two-phase flow. Among these, the pin- fin correlation derived by Peles & Krishnamurthy [1] has been extensively evaluated by other investigators and found to provide the most consistent results. Accordingly, the purpose of this preliminary study is to observe general parametric trends for two-phase flow through micro pin- fin structures with LN_2 using the correlation originally derived by Peles & Krishnamurthy [1] and modified by Reeser et al. [2] and subsequently tuning the correlation to the data sets obtained in the current experimental effort. Of specific interest, during both validation and actual Laser Diode bar testing, are the effects of parameters such as flow quality, heat flux, mass flux, pin-fin geometry, and flow regime on the thermal performance (heat transfer coefficient) of the final micro pin-fin cooler design. The Reeser et al. [2] correlation was, thus, used to gather some insight on these parametric effects and to guide the initial design of the micro pin fin cooler.

The Reeser et al. [2] correlation is given in full detail:

$$h_{tp} = \zeta(\phi^2)^{0.2475} h_{sp}$$

where,

$$h_{sp} = \frac{Nu \cdot k_f}{d_{fin}}$$

$$Nu = C_{Nu}\left(\frac{S_L}{D_f}\right)^{0.2}\left(\frac{S_T}{D_f}\right)^{0.2}\left(\frac{h_f}{D_f}\right)^{0.25}\left(1+\frac{dh}{D_f}\right)^{0.4}\mathrm{Re}^{0.6}\,\mathrm{Pr}^{0.36}\left(\frac{\mathrm{Pr}}{\mathrm{Pr}_w}\right)^{0.25}$$

$$(\phi)^2 = 1 + \frac{0.24}{X_{vv}} + \frac{1}{X_{vv}^2}$$

$$X_{vv} = \left[\frac{(\Delta P_f/\Delta Z)_f}{(\Delta P_f/\Delta Z)_v}\right]^{1/2} \quad (\Delta P_f)_f = \frac{fN(G(1-x))^2}{2\rho_f} \quad (\Delta P_f)_v = \frac{fN(Gx)^2}{2\rho_v}$$

$$\zeta = C_1 e^{C_2 x_e} + C_3 x_e^3 + \left(\frac{C_4}{G+C_5}\right)^{1/2}$$

$D_f = d_{fin}$ = hydraulic diameter of single pin
S_L = streamwise pin pitch
S_T = traverse pin pitch
N = total number of pins
h_f = height of pin
dh = gap above pin (0 for this study)
Re = Reynolds number
Pr = Prandtl number
Pr_w = Prandtl number for wall temperature
f = friction factor
k_f = thermal conductivity of fluid
X_{vv} = Martinelli parameter
x = flow quality
x_e = flow quality at exit
G = mass flux
ρ_f = density of liquid
ρ_v = density of vapor
h_{sp} = single-phase heat transfer coefficient
h_{tp} = two-phase heat transfer coefficient
C_{Nu}, C_1, C_2, C_3, C_4, C_5 = empirical constants

As shown, the correlation takes into account the pin-fin geometry, fluid & thermal properties, mass flow rate, and flow quality. The range of conditions tested was based on the parametric space in which the correlation was derived. The baseline conditions are always plotted in black and are as follows:

- LN_2
- T_{sat} = 80K
- 800 kg/m^2-s mass flux
- 12 x 12 mm^2 pin-fin channel
- Inline configuration of pins
- 150 µm wide pins
- 300 µm pitch
- 300 µm height
- ~275% Area Enhancement

2.1.1.1 Mass Flux

The effect of mass flux on the heat transfer coefficient vs. flow quality profile is demonstrated in Figure 1 for the baseline conditions. Note that the base heat transfer coefficient takes into account the surface area enhancement from the pin-fin structure. As shown, the correlation predicts a “softened” M-shape profile and a rapid deterioration in the heat transfer coefficient (caused by dryout) after a flow quality of roughly 65%. The second peak in the profile occurs at flow qualities between 30 to 50%, shifting to higher qualities with decreasing mass flux. This trend is attributed to the higher velocities at higher mass fluxes, which trigger an earlier breakdown (dryout) in the evaporating liquid film. Overall, increasing the mass flux enhances the heat transfer coefficient at lower qualities and decreases the heat transfer coefficient at higher qualities, with a transition quality that decreases with increasing mass flux.

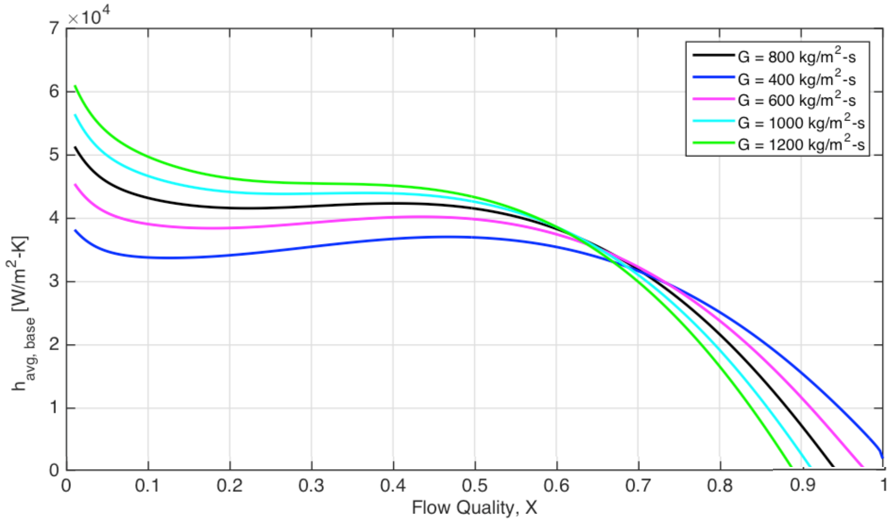

Figure 1: Influence of Mass Flux on the Base Heat Transfer Coefficient vs. Flow Quality Profile

LN_2, T_{sat} = 80K, 12 x 12 mm^2 channel, inline configuration, 150 µm wide pins, 300 µm pitch, and 300 µm height.

2.1.1.2 Pin-Fin Height

The effect of pin-fin height on the base heat transfer coefficient vs. flow quality profile is displayed in Figure 2 for the baseline mass flux of 800 kg/m^2-s. As shown, the heat transfer coefficient increases across the entire flow quality range with increasing pin-fin height. The local fin wall heat transfer coefficient does diminish with increasing pin-fin height but is offset by the enhancement in surface area due to the taller fins, resulting in an overall steady increase in the base heat transfer coefficient with fin height. According to the correlation, it is clearly advantageous to increase the pin-fin height above the 300 µm baseline, thus enhancing the heat transfer coefficient while reducing the pressure drop as a result of the increased hydraulic diameter.

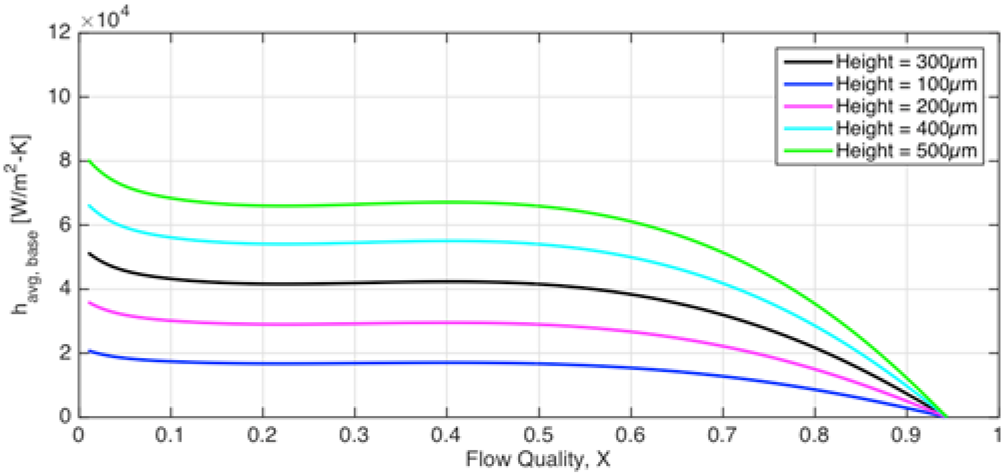

Figure 2: Influence of Pin Fin Height on the Base Heat Transfer Coefficient vs. Flow Quality Profile for a Mass Flux of 800 kg/m^2-s and Pin Height of 100, 200, 300, 400, and 500 µm

LN_2, T_{sat} = 80K, 12 x 12 mm^2 channel, inline configuration, 150 µm wide pins, and 300 µm pitch.

2.1.1.3 Streamwise & Traverse Pin-Fin Pitch

The effect of streamwise and traverse pin-fin pitch on the base heat transfer coefficient vs. flow quality profile is demonstrated in Figure 3 and Figure 4 for the baseline mass flux of 800 kg/m^2-s and pin-fin width of 150 µm. As shown, the heat transfer coefficient increases across the entire flow quality range with decreasing pin-fin pitch. Reducing the pin-fin pitch increases the wetted surface area (for a given channel footprint) and thins the liquid film on the fins thus enhancing the base heat transfer coefficient. Additionally, the influence of streamwise and traverse pin-fin pitch on the heat transfer coefficient is identical (i.e., Figure 4 and 5 are identical).

Accordingly, it is thermally advantageous to reduce the pin-fin pitch, but thermal gains will come at a cost of a larger pressure drop across the array.

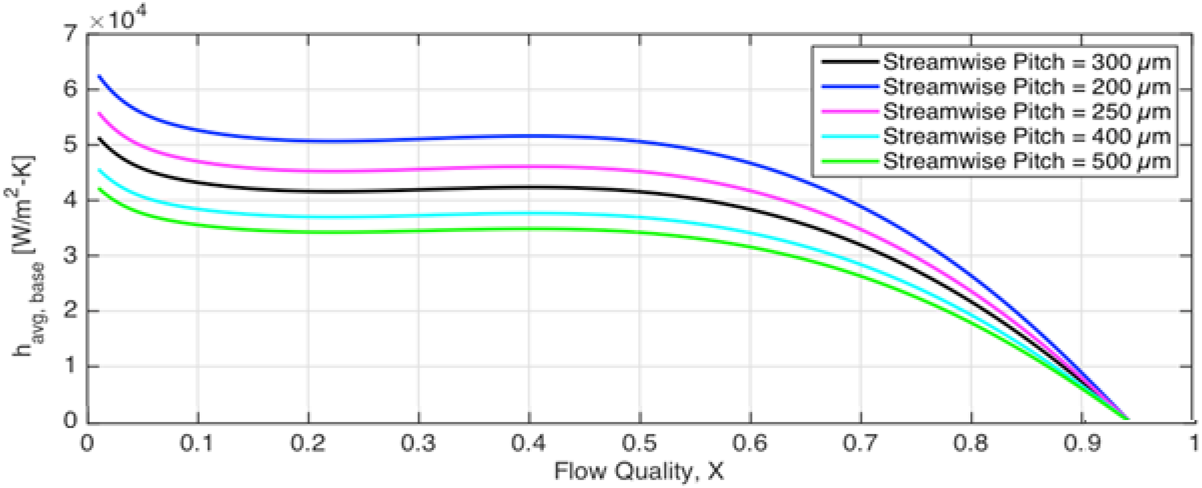

Figure 3: Influence of Streamwise Pin Fin Pitch on the Base Heat Transfer Coefficient vs. Flow Quality Profile for a Mass Flux of 800 kg/m^2-s

LN_2, T_{sat} = 80K, 12 x 12 mm^2 channel, inline configuration, 150 µm wide pins, and 300 µm height.

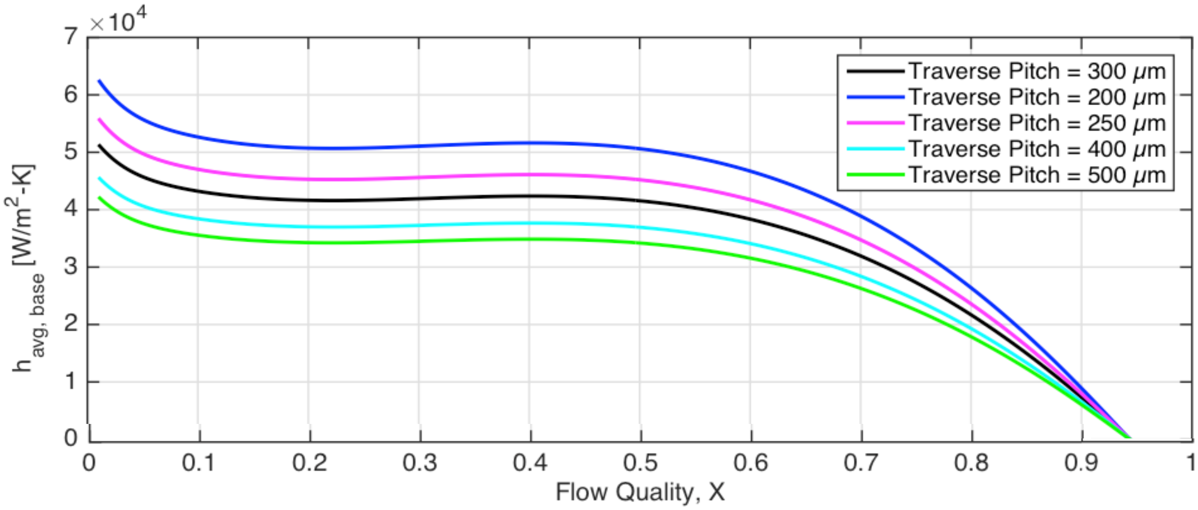

Figure 4: Influence of Traverse Pin Fin Pitch on the Base Heat Transfer Coefficient vs. Flow Quality Profile for a Mass Flux of 800 kg/m^2-s

LN_2, T_{sat} = 80K, 12 x 12 mm^2 channel, inline configuration, 150 µm wide pins, and 300 µm height.

2.1.1.4 Variable Pin-Fin Width with Constant Gap

The effect of pin-fin width – for a constant gap of 150 µm between adjacent pin-fins – on the base heat transfer coefficient vs. flow quality profile is demonstrated in Figure 5 for the baseline mass flux of 800 kg/m^2-s and pin-fin height of 300 µm. As shown, reducing the pin-fin width significantly increases the heat transfer coefficient across the entire flow quality range, reflecting – in part – the increase in wetted surface area in the fin array and – in part – the thinner film thickness. However, as the “minimum” thickness of the pin-fins is limited by machining constraints, (especially for high aspect ratio pins), the baseline pin width of 150 μm was chosen for the final design.

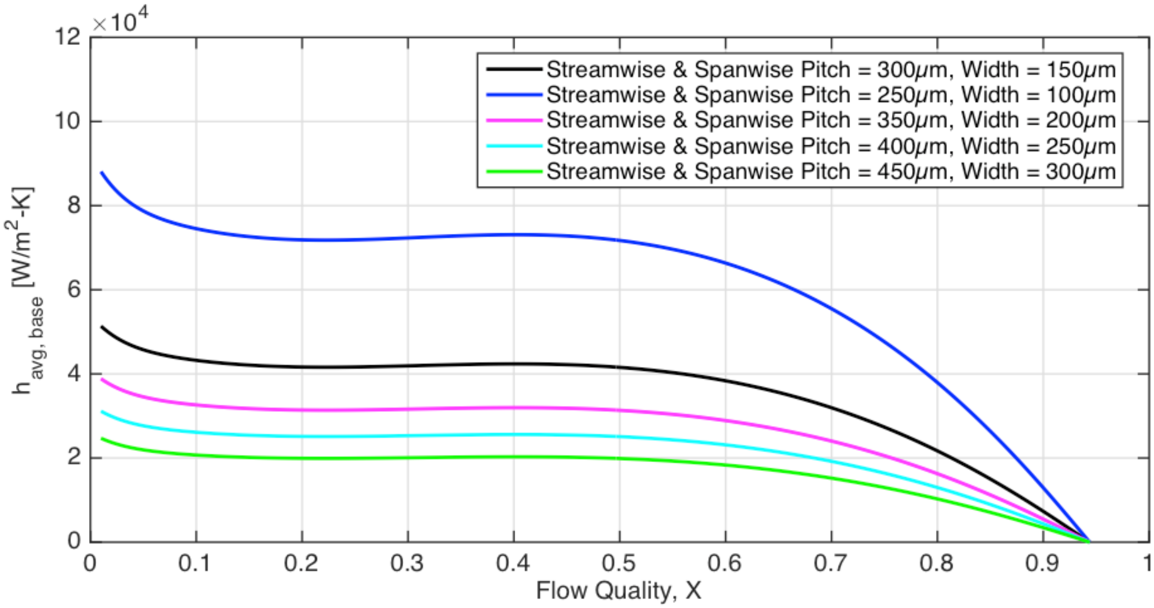

Figure 5: Influence of Pin-Fin Width on the Base Heat Transfer Coefficient vs. Flow Quality Profile for a Mass Flux of 800 kg/m^2-s and Constant Gap of 150 μm between Adjacent Pins

LN_2, T_{sat} = 80K, 12 x 12 mm^2 channel, inline configuration, and 300 μm pin-fin height.

2.1.2 Summary of Preliminary Correlation Study

According to the results obtained by exercising the Reeser et al [2] correlation across the parametric space of interest in this study, it is thermally advantageous to increase the mass flux (for low- to mid-range qualities) and pin-fin height, and decrease streamwise/transverse pin-fin pitch, and pin-fin width. These are the main trends observed from this parametric study. However, the correlation derived by Peles & Krishnamurthy [1] was developed using relatively long pin-fin arrays, while – in the present application – the pin-fin array is significantly shorter. Limited chip- scale microgap data [3-4] suggests that there are significant differences in the thermofluid behavior of short and long microchannels. It is, consequently, important to obtain relevant experimental data for such short, pin fin channels before finalizing the design of the LN_2 microcooler. In the next section, data from such an experiment using a fluid similar to LN_2 (3M FC-72) are compared to the predictions from the correlation.

2.1.3 Experimental Short-Array Micro Pin-Fin Data

In the previous section, a two-phase micro pin-fin correlation derived by Reeser et al. [1, 2] was used to parametrically analyze the thermal performance of a LN_2 pin-fin channel for various mass fluxes, flow qualities, and pin-fin geometries. According to the correlation, it is thermally advantageous to increase the mass flux, pin-fin height, decrease streamwise and transverse pin-fin pitch, and pin-fin width. However, the correlation derived by Reeser et al. was developed using relatively long pin-fin arrays. To further increase confidence in the selected cooler design parameters, the correlation predictions were benchmarked against a short-array pin-fin experimental study using 3M FC-72 as the working fluid.

An overview of the pin-fin channel and test section used in the benchmarking study is shown in Figure 6 and Figure 7, respectively. The pin-fins are machined out of the copper pedestal shown in Figure 6, which is inserted into the test section shown in Figure 7. The pin-fins are positioned in an inline configuration, are 150 µm wide, have a pin-to-pin pitch of 300 µm, and are either 100 µm or 500 µm tall. The entire pin-fin array is 12 mm x 12 mm in size, amounting to a total of 1600 pin-fins. Heat is applied to the bottom of the pin-fins with a ceramic resistive heater and temperature is measured using five embedded thermocouples, positioned along the centerline of the pin-fin channel and 1 mm below the surface. The pin-fin channel is inserted into a PEEK test section, which channels fluid to and from the pin-fins. The upper surface of the pin-fins is confined with a sapphire window, which is used for top-down photographic and mid-wave infrared visualization.

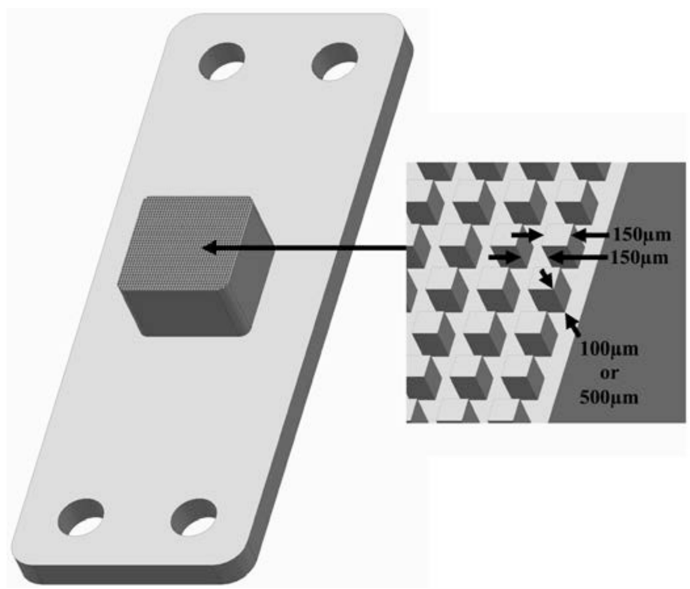

Figure 6: Copper Micro Pin-Fin Channel

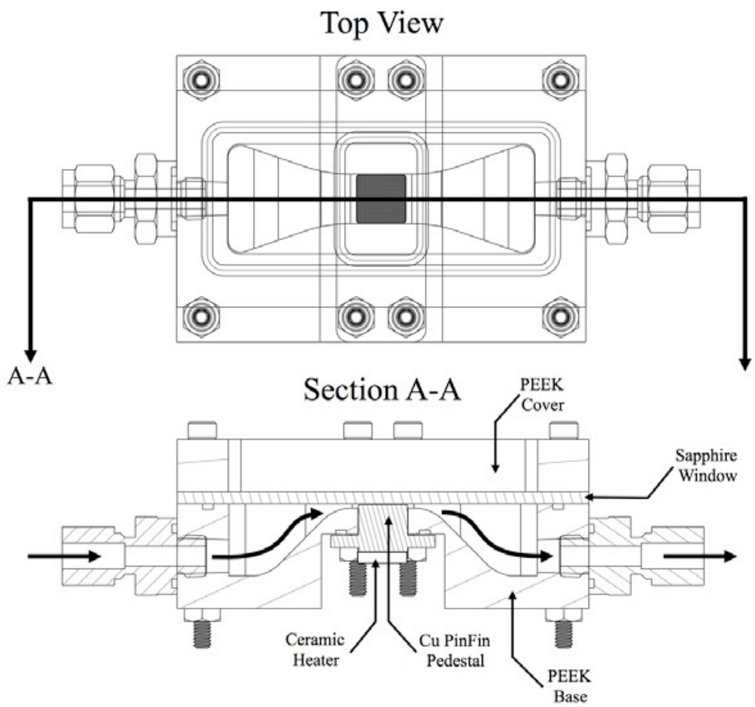

Figure 7: Micro Pin-Fin Test Section

The experimentally measured base average heat transfer coefficient and pressure drop vs. flow quality profiles are shown in Figure 8 and Figure 9, respectively, for both the 100 µm and 500 µm tall pin-fin channels. Data for the 100 µm tall pin-fin channel is presented at three different liquid flow rates: 0.5, 0.75, and 1.0 mL/s and data for the 500 µm tall pin-fin channel is presented for one flow rate: 1.0 mL/s. The base surface area enhancement is 1.67x and 4.33x for the 100 µm and 500 µm tall pin-fin channels, respectively. The predicted base heat transfer coefficient, using the correlation derived by Reeser et al. [1, 2], is plotted as a dotted line. As shown, the heat transfer coefficient and pressure drop steadily rises, on average, with increasing flow quality, heat flux, and flow rate. The 100 µm and 500 µm tall pin-fin channels reach a maximum heat transfer coefficient of 55,000 and 43,000 W/m^2-K at a flow quality of 99 and 94%, respectively, for a flow rate of 1.0 mL/s. On average, the base heat transfer coefficient for the 100 µm and 500 µm tall pin-fin channels is similar for the 1.0 mL/s flow rate but the pressure drop is significantly lower for the taller pin-fins because of the substantial increase in cross-sectional area in the flow direction. The surface heat transfer coefficient for the taller pin-fins is less (attributed to the decrease in flow velocity) and these base heat transfer coefficient results imply that the increase in surface area counteracts the decrease in the surface heat transfer coefficient for the taller pin-fins. However, the substantial decrease in the pressure drop is especially important for applications where pumping power must be minimized. Overall, these preliminary results indicate that taller pin-fins are ideal for low pumping power applications; however, more data needs to be gathered before drawing any definite conclusions.

As shown in Figure 8, while the experimental heat transfer coefficient results are generally in the range of the correlation-derived predictions, the average percent error, at greater than 110%, is unacceptably high. The correlation under predicts the heat transfer coefficient for most cases and especially at higher flow qualities. Also, the trends contradict one another; the correlation predicts a heat transfer coefficient that falls, on average, with increasing flow quality, whereas the experimental results demonstrate a heat transfer coefficient that steadily increases with flow quality. Accordingly, some additional care – beyond the application of the Reeser et al correlation – must be taken in designing the LD micro pin-fin cooler to reflect these experimental trends.

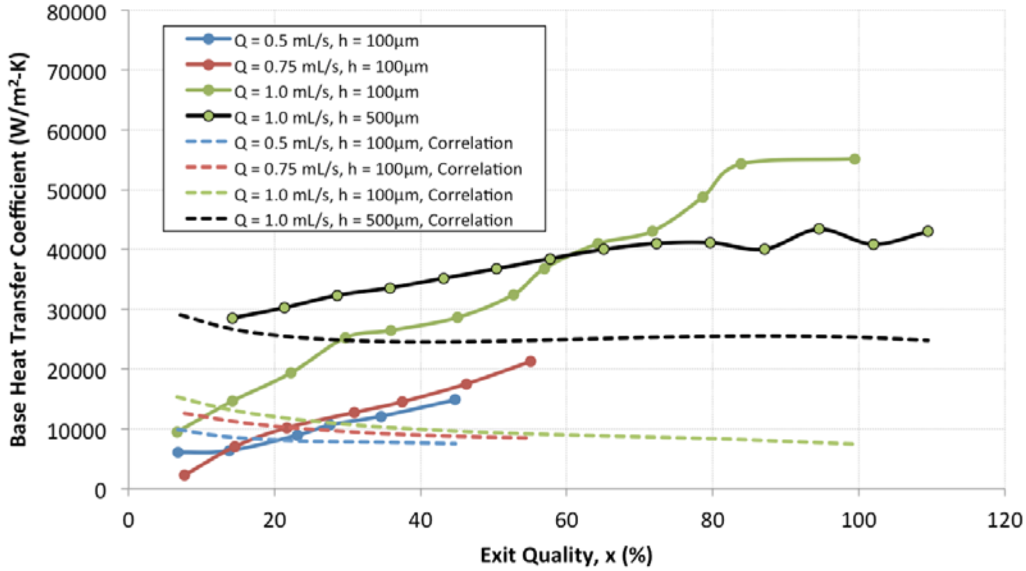

Figure 8: Base Heat Transfer Coefficient vs. Exit Quality for Two-Phase Micro Pin-Fin Channel

FC-72, 0.5 to 1.0 mL/s, 12 mm x 12 mm channel, inline pin-fin configuration, pin-fins are 150 µm wide, either 100 µm or 500 µm tall, and have a pitch of 300 µm. Dotted line data is predicted heat transfer coefficient using pin-fin correlation from [2].

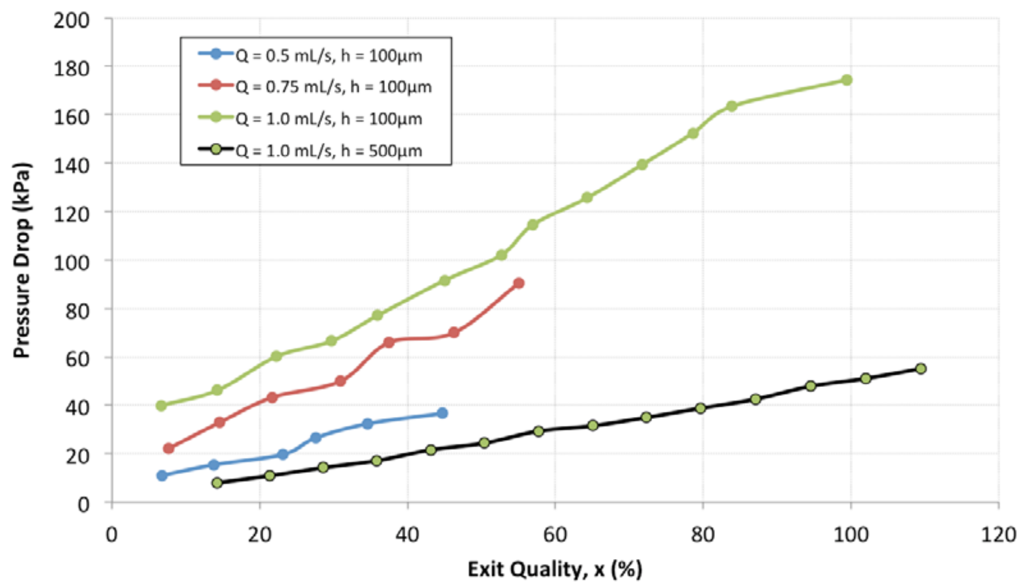

Figure 9: Pressure Drop vs. Exit Quality for Two-Phase Micro Pin-Fin Channel

FC-72, 0.5 to 1.0 mL/s, 12 mm x 12 mm channel, inline pin-fin configuration, pin-fins are 150µm wide, either 100µm or 500µm tall, and have a pitch of 300µm.

2.2 Apparatus of Cryogenic Microcoolers for High-Power LD Bar

2.2.1 Final Design of Micro-Pin Fin Manifold

Armed with the insights obtained from the correlation study and FC-72 micro-pin fin benchmarking experiment, a final liquid nitrogen cooler design was produced. A cross-sectional and exploded view of the final design iteration is shown in Figure 10 and 11, respectively. The cooler consists of three copper parts: an upper insert, a lower insert, and a central manifold. The micro pin-fins are milled out of the upper insert and positioned under the LD bar or test heater. The design parameters of the pin-fin array itself are identical to the baseline of the correlation study: 150 µm wide, 300 µm tall pins at a pitch (streamwise and transverse) of 300 µm. However, the footprint of the array has been reduced to 10 mm x 10 mm. This both better matches the LD bar emitter width as well as the footprint of the ceramic heater used for cooler characterization.

The central piece serves as a plenum/manifold, channeling LN_2 to and from the micro pin-fin array. Finally, the lower insert seals off the lower plenum machined in the underside of the central manifold. As shown in the exploded view, the three sections of the cooler are bolted together and contact surfaces are sealed using a flexible cryogenic sealant.

For the initial evaluation of the thermal performance, a resistive heater is placed directly above the pin-fins in order to simulate the waste heat of an LD bar. The modular design of the cooler facilitates a simple exchange of different pin-fin designs for future studies. Following the evaluation of the cooler thermal performance, the LD bar is then bolted to the non-wetted side of the upper insert, using a thermal interface material (TIM) between the cooler and LD bar (as diagrammed in Figure 4).

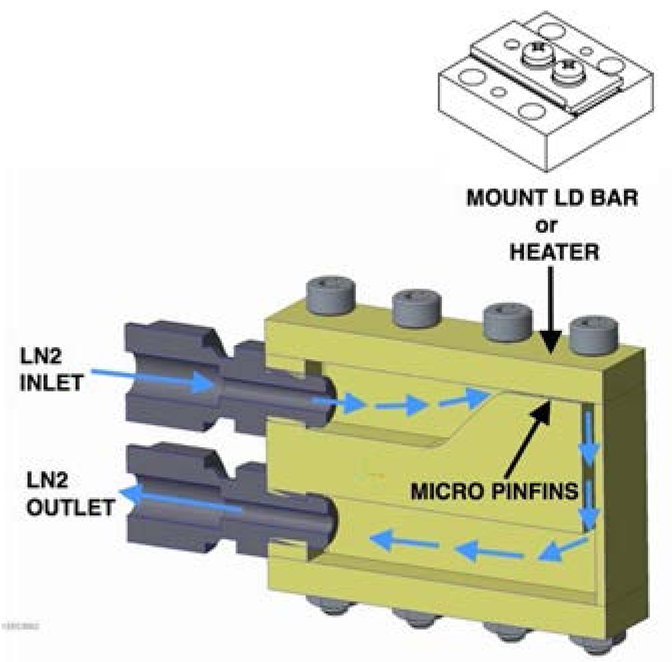

Figure 10: Cross-Sectional View of Cryogenic Micro Pin-Fin Cooler

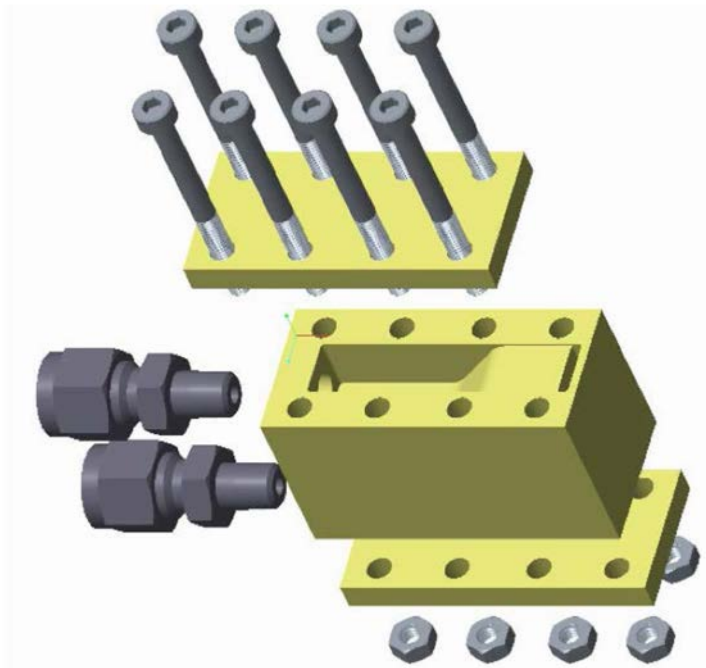

Figure 11: Exploded View of Cryogenic Micro Pin-Fin Cooler

2.2.2 Design and Final Assembly of LN_2 Flow Loop Apparatus

The cryogenic flow loop apparatus is critical in both regulating the supply of liquid nitrogen to the pin-fin array and in collecting experimental data during both the test heater reference experiments and the powered LD bar tests. While the flow loop underwent several iterations during the project, the basic open-loop design philosophy remained constant.

Shown in Figure 12 – along with a schematic in Figure 13 – is the underlying flow loop before installation of the cooler manifold and cryogel insulation. LN_2 is stored and supplied via a pressurized tank, where the tank's integrated pressure regulator is used to regulate the flow of LN_2 through the flow loop and cooler. The LN_2 flows from the tank into a four-way junction, where the temperature (T_{INLET}) and pressure (P_{INLET}) are measured with an Omega E-Type thermocouple and cryogenic pressure transducer, respectively. The LN_2 then proceeds to flow into the LD cooler (not pictured, installed at the blue end-caps visible in Figure 12), where the flow absorbs heat from the LD bar and phase changes from liquid to vapor. The two-phase mixture then exits the LD cooler and flows through another four-way junction, where the temperature (T_{OUTLET}) and pressure (P_{OUTLET}) are measured again. The pressure and temperature sensors monitor the saturation temperature, bulk fluid temperature, and pressure drop across the LD two-phase cooler.

After exiting the four-way junction, the two-phase flow of LN_2 then proceeds through a liquid-to-liquid heat exchanger. The purpose of the heat exchanger is to completely evaporate all of the excess LN_2 and heat the nitrogen gas to roughly room temperature, so that the mass flow rate can be measured with the nitrogen gas mass flow meter. The LN_2 is heated with the heat exchanger using a constant temperature water loop maintained at 25°C. The temperature of the nitrogen gas is measured after the heat exchanger with an Omega E-Type thermocouple to ensure complete evaporation and heating of the LN_2 to standard atmospheric conditions.

All of the Swagelok compression fittings and tubing are made of 316SS and the apparatus is insulated using Cryogel Z insulation. Data is measured and logged in LabVIEW using a National Instruments NI 9214 (thermocouple) and NI 9205 (voltage) cDAQ module.

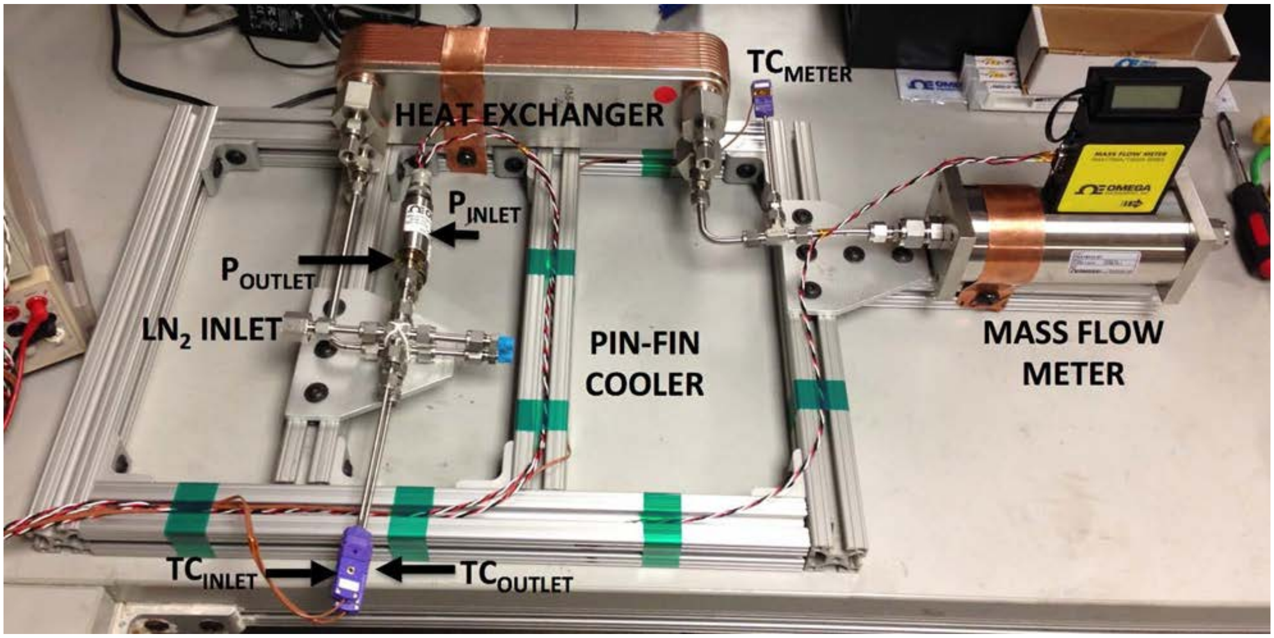

Figure 12: Assembled LN_2 Flow Loop Apparatus

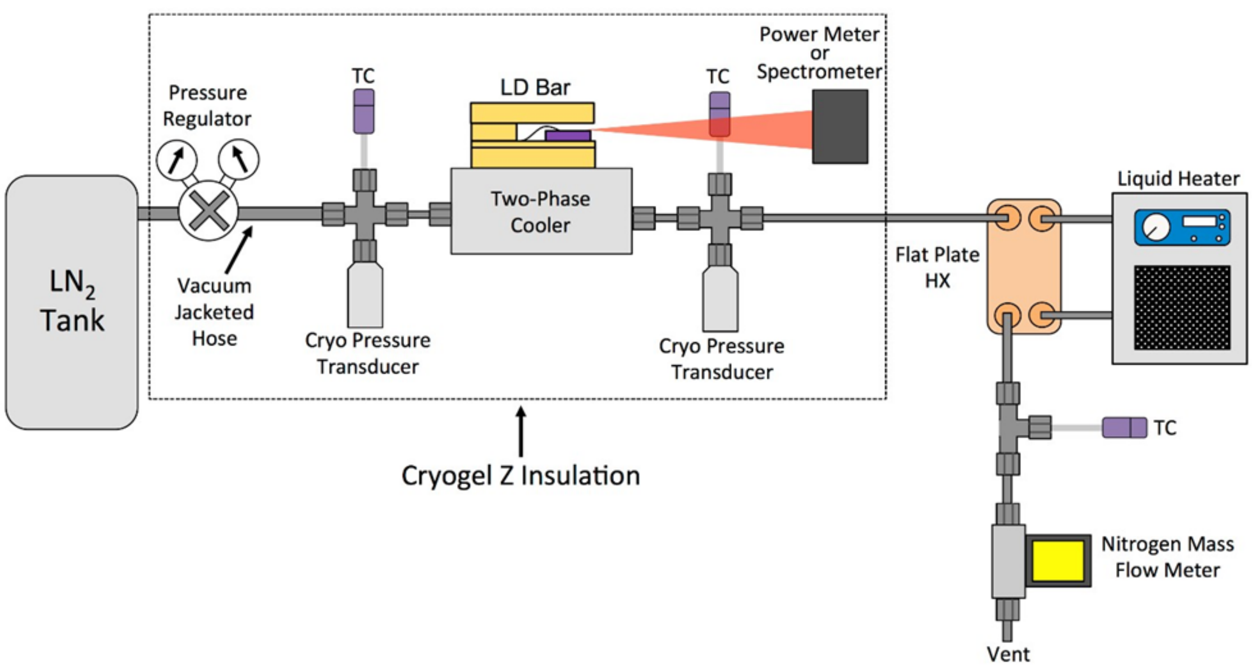

Figure 13: Schematic of LN_2 Flow Loop Apparatus

2.2.3 LN_2 Flow Loop Apparatus Heat Leakage – Cryogel Z Insulation

Because the saturation temperature of liquid nitrogen is so much lower than room temperature (-196˚C at 1 bar), heat leakage from the surrounding ambient into the LN_2 apparatus must be minimized. Minimizing the heat leakage will, in turn, reduce the flow quality at the inlet by preventing premature (parasitic) phase change, maximizing the amount of latent heat available for the LD micro pin-fin cooler. While frequently a sealed chamber under high vacuum can be used to thermally insulate a cryogenic apparatus, this approach is very expensive and complex. A more direct approach is to use insulation designed for cryogenic applications, such as Cryogel Z (made by Aspen Aerogels). A plot of thermal conductivity versus temperature for Cryogel Z insulation is shown below in Figure 14, where it can be observed that the thermal conductivity falls with decreasing temperature and has a temperature-averaged value of about 0.015 W/m-K, approximately half the value of dry air. The claimed thermal conductivity value was also experimentally confirmed for an average insulation temperature of 35 and 45˚C. The experimentally determined thermal conductivity was only slightly lower than the thermal conductivity claimed in the datasheet and within the limits of experimental error.

The amount of heat leakage for the LN_2 flow loop was approximated for the first portion of the flow loop, consisting of all the components leading up to the LD cooler inlet and the LD bar/cooler itself. For the heat leakage approximation, it's assumed that the inner wall temperature (e.g., wall temperature of stainless steel plumbing and fittings) is -196˚C, ambient temperature is 25˚C, and the dominate mode of heat transfer is natural convection. A 1-D heat transfer analysis was then performed using the known geometry of the plumbing, fittings, and fixtures. The results from the heat leakage approximation are shown in Figure 15 with a plot of cooler inlet quality, X, versus flow rate of LN_2. As shown, without insulation the inlet quality is very high at lower flow rates (e.g., 45% at a flow rate of 1 mL/s), indicating that the heat leakage is significant and thus reducing the amount of latent heat available for the LD cooler. Conversely, the cooler inlet quality is significantly reduced with just 5 mm of Aerogel/Cryogel Z insulation and further reduced with 10 mm of insulation. With 10 mm of Cryogel Z insulation, the cooler inlet quality is estimated at 8% for a flow rate of 1 mL/s – an acceptable coolant expenditure given the remaining latent heat available in the remaining liquid delivered to the pin-fin array.

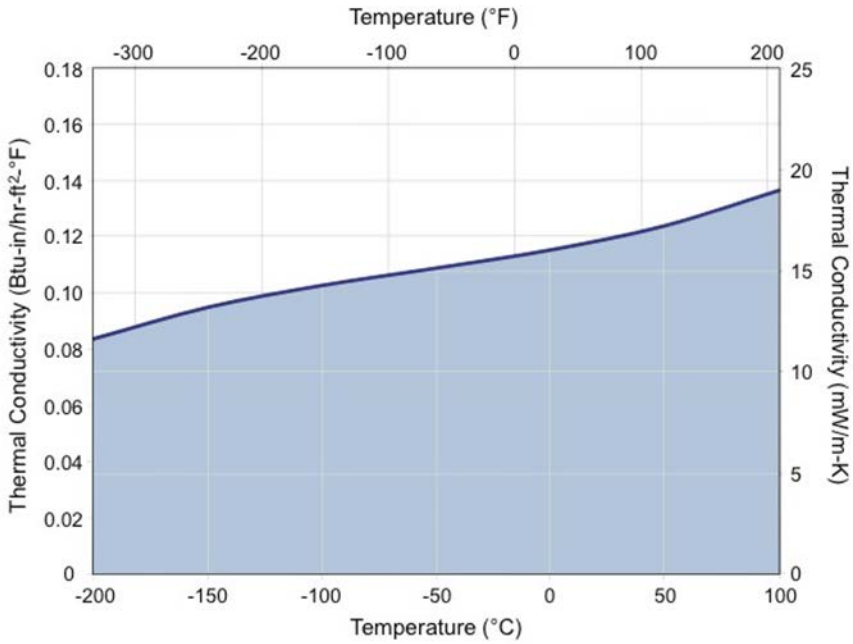

Figure 14: Thermal Conductivity vs. Temperature for Cryogel Z Insulation
Source: Aspen Aerogels datasheet.

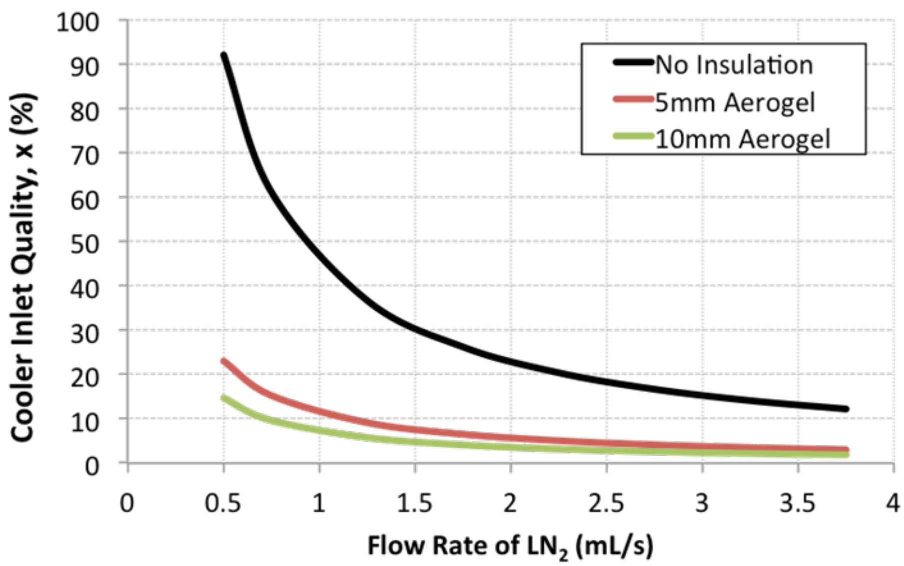

Figure 15: LD Cooler Inlet Quality versus Flow Rate from Heat Leakage Approximation for LN_2 Flow Loop Apparatus

2.2.4 Preliminary Testing of LN_2 Flow Loop Apparatus

Following the assembly of the LN_2 flow loop, a cursory two-phase cooling test was performed. In order to quickly evaluate the functionality of the flow loop and to assess whether the loop is performing as designed, a Lytron off-the-shelf aluminum cold plate was attached to the LN_2 flow loop in place of the pin-fin cooler. A 10 mm x 10 mm ceramic resistive heater and E-type thermocouple was attached to the cold plate in order to evaluate the two-phase thermal performance of the cold plate configuration with LN_2, as shown in Figure 16.

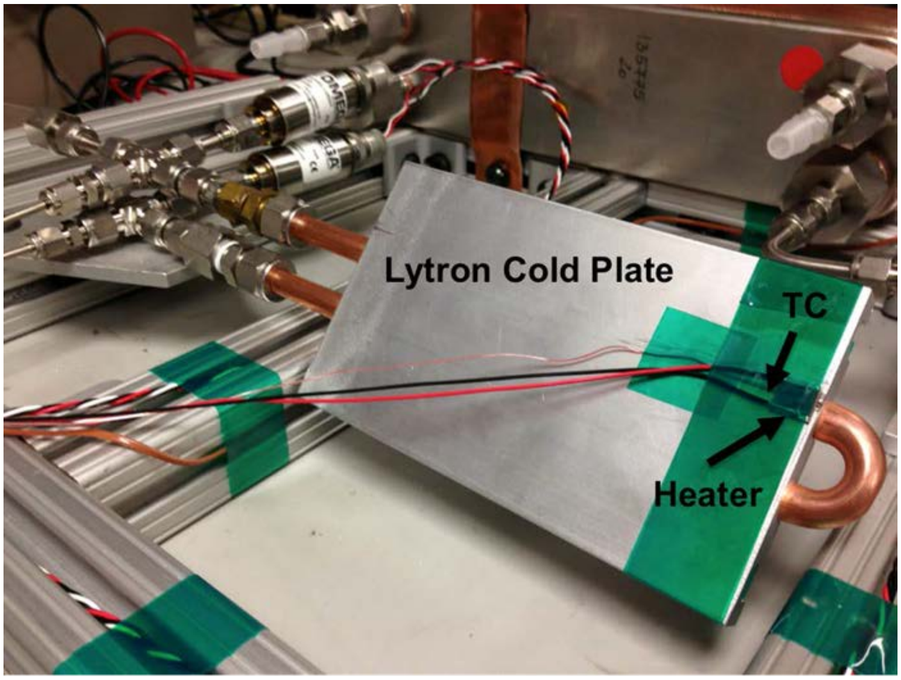

Figure 16: Lytron Cold Plate Setup used to Test LN_2 Flow Loop Apparatus

The initial testing of the flow loop was satisfactory in that it didn't reveal significant problems with the functionality of the flow loop. The LN_2 tank provided a very constant source of pressure and flow – with very little fluctuations. The tank's valve allowed precise control over the flow rate. Moreover, the pressure transducers, thermocouples, and mass flow meter performed as expected and the water-nitrogen heat exchanger effectively evaporated and superheated any remaining LN_2 to room temperature.

A plot of the heat transfer coefficient (HTC) versus calculated change in flow quality (outlet quality – inlet quality) for the Lytron cold plate with LN_2 is shown in Figure 17. This HTC is calculated using the temperature rise of the plate-heater interface with respect to the inlet fluid saturation temperature, with the footprint of the ceramic heater used as the normalization area. No insulation was used for this initial test so the inlet quality is not zero (or near zero), hence the x- axis is given as a change in flow quality and not an absolute value. The heat transfer coefficient profile shown in Figure 17 is for a flow rate of 3.0 mL/s (2.42 g/s) of LN_2, an inlet saturation temperature of -184˚C (slightly above atmospheric pressure), pressure drop from 8.5 to 14.9 kPa, and heat flux of 50 to 150 W/cm^2. As shown, the HTC rises with increasing flow quality and heat flux up to a change in flow quality of around 10%, where it peaks at a value of 15,000 W/m2-K. The heat transfer coefficient then quickly falls off for changes in flow quality above 10%, reaching a minimum of 6500 W/m^2-K at a change of flow quality of 14.2%. This rapid drop in the heat transfer coefficient is likely caused by dryout of the heated surface. Nonetheless, the profile obtained is similar in shape and magnitude to the thermal data previously published by Qi et al. [3] for flow boiling of LN_2 in mini tubes.

This same basic procedure is used in future tests to evaluate the thermal performance of the micro pin-fin cooler.

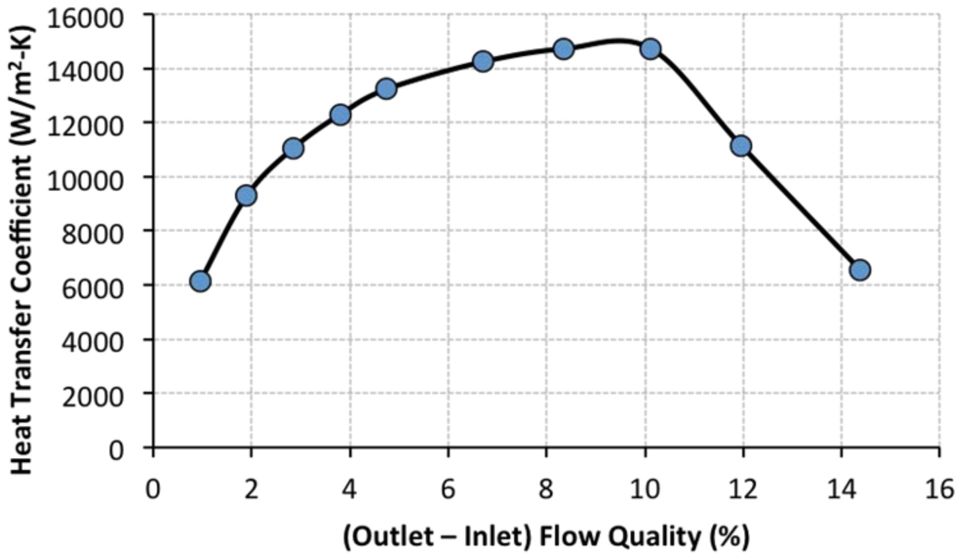

Figure 17: Heat Transfer Coefficient versus Change in Flow Quality (outlet – inlet) for Lytron Cold Plate with LN_2

$Q = 3.0$ mL/s, $G = 110$ kg/m^2-s, $q'' = 50$–150 W/cm^2, $T_{sat,avg} = -184$˚C, $\Delta P = 8.5$-14.9 kPa, and $D = 8$mm (copper tube with U-bend).

2.2.5 Installation and Initial Testing of LN_2 Pin-Fin Cooler

Following the assembly of the flow loop and preliminary cold plate testing, the micro pin- fin cooler was installed and the flow loop insulated. The installed cooler is shown in Figure 18 occupying the location of the prior Lytron cold plate. As with the cold plate, a 10 mm x 10 mm ceramic resistive heater is attached to evaluate the two-phase thermal performance of the pin-fin cooler. Three thermocouple holes provide temperature readings at the inlet, midpoint, and outlet of the pin-fin array, and are used in conjunction with dissipated power of the heater to determine the pin-fin cooler's performance.

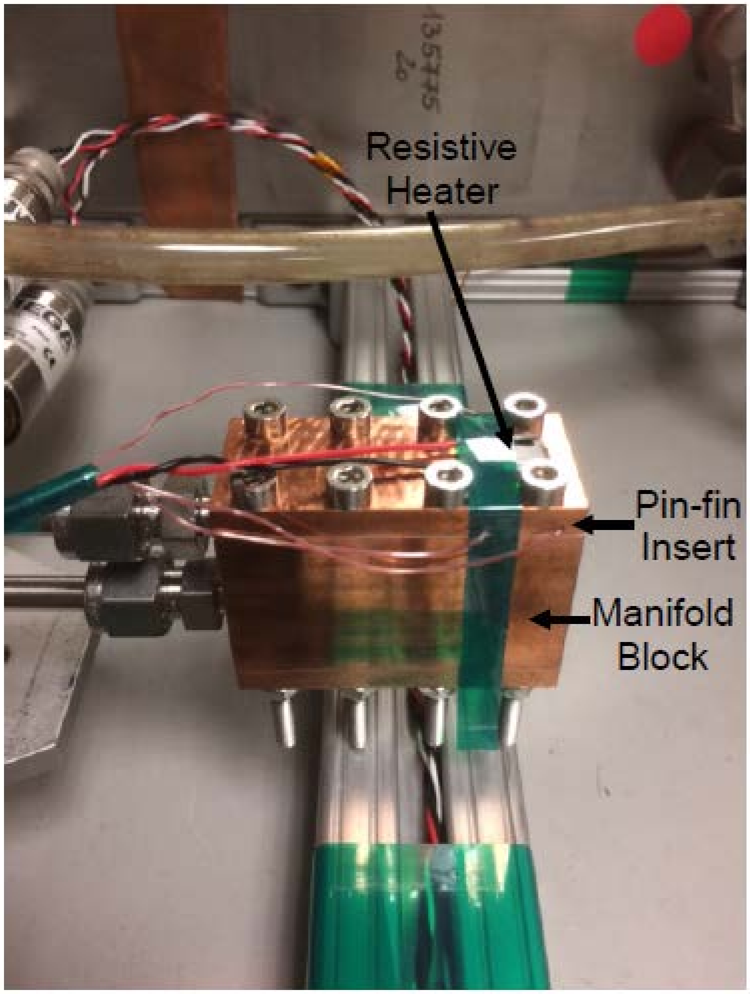

Figure 18: Assembled LN_2 Pin-Fin Cooler

For the two-phase flow process, in the absence of an ability to empirically determine the input or output flow quality, the change in quality across the microcooler is the only determinable quality parameter. As discussed, in order to provide flow to the pin-fin cooler with near-zero inlet quality, aerogel insulation was installed on the flow loop and manifold. The installed cooler insulation is shown in Figure 19. Further aerogel insulation (not shown in Figure 2) was added to the cryogenic hose supplying LN_2 from the tank.

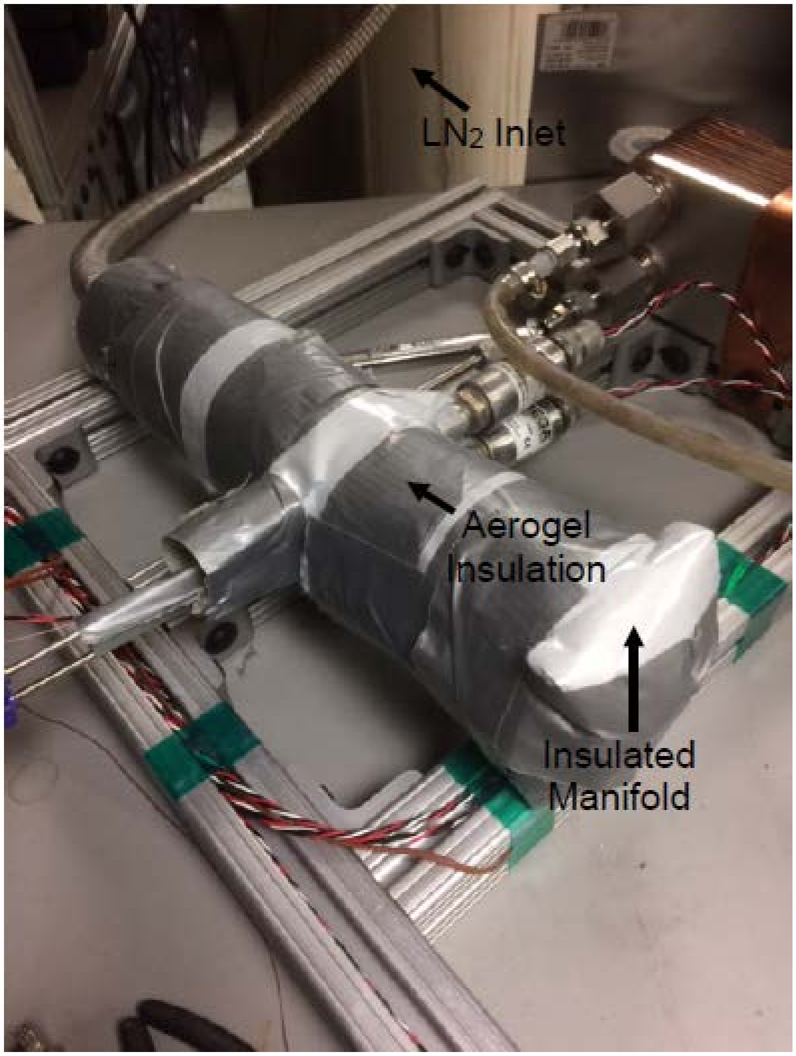

Figure 19: Flow Loop and Manifold Aerogel Insulation

2.2.6 Design and Purpose of Bypass/Blowdown System

A final flow loop modification was made to address the difficulty of bringing the liquid vaporization front into and past the pin-fin array with the available 22 psig (237 kPa abs) delivered by the nitrogen tank. Because the system startup from room temperature involves single-phase gas flow, the pressure drop required for a given startup mass flow through the array are much higher than if the nitrogen flow was in liquid or two-phase conditions. This is in contrast to typical two-phase applications where the saturation temperature is above room temperature, where startup begins with zero-quality liquid and transitions to two-phase after the thermal load to the cooler is applied. Without a way to bypass this gas flow restriction, the initial cool-down of the pin-fin cooler and manifold occurs on the order of an hour or more, depending on the LN_2 supply tank pressure.

To more rapidly bring the system down to cryogenic temperatures, a bypass was installed prior to the pin-fin manifold inlet temperature and pressure fitting, as diagrammed in Figure 20. This allows a much increased flow of LN_2 (not measured but easily in excess of 15 mL/s), rapidly cooling down upstream components. In addition to this, the exhaust from this bypass is directed through two parallel runs of ¼” copper tubing clamped on either side of the copper pin-fin manifold before venting to atmosphere where the tubes emerge from the aerogel insulation. In this way the pin-fin array itself is brought down to cryogenic temperatures during a span of several minutes. Upon closing the bypass valve, the liquid-vapor front is now past the pin-fin array. Thus the fluid passing through the array is mostly liquid, dramatically reducing the pressure needed to drive a desired mass flux. With the heater off and the 50 psig tank, the flow obtained through the loop was 2.8 mL/s of liquid – or 2.25 g/s – with a pin-fin manifold inlet-to-outlet pressure drop of 214 kPa (with a further 55 kPa being dropped from outlet to ambient within the evaporative heat exchanger and outlet tubing).

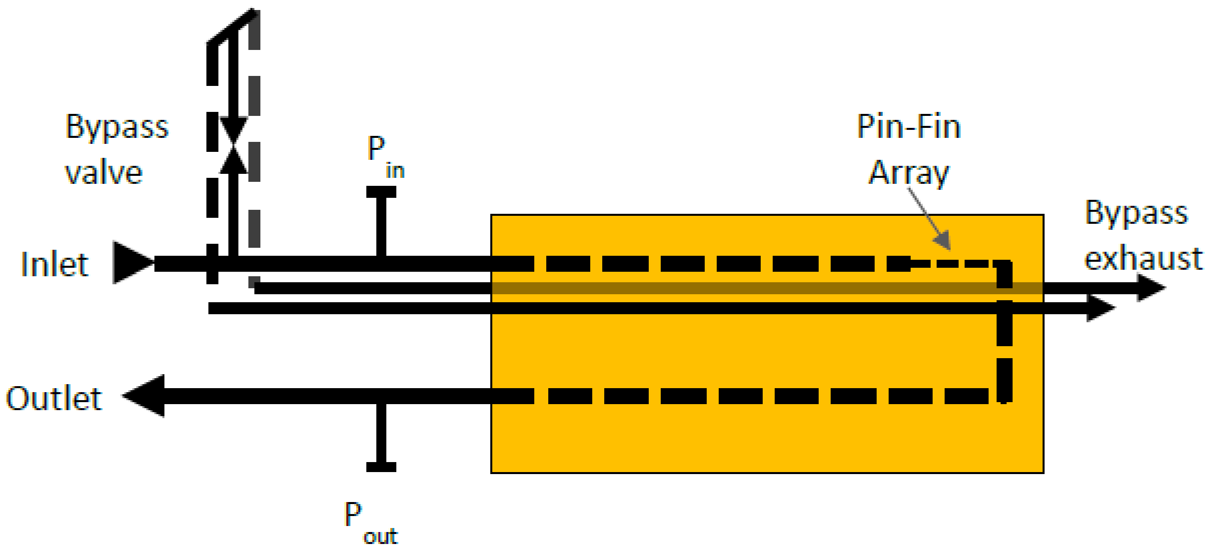

Figure 20: Diagram of Bypass/Blowdown Flow Modification

Opening the bypass valve directs liquid and vapor N_2 through tubing mounted on outer surface of cooler manifold.

2.3 Performance of Cryogenic Microcoolers

2.3.4 Micro Pin-Fin Array Initial Two-Phase Testing

With the higher pressure tank and the flow loop modification allowing adequate liquid delivery to the cooler, a set of initial heater-based tests was conducted. From the outset, an encouraging observation was that even with substantial heater power, the temperature rise measured by the embedded thermocouples remained below 3 to 4°C, indicating the feasibility of using the system to maintain an LD bar at cryogenic temperatures. Figure 21 quantifies this result with the cooler manifold conductance for three stable high-power operating points, with the chip heater driving voltage set to 40, 60, and 70 Volts. The chip power (voltage-current product) is used with the measured flow rate at each point to estimate the change in fluid quality just as with the cold plate testing. The 40, 60, and 70 Volt cases correspond to the 7.5%, 19%, and 30% quality points in Figure 21 (chip power of 31, 70, and 96 W, respectively). The thermal conductance of the pin-fin array is defined as the chip power divided by the average temperature rise of the three embedded manifold thermocouples located just above the pin-fin heated wall (see Figure 23) with respect to the zero chip power case. This is the best way to estimate the wall temperature rise with respect to the local fluid saturation temperature with the given thermocouple locations. In Section 3.4 additional thermocouple locations are added that provide a more accurate instantaneous wall superheat measurement.

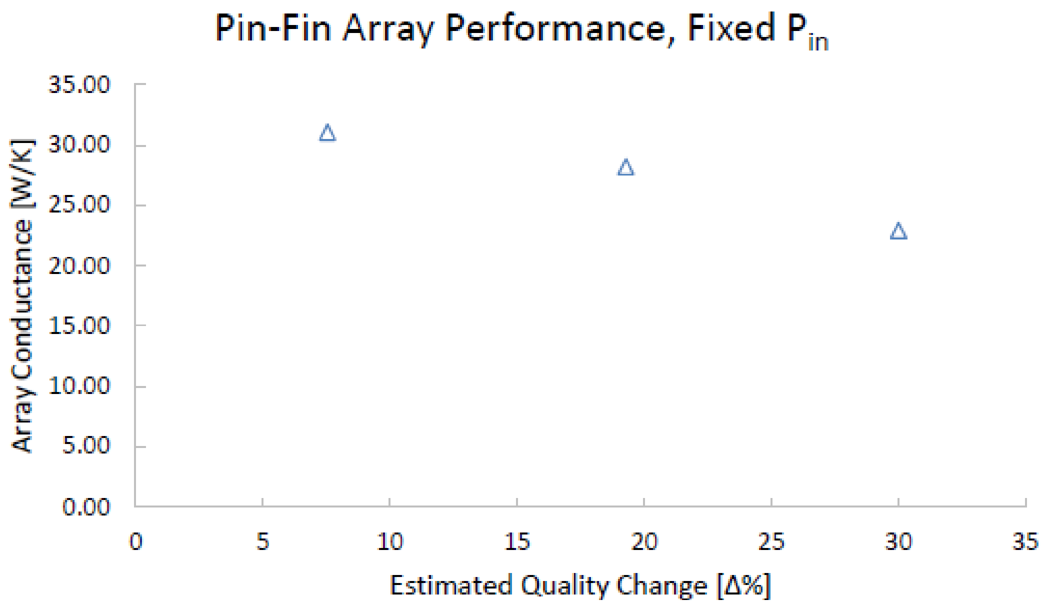

Figure 21: Pin-Fin Array and Manifold Conductance as a Function of Estimated Fluid Quality Change

Inlet pressure is fixed at 370 kPa absolute, manifold outlet pressure increases with quality due to increased pressure losses.

Normalizing this array conductance by the 1.14 cm^2 footprint of the array (dimensions shown in Figure 22) results in the very large value of ~250,000 W/m^2-K base equivalent heat transfer coefficient. However, there are two primary uncertainties involved in the calculation of this value. The first is that the 5 mm upper manifold insert that lies between the chip heater and the pin-fin array operates as a thermal spreader, allowing a portion of the chip power to conduct to parts of the copper manifold far from the array and substantially increasing the "wetted" area for heat transfer to the flowing nitrogen. While this is obviously of benefit in keeping the heater as cold as possible, it means that using the 1.14 cm^2 footprint of the array is a substantial underestimate of the effective cooling area, which could, perhaps, be as much as twice as large. The other uncertainty is in knowing precisely what the nitrogen saturation temperature is at the array. While the thermocouple readings in the unpowered case provide a good estimate of the saturation temperature, powering the chip alters the static pressure within the array, changing the saturation temperature. Allowing for a ±1°C uncertainty in this temperature contributes a ±30% uncertainty in the heat transfer coefficient, due to the low (3 to 4°C) temperature rise observed.

In future studies addressing these uncertainties can be done on two fronts. Uncertainty in T_{sat} can be reduced by embedding thermocouples below the pin-fin array, where a zero-flux condition can be assumed at the lower wall. To accurately predict the portion of chip power dissipated through the array itself, numerical modeling – calibrated with the available temperatures and used to determine the local heat fluxes and wall temperatures - may be the most straightforward approach. Additional thermocouple wells were drilled in the manifold for the final LD bar testing. These thermocouple locations are shown in Figure 23.

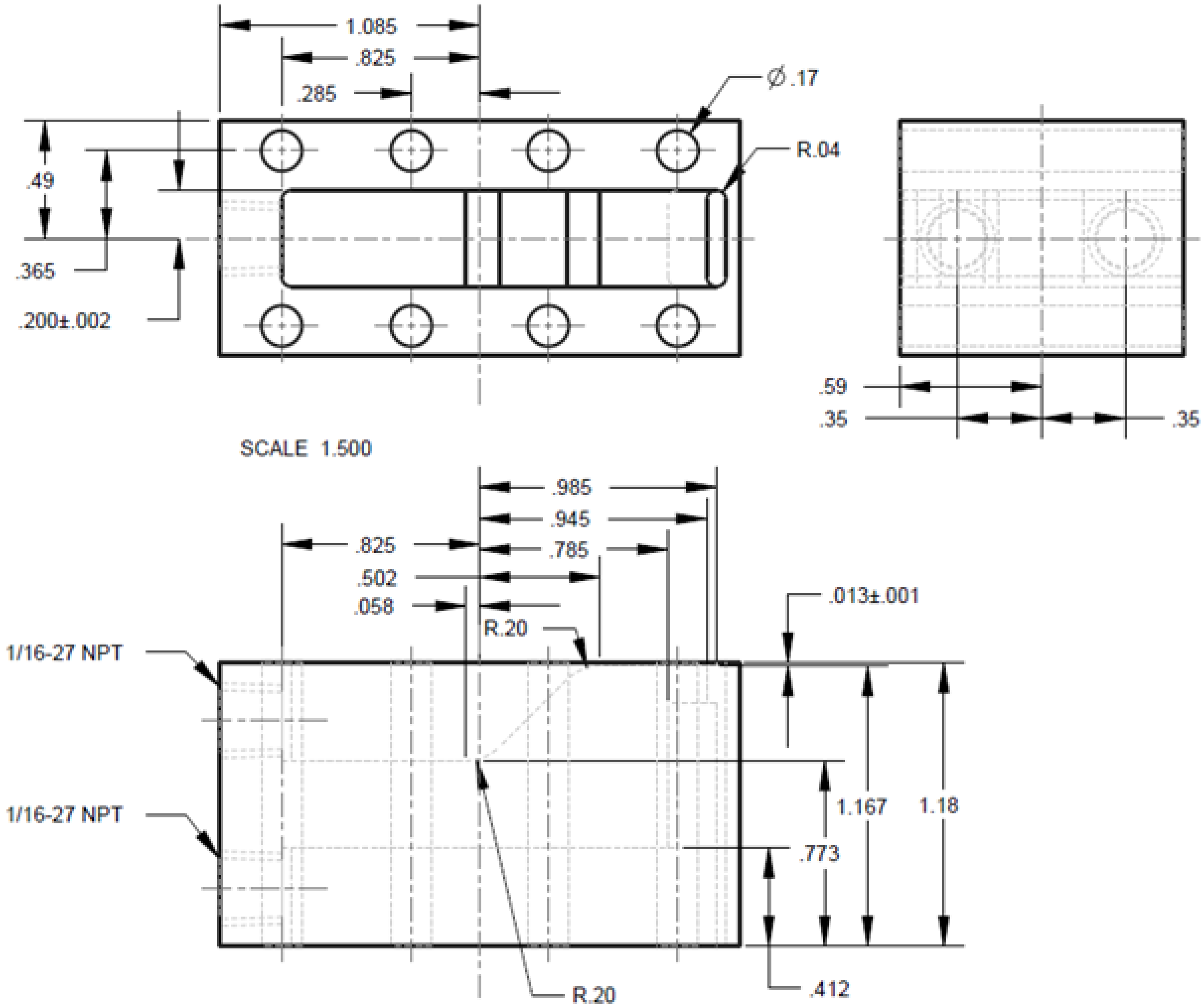

Figure 22: Central Manifold Block Dimensions (inches)

The footprint of the array and/or microgap are computed from the wetted dimensions of the restriction created by this part, 0.4” wide x 0.443” long, with 0.013” (300 µm) gap height.

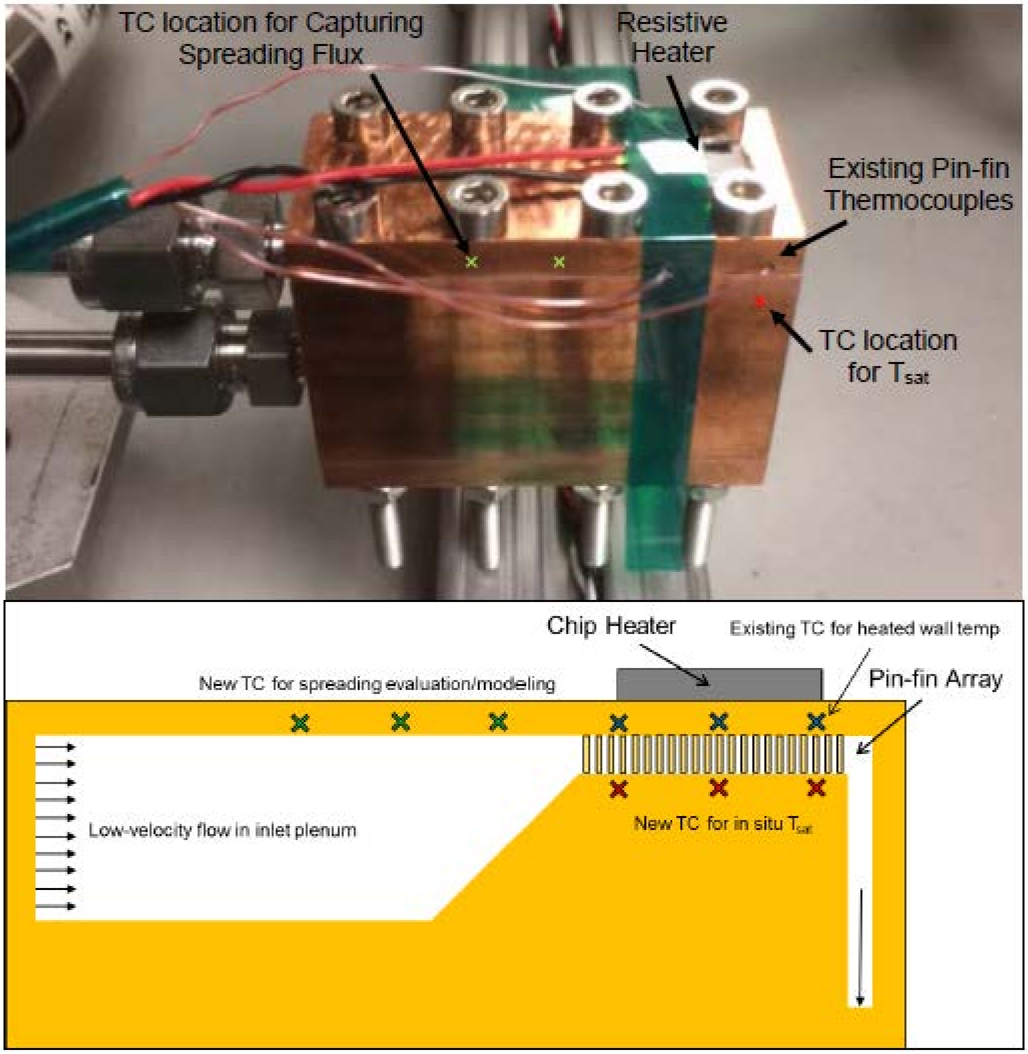

Figure 23: Thermocouple Locations on the Micro Pin-Fin Cooler Manifold

A challenge encountered in the current pin-fin flow loop is that a fixed inlet pressure is available from the LN_2 tank, rather than a user-selectable fixed flow rate that would be obtained from a positive displacement pump. This means that without any flow control within the loop the flow through the pin-fin array varies as chip power is applied due to an increasing pressure differential. Plotted in Figure 24 is the nitrogen mass flowrate as a function of applied chip power.

Heat dissipated from the chip vaporizes increasing amounts of LN_2, leading to increased pressure drop from both the expansion and acceleration of the gas phase. At 80 volts of chip power (126 W), the decrease of flow is sufficient to cause a runaway increase in pressure drop as falling mass flow leads to higher exit quality, leading to additional pressure loss which eventually pushes the vaporization front upstream of the pin-fin array. With only N_2 vapor as the coolant, the heater temperature rises continuously. Fortunately, unpowering the chip heater leads to a gradual recovery of liquid flow in a matter of minutes, indicating that there is sufficient thermal mass in the manifold block to avoid the need to restart the bypass and blowdown procedure. An automated flow control method would be able to prevent this flow instability, but would need to down- regulate heater power if a prescribed maximum pressure differential is reached. Fortunately for the LD bar cooling application, 126 W is well over the expected thermal dissipation to be managed, by a factor of 2 or more.

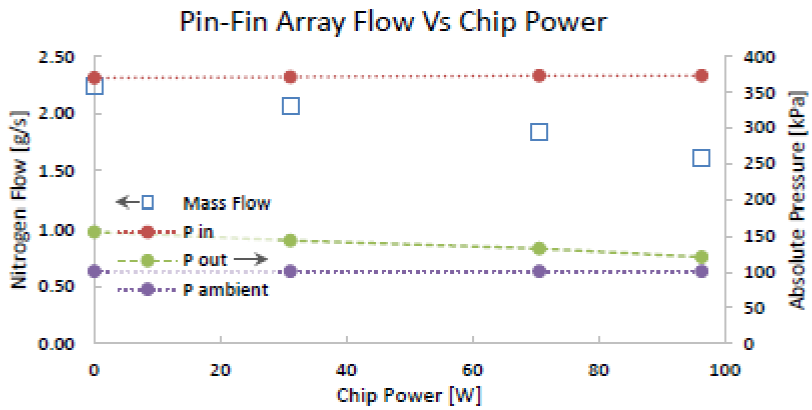

Figure 24: Fluid Mass Flow Rate as a Function of Applied Chip Heater Power (left axis) and Absolute Pressure at Manifold Inlet, Outlet, and Ambient (flow loop outlet at gas flowmeter) (right axis)

2.3.2 Microgap Two-Phase Testing

Two-phase microgap testing was undertaken due to two motivations. First it offers a simple, low-pressure alternative to the pin-fin array that could be tested prior to the solution delivered by the bypass loop modification. Second, the simplified geometry and longer history of use compared to micro pin-fin arrays means that the two-phase correlations that will be compared to experimental results are simpler and more mature than those for pin-fins. Due to the modular nature of the pin-fin manifold design, undertaking microgap experiments required only the interchange of the upper and lower manifold inserts. The pin-fin array is "stored" within the lower outlet plenum, protecting it from damage while having negligible impact on the nitrogen flow. The only modification made was the addition of three new thermocouple holes to capture the heated wall temperature of the new microgap. This gap has the same height as the pin-fin length plus clearance height: 330 μm.

Because the pressure drop across the microgap is substantially less than that for the pin-fin array, no startup bypass procedure is necessary. Furthermore, because heater-induced variation in pressure drop is also decreased, it is much more straightforward to regulate mass flowrate using the pressure venting valves on the LN_2 tank, meaning data can be taken at constant flow conditions without a more elaborate flow control system. As a preliminary test of two-phase microgap cooling, results were collected at two nominal flow rates of 3.2 g/s and 2.3 g/s at different chip heater powers ranging from 0 – 60 W. The results are presented in Figure 25 through Figure 28.

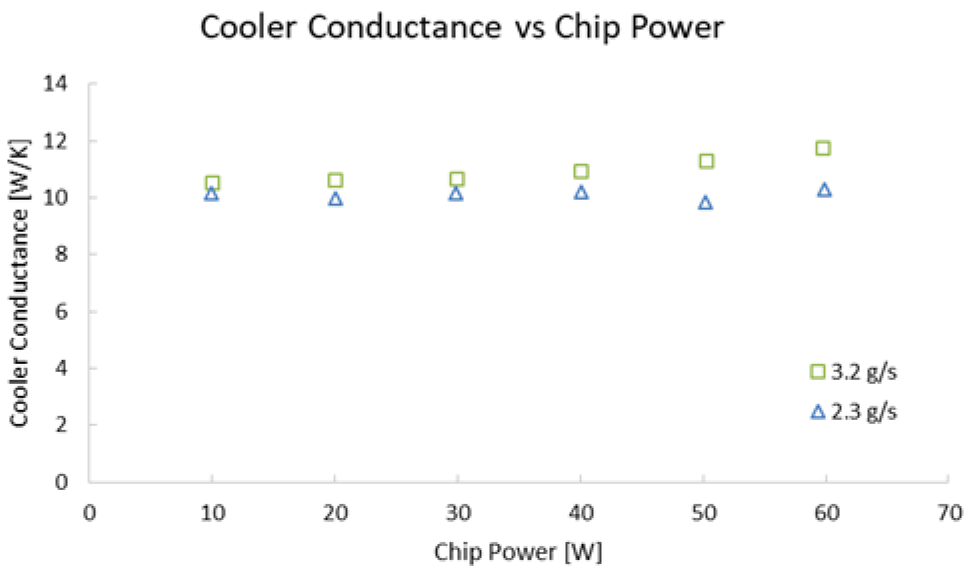

Figure 25: Microgap Cooler Heat Transfer Coefficient as a Function of Wall Heat Flux for Two Mass Flowrates

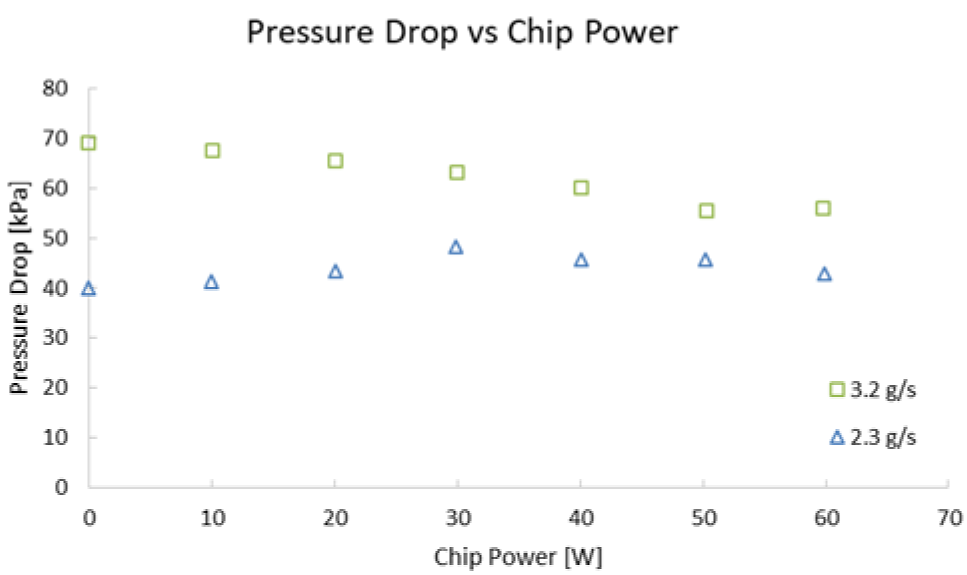

Figure 26: Microgap Cooler Pressure Drop as a Function of Wall Heat Flux for Two Mass Flowrates

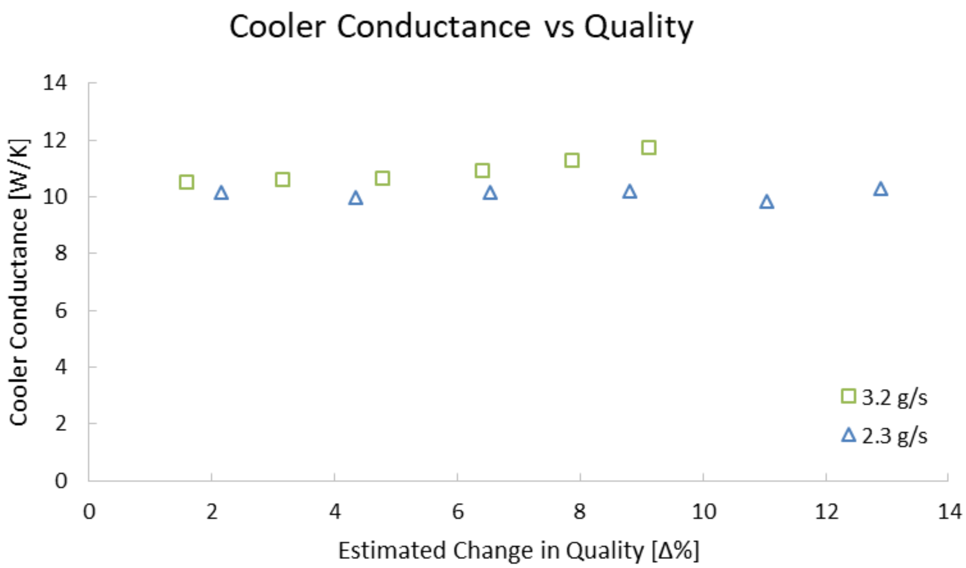

Figure 27: Microgap Cooler Heat Transfer Coefficient as a Function of Change in Vapor Quality for Two Mass Flowrates

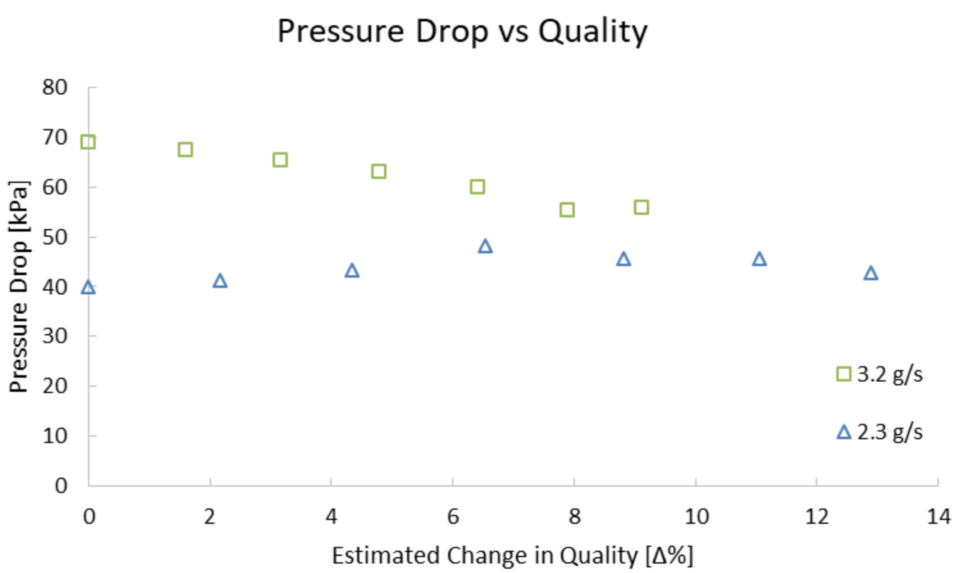

Figure 28: Microgap Cooler Pressure Drop as a Function of Change in Vapor Quality for Two Mass Flowrates

In these tests, the cooler conductance is defined the same way as in the pin-fin testing: the average of the temperature rise experienced by the three thermocouples located at the heated microgap wall with respect to the unpowered condition. If the measured conductance of the microgap cooler were to be normalized by the same 1.14 cm^2 as the pin-fin array, the resulting equivalent heat transfer coefficient is ~100,000 W/m^2-K. As with the pin-fin array, these equivalent values are likely higher than the actual local values since thermal spreading within the upper insert provides a parallel path to parts of the manifold block in contact with (albeit slowermoving) LN_2 fluid. This spreading path is likely to have increased participation relative to the pin- fin application due to the lower effective heat transfer coefficient, *h*, of the microgap, which leads to elevated wall and heater temperatures compared to the pin-fin array. Also present are the same sources of uncertainty in estimating local T_{sat} within the gap, although the lower pressure variation coupled with the higher temperature differentials lead to a lower preliminary uncertainty of ±20%. The same measures proposed for mitigating pin-fin T_{sat} and spreading uncertainty can be applied to microgap testing. Despite these uncertainties, one indication that appropriate operation is being obtained is that the ratio of pin-fin to microgap cooler conductance (and by extension heat transfer coefficients) is between 2.5 – 2.8, which is very close to the 2.75 time area enhancement offered by the pin-fin array over the microgap

Regardless, the obtained cooler conductance of 11 W/K indicates the even the microgap cooler is certainly capable of managing a substantial amount of dissipated power. Identifying the thermal resistance from emitter-to-nitrogen: R_{LD} is 0.8 K/W, R_{attach} estimated at 0.24 K/W for silver grease, R_{copper} is $\frac{5mm}{400W/m-K*12mm*12mm}$ = 0.09 K/W and R_{cooler} is 0.09 K/W results in a total resistance of 1.22 K/W, of which the microgap cooler is less than 10%. This is a particularly interesting result: until the other resistances between the emitter and nitrogen are addressed (i.e. by integrating the emitter chip and submount on the cooler surface, rather than relying on a separate conduction bar), a microgap may be sufficient is preventing the convection resistance from becoming the thermal bottleneck.

One drawback, however, is that although the microgap is simpler and presents a much lower pressure drop than the pin fins, its performance is measured at generally higher mass flow rates than those required for the pin-fin array. Higher flow means the exit quality is lower than the in the case of the pin-fin array, indicating that a smaller portion of the available coolant is being used for thermal management. This is a particular issue considering the open loop configuration of the LN_2 flow apparatus, and represents a large loss in overall efficiency unless the un-vaporized coolant can be put to further use downstream of the microgap in any eventual application. Redesigning the flow apparatus to deliver lower flow rate and thus higher exit quality will provide insight on whether the microgap maintains similar performance compared to high-flow conditions.

One final consideration identified in the preliminary testing can be seen in the pressure curves plotted in Figure 26 and Figure 28. The tests were conducted with the high flow first, moving from high to low chip power. This was done because flow control by tank venting is relatively responsive when lowering tank (and thus inlet) pressure, but requires time for pressure to build back up to regain high pressures. For the 3.2 g/s flow, as chip power was reduced the vapor quality exiting the cooler decreased, meaning more LN_2 need to be evaporated within the water-stabilized heat exchanger before exhausting to the gas flowmeter. For the lowest power tests, this eventually overwhelmed the heater responsible for water temperature control: the reservoir water temperature was less than 10°C, and icing was visible on the outer surfaces of the heat exchanger. N_2 exhaust temperature prior to the flow meter decreased to 150 K by the 10 W operating point, well outside the accurate range of the gas flow meter. It is likely mass flow was substantially higher than measured 3.2 g/s (3.9 mL/s), as evidenced by the increasing pressure as chip power was reduced. The flow loop was shut down and water temperature allowed to recover before proceeding with the 2.3 g/s testing, which displayed relatively constant pressure drop.

Exhaust temperature for the 2.3 g/s testing remained above 280 K for the entire test run. The lesson is that for high LN_2 flow testing, additional care is necessary in monitoring the auxiliary components of the flow loop.

2.4 Application of Cryogenic Microcoolers for High-Power LD Bar

2.4.2 LN_2 Cooled Laser Diode Bar Experimental Setup

The laser diode bar was fixed to the micro-pin fin cooler following the initial ceramic heater cooler characterization tests. Shown in Figure 29 is the DILAS conduction cooled laser diode bar, along with the locations where additional thermocouples were placed for measurements during the experiments.

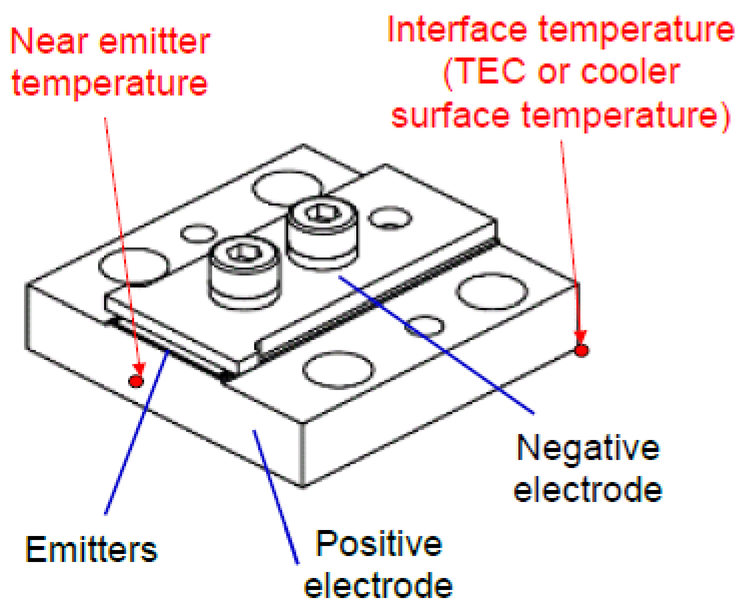

Figure 29: DILAS Conduction Cooled Laser Diode Bar

The characteristics of this LD bar are as follows: 19 identical GaAs emitters, each with a width of 100 μm with a center-to-center spacing of 500 μm between emitters, yielding a fill-factor of 20%. The length of the chip is 2000 μm, with an active epitaxial layer thickness of 4.6 μm grown on a chip substrate thickness of 107 μm. This chip is attached to positive copper electrode with indium solder with a layer thickness of 10 μm. The maximum optical power is 65 W at 62.5 A, with a center wavelength of 976 nm +/- 10 nm and an overall efficiency of 63.4%. The spec sheet thermal resistance from the junction to the copper block is 0.8 K/W.

Figure 30 shows the LD bar mounted on top of the micro-pin fin cooler using the four mounting bolts, situating the emitter in the vicinity of the micro-pin fin array, and directing the beam towards the optical power sensor (not shown). The ends of copper bypass exhaust tubes were then angled outward to avoid exhausting directly onto the power meter.

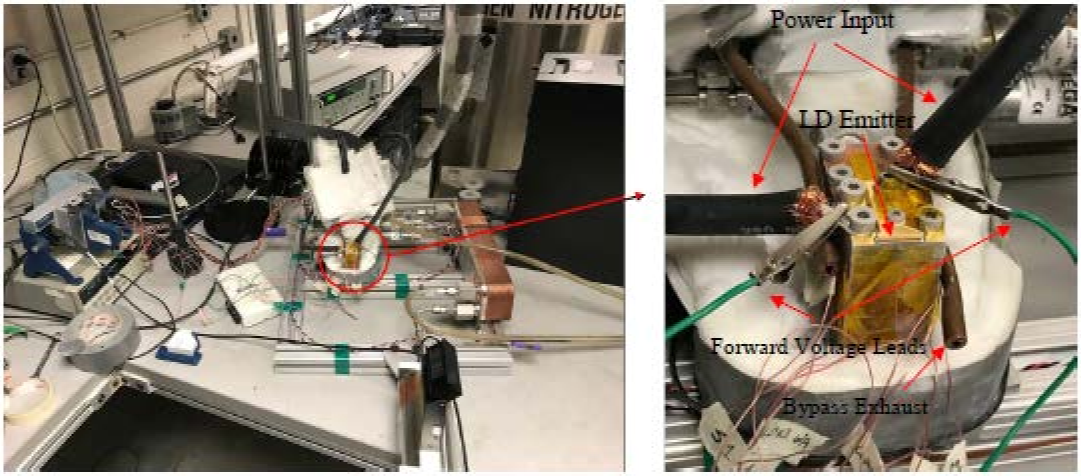

Figure 30: Nitrogen Flow Loop with DILAS LD Bar Mounted on Micro-Pin Fin Cooler

A single test cycle using the LD bar consisted of a room temperature startup of the LD bar (powered at 60 A), shortly followed by nitrogen flow through both the pin fin array and the bypass. This was done to reach a near-emitter temperature of 46°C before cooling progressively to cryogenic temperatures. 46°C is the measured near-emitter temperature during a reference test using a thermoelectric temperature-controlled stage held at 25°C and a LD current of 60 A, which is the standard operating conditions specified in the LD bar data sheet. The flow of nitrogen through both the bypass and pin fin array is adjusted to slowly bring the cooler and LD bar temperature down to cryogenic temperatures and allow two-phase flow to be established fully in the pin fin array. At this point the temperature at the interface between the cooler and the LD bar is about -180°C. The cooldown – which occurs over 10 to 15 minutes – is assumed to be slow enough that the effects of transient temperature change on the diode emitter can be neglected. The LD bar power and efficiency measurements are thus treated as quasi-steady state.

Figure 31 illustrates some of the considerations encountered during the cryogenic tests. In order to provide access for the LD bar power input and allow a path for the beam output, the aerogel insulation had to be rolled back from the end of the cooler. As the cooler reaches subzero temperatures ice begins to build up on exposed surfaces, including the LD bar and its emitting surface. Preliminary cryogenic tests revealed that once this emitter ice buildup occurs measured optical power drops markedly. To combat this a nozzle directing nitrogen gas towards the emitter in a shield plume was installed above the cooler. This nitrogen was sourced from the head space in the LN_2 supply tank, and so was also at cryogenic temperatures. In this way the shield gas attempts to reduce the impact of the ambient temperature and humidity on cooler operation.

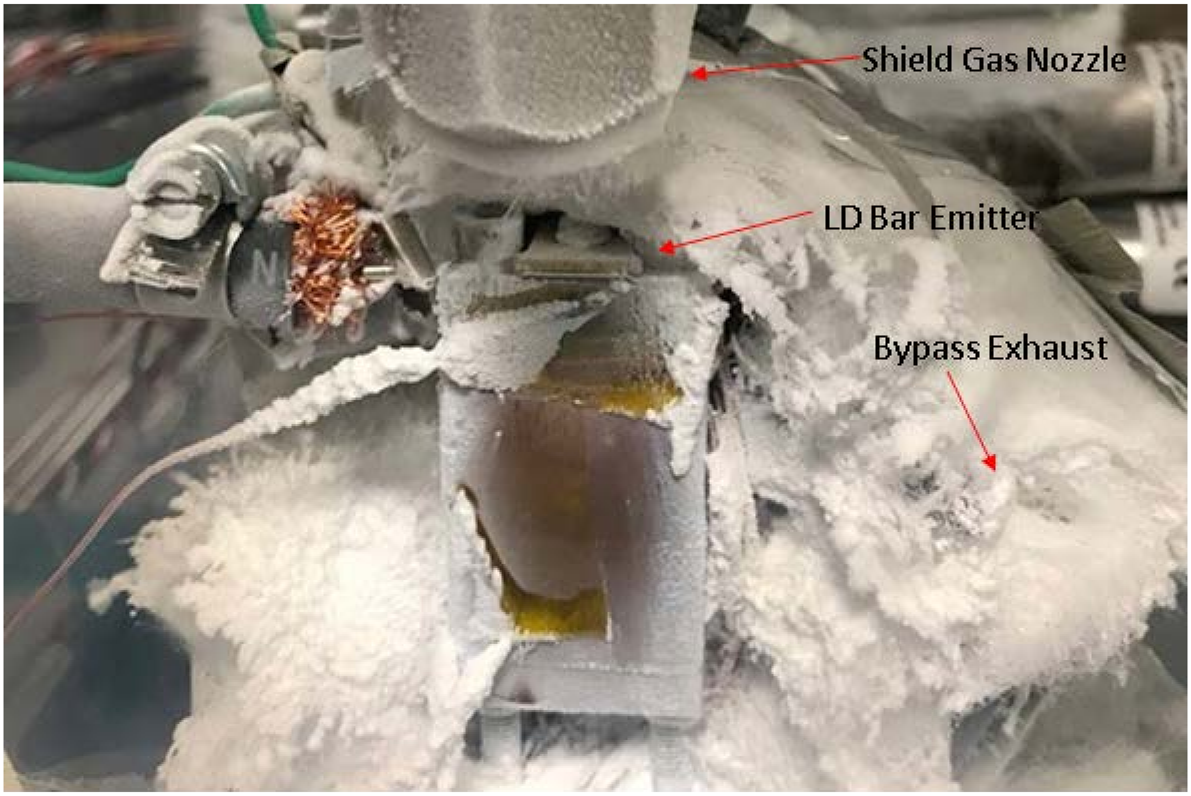

Figure 31: Cooler and LD Bar at the End of a Test Cycle

2.4.3 LN_2 Cooled Laser Diode Bar Experiment Results

Figure 32 shows experimental results for two separate cryogenic cycles on an LD bar run at 60 A emitter current. Measured power values are plotted as a function of the cooler/conduction block interface temperature, providing a comparison to measurements made using the 25°C thermal stage. Cycles proceeded from room temperature to cryogenic temperature, i.e. from right to left on the plots in Figure 32.

As temperature decreased, the input electrical power rose as the diode forward bias voltage increased (from 1.55V at 25°C to 1.83V at -180°C). For the first portion of each cycle, the measured output optical power increased with decreasing temperature up until an interface temperature between -75 to -100°C, where it peaks at 68.9W. Measured output power then fell as temperatures dropped further, even falling below levels measured at room temperature. These reductions in measured power coincided with progressive ice film accumulation that occurred despite the nitrogen shield gas. The interpretation is that ice buildup on the emitter surface occludes and/or scatters the emitted beam, and moreover that differences in the icing process accounts for the discrepancy between data from individual tests. This beam interference manifests as a reduction in the effective power efficiency of the LD bar in terms of optical power delivered to the power meter, as seen in the second plot of Figure 32. The peak effective power efficiency in each run was 68.9% and 68.4%, respectively, occurring at an interface temperature of -50°C.

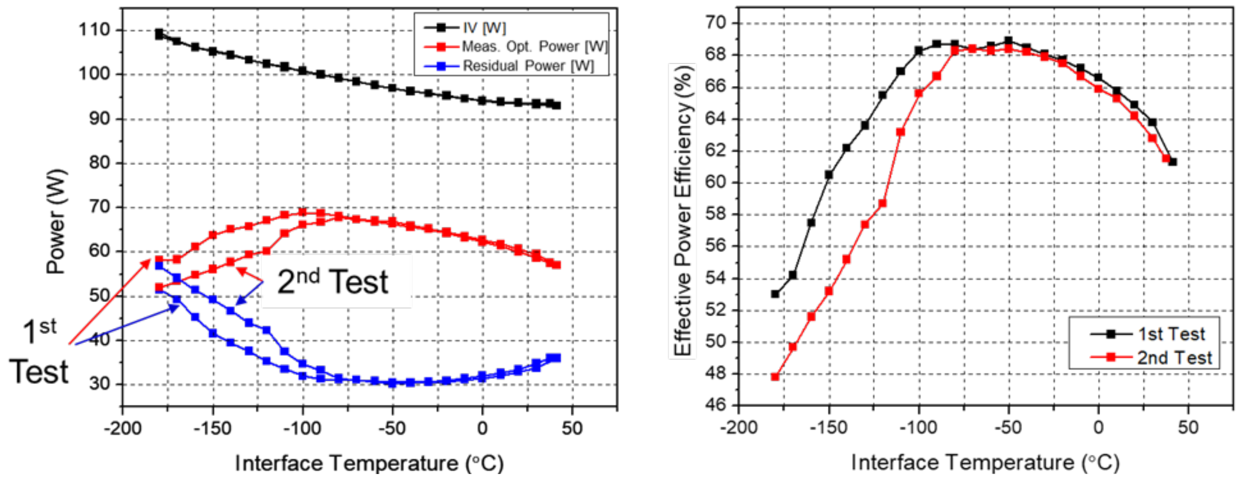

Figure 32: Test Data for Two Cryogenic Cycles on an unused LD Bar

The discrepancy between the electrical input power and the measured optical power is recorded as the residual power not transmitted to the optical target. At temperatures above -50°C this power is identified as the LD bar thermal dissipation, but after an ice film is generated it remains an open question if the entirety of the residual power goes to heating the LD bar or if some is scattered and unaccounted optical power.

Accounting for this power in the thermal operating characteristics of the cooler is complicated by the unknown heat transfer facilitated by the shield gas jet, the bypass tubing, and ambient. An example of this is cooler operation at -25°C where an energy budget is presented in Figure 33, before ice film generation and when the flow in the pin fin array is entirely single-phase gas. Because the nitrogen at the cooler inlet and outlet is superheated gas, calculating the net heat removal is a matter of computing the net enthalpy flow, while the absence of ice means the 30W LD bar residual power can be completely ascribed to thermal dissipation. Comparing these energy rates to the rate at which the cooler/LD bar mass cools down highlights a 40 – 50 W discrepancy, which is attributed to the cooling effect of the cold shield gas jet and the nitrogen flowing through the bypass. As temperatures continue to fall, this cooling effect will decrease as the exposed surfaces of the cooler/LD bar become closer to the gas jet and bypass temperatures and further from the ambient temperature.

Energy Input	-	**Energy Output**	$\pm$ **Discrep.**	=	**Energy Accum.**
IV, **95W**		P_{opt}, **65W**			Heat Capacity, Cu manifold and LD bar 70 J/K
Enthalpy Flow 0.36 g/s N_2 $\dot{h}$ flow in (290kPa, 89.4K→ h = 101.4 J/g) **37W**		0.36 g/s N_2 $\dot{h}$ flow out (110kPa, 268K→ h= 278.5 J/g) **100W**			Cooldown Rate | -25°C -1.1 K/s
Totals **132W**	-	**165W**	Additional Removed $\boxed{-44W}$	=	**- 77W**

Figure 33: Energy Budget for LD Bar Cooler Operation at -25°C Interface Temperature

Below -25°C interface temperature this calculation is made more complicated as the nitrogen at the cooler inlet reaches saturation. As the inlet flow quality is unknown, the internal heat removal rate cannot be estimated. However, once the cooler outlet also reaches saturation (at an interface temperature of -180°C), the flow in cooler is fully two-phase, picks up to a mass flow rate of ~2 g/s, and reaches steady state. At this point the cooler operation can be compared to the tests performed with the ceramic chip heater where the internal cooler conductance was measured to be about 30 W/K. The measured wall superheat at this point is 1.5±0.5K, suggesting that the cooler is removing between 30 and 60 W. The residual LD power is between 50 and 60 W, indicating that on the order of 10W is unaccounted for. This power may have been removed by the bypass and shield jet, or as scattered optical power not captured by the optical power meter.

2.5 References for Part I

[1] S. Krishnamurthy, Y. Peles, “Flow boiling of water in a circular staggered micro- pin fin heat sink”, Int. J. Heat Mass Transfer 51 (2008) 1349–1364.
[2] A. Reeser, A. Bar-Cohen, and G. Hetsroni, "High quality flow boiling heat transfer and pressure drop in microgap pin fin arrays," International Journal of Heat and Mass Transfer, vol. 78, pp. 974-985, 2014.
[3] Rahim, E., and Bar-Cohen, A., 2015, "Thermal Characteristics of a Chip-Scale Two-Phase Microgap Cooler," Heat Transfer Engineering, 36(5), pp. 511-520.
[4] Bar-Cohen, A. and Holloway, C., 2016, “Thermofluid Characteristics of High Quality Flow in Chip-Scale Microgap Channels”, IPHT Journal Vol 3, Issue 4, January.
[5] S. L. Qi, P. Zhang, R. Z. Wang, and L. X. Xu, "Flow boiling of liquid nitrogen in micro-tubes: Part II – Heat transfer characteristics and critical heat flux," International Journal of Heat and Mass Transfer, vol. 50, pp. 5017-5030, 2007.

3. PART II: POF-BASED RELIABILITY ASSESSMENT OF LD/MICROCOOLER SUBASSEMBLY SUBJECTED TO CRYOGENIC OPERATING CONDITIONS

3.1 PoF Model for LD/Microcooler Subassembly

The concept of a hierarchical PoF-based reliability assessment model is proposed. The model is shown in Figure 34 for the LD bar cooled by the cryogenic pin-fin cooler. The LD bar is eventually used as an optical power source for a fiber laser. The failure of the fiber laser can be separated by catastrophic optical mirror damage from the LD bar and gradual degradation of the optical power. For the gradual degradation, there is no standard failure criterion. We have decided the failure criterion for the gradual degradation when the optical power is less than 80% of the initial optical power.

The gradual degradation of the optical power governed by the pumping efficiency. The pumping can be affected by optical reliability and LD bar reliability. The optical reliability is related to degradation of fiber (lasing medium) and coupling efficiency. The LD bar reliability is governed by optical power change from chip degradation, center wavelength shift, spectrum width change, and beam divergence and near-field linearity. The beam divergence and near-field linearity also affect the coupling efficiency in the optical reliability.

The LD bar reliability is mainly affected by the junction temperature distribution, which is governed by the thermal reliability. When the forward current, inlet coolant temperature, and flow rate are determined from the operation input, the LD bar have the initial junction temperature distribution. The thermal reliability affects the junction temperature distribution. The thermal reliability can be separated by thermal conduction resistance of the die attach and the heat transfer coefficient of the cooler. The thermal conduction resistance of the die attach can be increased by voids from the electromigration or cracks from the thermal fatigue. The heat transfer coefficient of the cooler can be degraded by erosion, corrosion, clogging in the pin-fin channel.

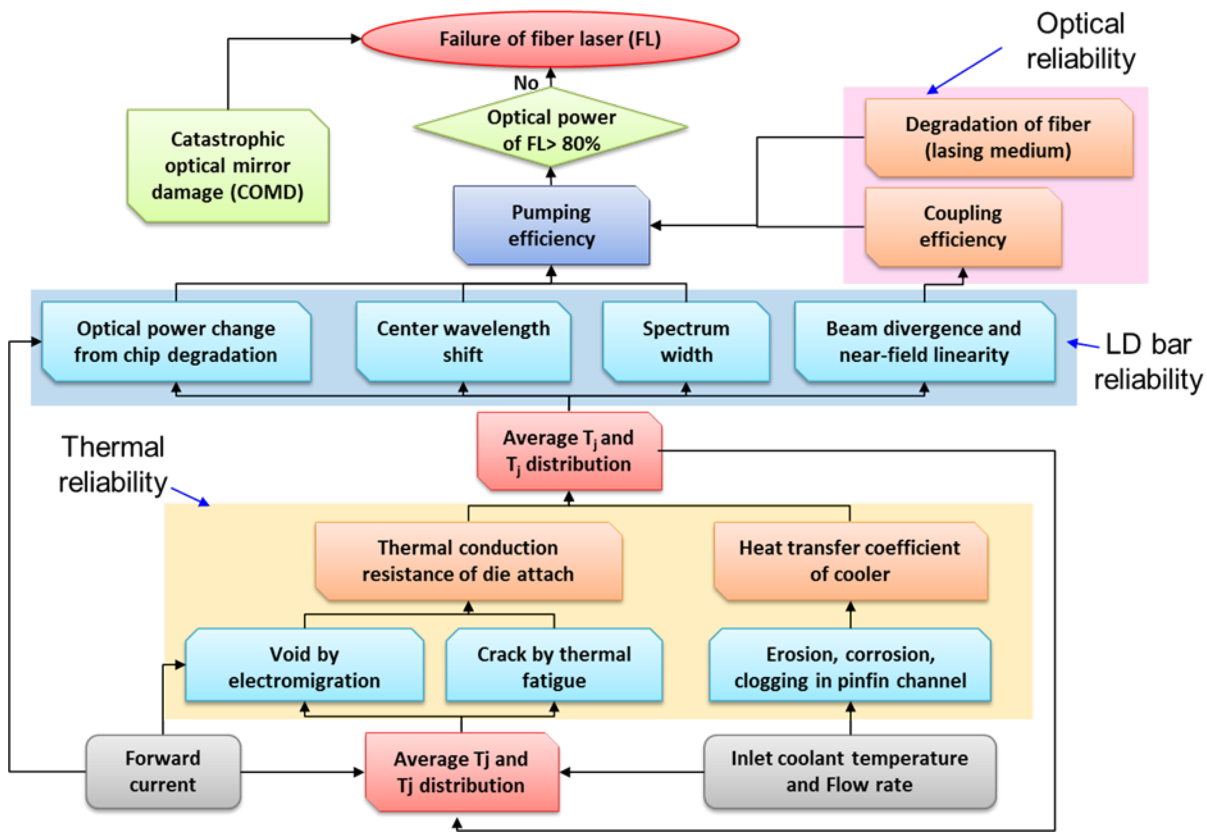

Figure 34: Hierarchical Life Prediction Model for the Cryogenic Pin-Fin Cooled LD Bar

In this study, the crack propagation in the die attach due to the thermal fatigue and its effect on the SPD) change are demonstrated for the PoF-based reliability assessment. First, the junction temperature distribution measurement is essential as the initial step. A hybrid experimental/numerical method is proposed to predict the junction temperature distribution of a high power LD bar (Section 3.2). In Section 3.3, a novel method is proposed to predict the SPDs of individual emitters by deconvoluting the SPD of an LD array. Eventually, this method can be utilized to predict the SPD change from the crack propagation of the LD bar. In Section 3.4, the crack propagation in the die attach due to the thermal fatigue and its effect on the spectral power distribution change are demonstrated for the PoF-based reliability assessment.

3.2 Method for Predicting Junction Temperature Distribution in High-Power LD Bar

A hybrid experimental/numerical method is proposed for predicting the junction temperature distribution in a high power LD bar with multiple emitters. A commercial water-cooled LD bar with multiple emitters is used to illustrate and validate the proposed method. A unique experimental setup is developed and implemented first to measure the average junction temperatures of the LD bar emitters. After measuring the heat dissipation of the LD bar, the effective heat transfer coefficient of the cooling system is determined inversely from the numerical simulation using the measured average junction temperature and the heat dissipation. The characterized heat dissipation and effective heat transfer coefficient are used to predict the junction temperature distribution over the LD bar numerically under high operating currents. The results are presented in conjunction with the wall-plug efficiency and the center wavelength shift.

3.2.1 Introduction

As higher optical power is demanded for advanced applications, more closely-spaced emitters with higher forward current are used in LD bars. As a result, the junction temperature from the center to the edge emitters may have large variations, which makes the center wavelength and wall-plug efficiency of each emitter different from each other.

Several junction temperature measurement methods for low power LDs or light emitting diodes (LEDs) have been proposed, including techniques based on measurement of the thermal resistance [4], wavelength-shift [5, 6], optical power output [5], and forward-voltage [5, 7-14]. These methods are applicable only when the junction temperature is uniform. Micro-Raman spectroscopy [15-17] can be used to measure the junction temperature distribution by measuring multiple local temperatures. In practice, it requires a complicated experimental setup and has limited accuracy (10 to 20°C) [15-17].

3.2.2 Laser Diode System

This section is devoted to the description and the electrical characteristics of a commercial water-cooled LD bar tested in the study.

3.2.2.1 LD Bar Description

The commercial LD bar system (E11.4N-940.10-150C-SO13.1: DILAS) is shown in Figure 35a. The LD bar consists of 23 identical GaAs emitters. The fill-factor is 50%; each emitter is 200 μm wide and has a pitch of 400 μm. The maximum optical power at 160 A is 160 W with a center wavelength of 930 nm.

The close-up view of the side of the LD bar is shown in Figure 35b. The GaAs chip (the epi-down configuration) is mounted on a CuW submount using AuSn die attach. The submount made of CuW (coefficient of thermal expansion (CTE): 6.5 ppm/°C) is placed between the GaAs chip (CTE: 6.4 ppm/°C) and the water-cooled microchannel made of Cu (CTE: 16.6 ppm/°C) for the stress-relieving buffer layer to reduce the thermal stress attributed to the mismatch in the CTE between them as well as for the heat spreader [18-20]. The specified thermal resistance from the junction to water inlet temperature is approximately 0.3 K/W [21]. The internal structures of the commercial microchannel and the interfacial resistance are not available, and thus the effective water heat transfer coefficient for this commercial microcooler cannot be determined.

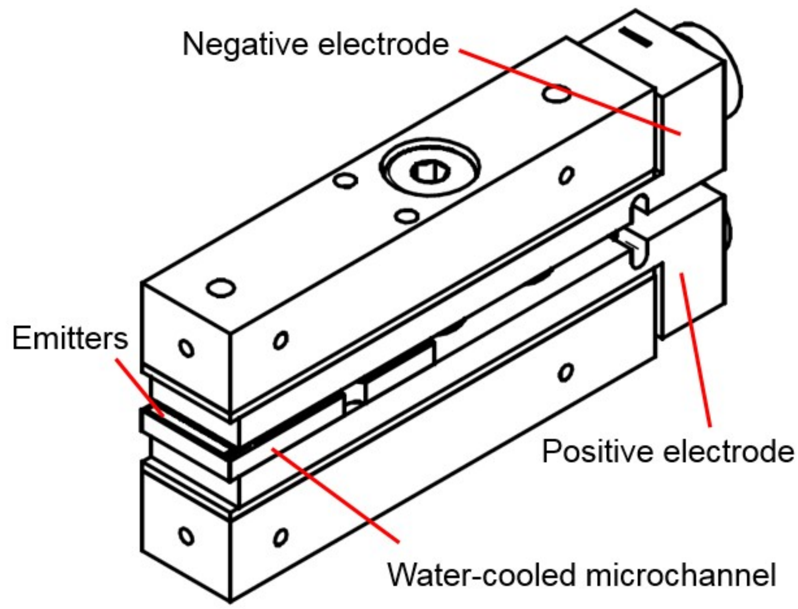

(a)

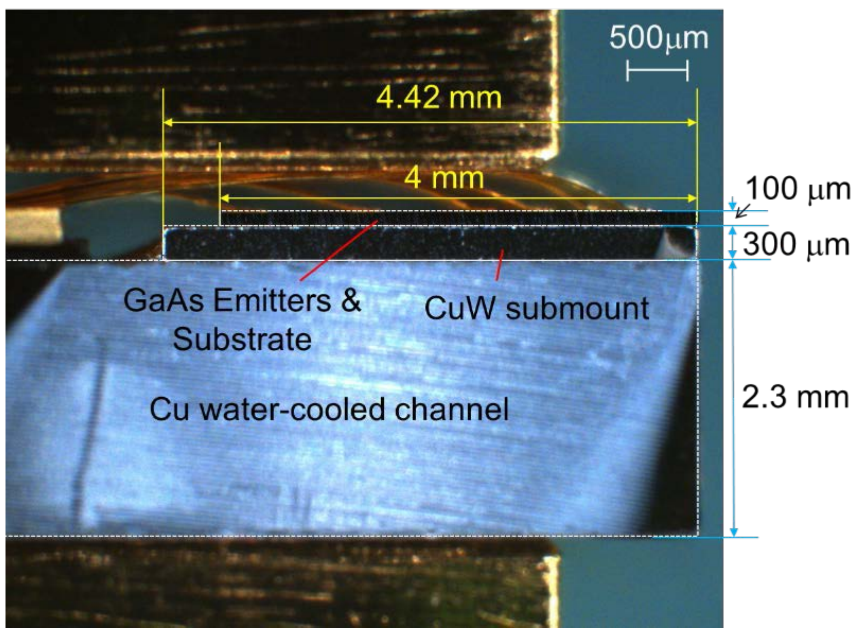

(b)

Figure 35: (a) LD Bar with Water-Cooled Microchannel [21] and (b) Side View of the LD Bar

3.2.2.2 Calibration Curve

It has been known that a negative linear relationship exists between the junction temperature and the forward voltage of a laser diode [7-14]. The junction temperature at the operating current can be measured using this relationship (known as the "calibration curve"), and it is called the forward voltage method [7-14].

The “calibration curve” is obtained using a probe current much lower than the operating current. If the probe current is too low, the forward voltage loses the negative linear relationship at high junction temperatures due to the leakage current effect [22]. On the other hand, if it is too high, the loss of linearity occurs at low junction temperatures due to the internal series resistance [23]. In addition, the probe current should be as low as possible to avoid any undesired junction temperature increase while obtaining the calibration curve. Every LD has somewhat different electrical characteristics. Thus, it is important to determine the lowest probe current that provides the desired linearity [14].

The LD bar was placed inside a convection oven (EC1A: Sun Electronics Systems) and the forward voltage was measured at 25, 35, 45, 55, and 65°C (with an accuracy of ±0.1°C) by a data acquisition module (DAQ: USB-6212: National Instruments) with a 16-bit resolution. The maximum operating junction temperature was estimated, based on the thermal resistance of 0.3 K/W, the inlet water temperature of 20°C, and the measured maximum heat dissipation of 84.7 W (this will be explained further in Section 3.2.5.1), to be 45.4°C. The calibration curve measurement was repeated at various probe current values (from 20 mA to 160 mA with an interval of 20 mA).

The results are shown in Figure 36, displaying the expected linear relationship between forward voltage and junction temperature. The small deviations from linearity in voltage and temperature at 65°C are summarized in Table 1. The junction temperature error gradually decreased as the probe current increased, and remained virtually the same after 120 mA. The probe current of 120 mA generated a heat dissipation of only 142 mW at 25°C (6.2 mW per emitter), which was negligible compared to the heat dissipation produced by the operating current. Thus, the calibration curve obtained at 120 mA was selected for junction temperature measurement. The slope and the y-intercept of the calibration curve were -1.21 mV/K and 1.2104 V, respectively.

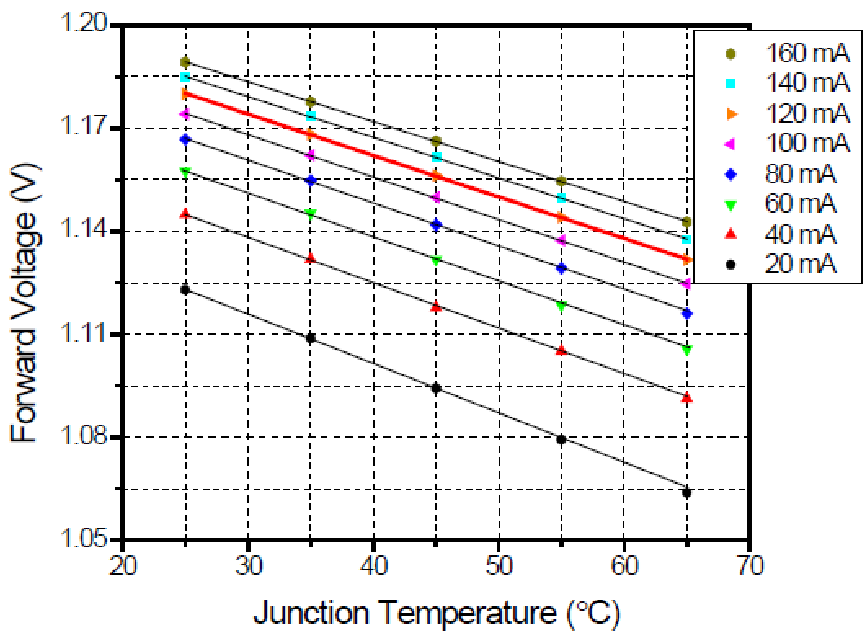

Figure 36: Forward Voltage as a Function of Junction Temperature

Table 1. Junction Temperature Error at 65°C under different Probe Currents

If [mA]	Deviation of Vf (mV)	Error in Tj [°C]
160	0.17	0.1
140	0.16	0.1
120	0.18	0.1
100	0.41	0.3
80	0.78	0.6
60	0.80	0.7
40	0.80	0.7
20	1.60	1.3

3.2.2.3 Electrical Resistance of Single Emitter

The calibration curve is obtained when all the emitters have the same temperature. The emitters of the LD bar are connected in parallel, and thus the electrical resistance of a single emitter (assuming that all emitters are identical) can be determined simply by

$$R(T) = N \times \frac{V_f(T)}{I_{probe}} \tag{1}$$

where R is the electrical resistances of the single emitter [Ω]; Vf is the forward voltage of the LD bar [V] under the probe current, I_{probe} [A]; and N is the number of the emitter (N = 23).

The results obtained for the LD bar at the probe current of I_{probe} = 120 mA are shown in Figure 37. The electrical resistance decreased with the temperature; the change in resistance was only 4% (from 226.2 Ω to 216.9 Ω) over the temperature range from 25°C to 65°C.

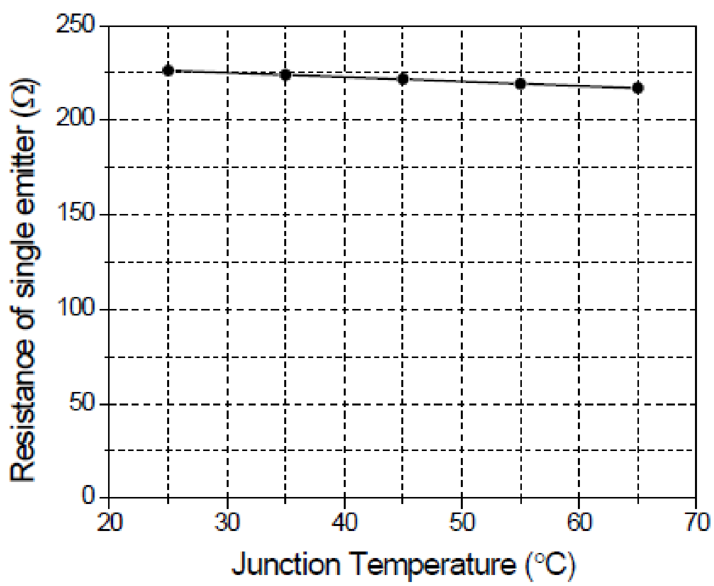

Figure 37: Electrical Resistance of the Single Emitter as a Function of Junction Temperature at I_{probe} = 120 mA

3.2.3 Junction Temperature Measurement

The junction temperature at the operating current can be measured by switching the operating current to the probe current [7-14]. As discussed in Ref. [24], the forward voltage shows the combined behavior of RC delay and thermal delay during the switching time. The RC delay is attributed to the resistance of a LD and the capacitance of a current source.

The LD bar is operated at very high forward currents. A power supply that drives high currents typically has large capacitance, which can cause the large RC delay, and the transient junction temperature behavior of the CuW submount cannot be documented. Fast switching circuits with two separate power supplies have been utilized to reduce the delay [10, 11]. This scheme is adopted for the current study.

3.2.3.1 Test Setup

A test apparatus to minimize the RC delay is illustrated schematically in Figure 38. The operating current source (LDX-36125-12: ILX Lightwave) applies the operating current with a nominal accuracy of ± (0.1% + 120 mA). The probe current source (2401: Keithley Instruments) applies the probe current with a nominal accuracy of ± (0.066% + 20 μA). The two power supplies are connected in parallel.

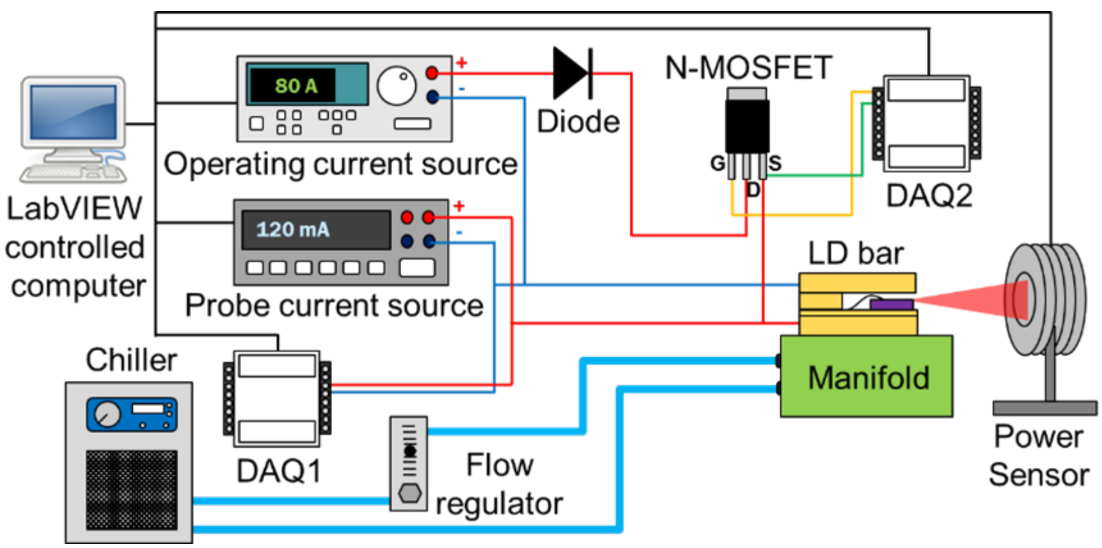

Figure 38: Schematic Illustration of Junction Temperature Measurement Setup

An N-channel metal-oxide-semiconductor field-effect transistor (MOSFET) (IRL7833PBF: International Rectifier Corporation) serves as a switch for the operating current source [10]. The probe current flows from the source (S) to the drain (D) of the N-channel MOSFET, even when the switch is off to block the operating current. A diode (150EBU02-ND: Vishay Intertechnology) is inserted between the operating current source and the MOSFET to prevent this undesired flow. The MOSFET and the diode are mounted on a heat sink to dissipate heat at high operating currents.

The chiller (ISOTEMP I 115V/60HZ PD-1: Fisher Scientific) regulates the water inlet temperature with a temperature stability of ±0.1 °C, and the flow regulator (FLDW3211G: OMEGA Engineering) controls the flow rate. The optical power sensor (USB-PM-150-50: Coherent Laser Group) measures the optical power with a nominal accuracy of ±2.7% in the operating range. The current sources, the DAQs, and the optical power sensor are integrated into a LabVIEW program.

In the actual measurements, the chiller is set to produce the inlet water temperature of 20°C and the flow rate of 16 L/h. The pressure drop from the water-cooled microchannel cooler is 34 psi. The forward voltage measurement is conducted only with the probe current applied to the LD bar. As an example, to apply an operating current of 80 A to the LD bar, the operating current source and the probe current source applies 79.88 A and 120 mA, respectively, with the MOSFET switch "on". When the optical power and the forward voltage of the LD reaches the steady-state condition, the switch is turned off to block the flow of the operating current. The data acquisition module 2 (DAQ2: USB-6212: National Instruments) supplies the gate voltage to the MOSFET switch and the data acquisition module 1 (DAQ1: USB-6212: National Instruments) measures the forward voltage of the LD with 16-bits resolution with the maximum sampling rate of 400 kS/s continuously during the transient period.

3.2.3.2 Average Junction Temperature

As mentioned earlier, the junction temperatures of emitters can have large variations at high operating currents. However, only a single value for the entire LD bar can be obtained from this setup. The following investigation is conducted to define the physical meaning of the measured value.

The emitters are connected in parallel, and thus the electrical resistance of the LD bar can be expressed as:

$$R_{\mathrm{bar}}(T) = \frac{1}{\sum_{i=1}^{N} {}^{1}\!/\!{}_{R_i(T_i)}} \tag{2}$$

where R_{bar} is the electrical resistance of the bar [Ω]; R_i and T_i are the electrical resistance [Ω] and the temperature of the i^{th} emitter [°C], respectively.

Let's consider a case where the junction temperature of the LD bar increases linearly from the edge to the center ($\Delta T = T_{center} - T_{edge}$). This simple linear variation is analyzed to illustrate the physical meaning of the measured value. The average junction temperature of this case can be expressed as

$$T_j^{ave} = \frac{1}{N}\sum_{i=1}^{N} T_i$$

Then, the true forward voltage and the forward voltage estimated based on the average temperature can be expressed as:

$$V_f^{true}(T) = R_{bar}(T) \cdot I_{prob} \;\; ; \;\; V_f^{ave}(T) = \frac{1}{N} R(T_j^{ave}) \cdot I_{prob} \tag{3}$$

V_f^{true} is the true forward voltage of the LD bar [V]; V_f^{ave} and $\frac{1}{N} R(T_j^{ave})$ are the forward voltage [V] and the electrical resistances [Ω] of the LD bar at the average junction temperature, respectively. It is to be noted that the true forward voltage and the forward voltage based on the average temperature are different because the emitters are connected in parallel.

The difference between these two values provides an estimate about how the true junction temperature deviates from the average junction temperature of the bar by dividing slope of the calibration curve [V/K]. The deviation can be defined as:

$$\delta T_j = \frac{V_f^{true} - V_f^{ave}}{1.21 \cdot 10^{-3}} \tag{4}$$

where δTj is deviation of the true junction temperature from the average junction temperature of LD bar [°C]; $1.21 \cdot 10^{-3}$ is the slope of the calibration curve [V/K].

Figure 39 shows the deviation as a function of ΔT. The deviation is less 1°C even for ΔT of 100°C. The small change in resistance with the temperature (Figure 37) is attributed to this behavior. The results imply that the junction temperature determined from the forward voltage of the LD bar at the operating current can be considered as the average junction temperature of the LD bar in practice. This implication will be confirmed later with the actual non-linear temperature distribution of the LD bar.

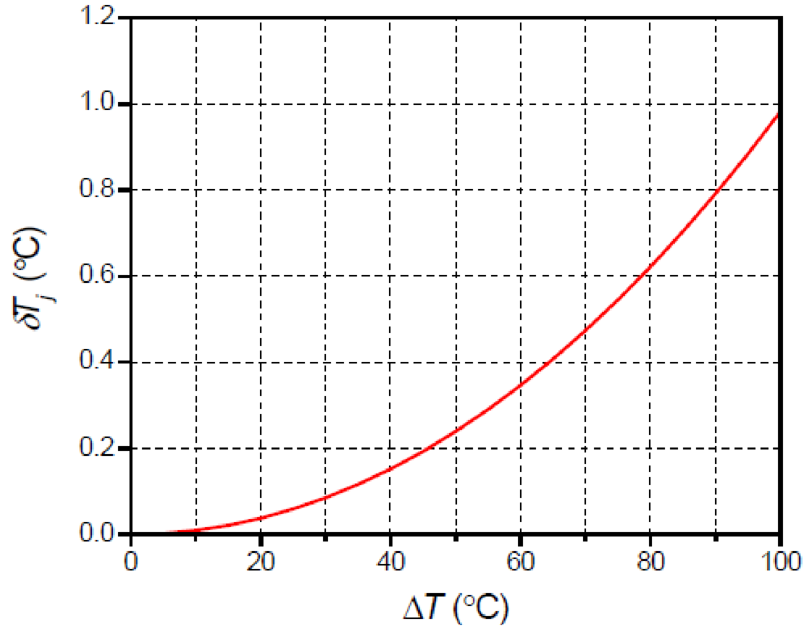

Figure 39: Deviation of the Measured Junction Temperature of LD Bar from the Average Junction Temperature of LD Bar with a Linearly Changing Temperature of ΔT from the Edge to the Center

3.2.3.3 Average Junction Temperature Measurement

Figure 40 shows the transient voltage behavior of the LD bar obtained after blocking the operating current of 80 A. An extreme voltage peak at the beginning of transient behavior is clearly visible. It was produced by an inductor voltage attributed to the large rate of current change (79.88 A to zero) and the non-zero inductance of the LD [25, 26]. The peak was large but disappeared quickly after 200 μs.

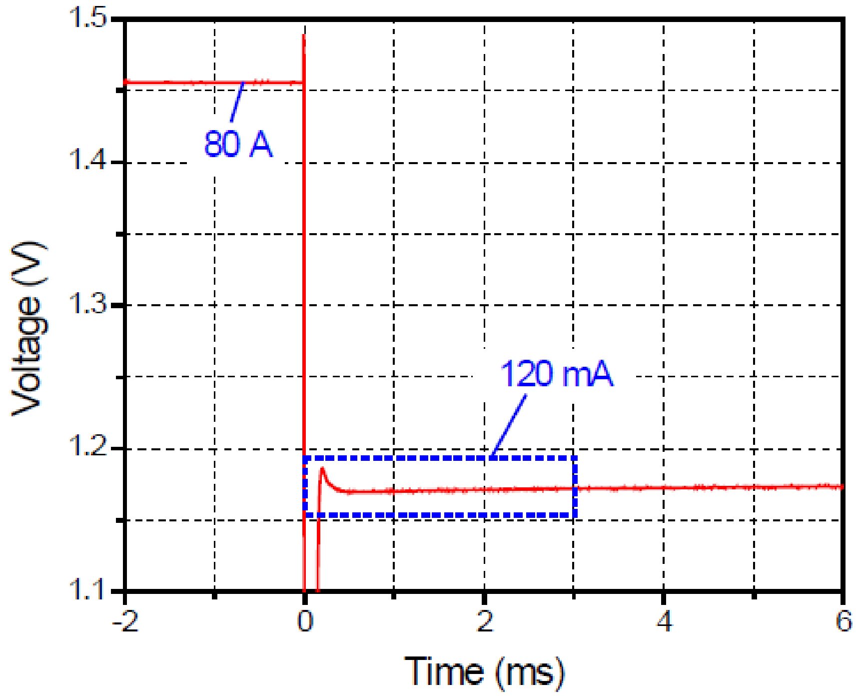

Figure 40: Transient Voltage Behavior of the LD Bar Obtained after Blocking the Operating Current of 80 A

Based on theoretical analysis [27-30], it is known that a junction temperature changes linearly in the square root of the time scale, if heat is dissipated in one direction through a homogenous material. In the case of this epi-down LD bar with the water-cooled microchannel cooler, the heat transfer through the GaAs substrate, and convection, as well as radiation, to the ambient surroundings is practically negligible (less than 1% of the total) due to the extremely large heat transfer coefficient in the water-cooled microchannel cooler (this will be discussed further in Section 3.2.4.2). Thus, the linear extrapolation in the square root time scale is applicable for the LD bar. The enlarged view of the region marked by a dashed box in Figure 41 is shown in Figure 41a. The voltage was converted into the temperature using the calibration curve and it was plotted in the square root time scale (Figure 41b).

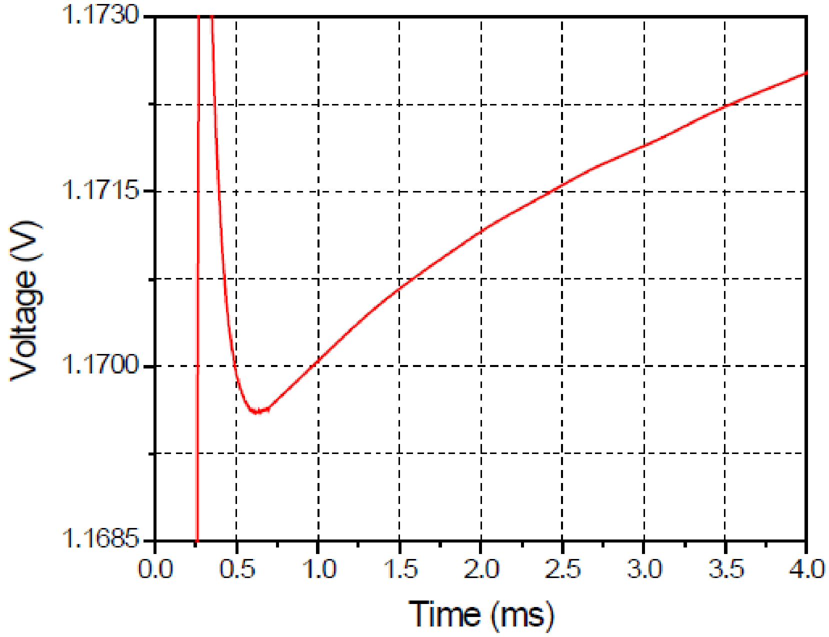

(a)

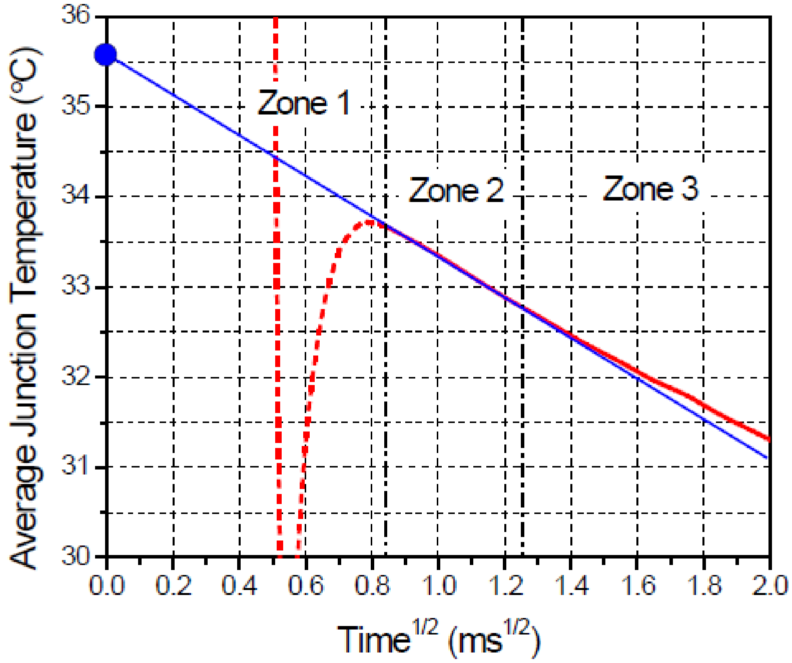

(b)

Figure 41: (a) Enlarged View of the Region Marked by a Dashed Box in Figure 6 and (b) Average Junction Temperature in the Square Root Time Scale

The linear extrapolation provides the estimated average junction temperature at the operating current.

The transient junction temperature behavior can be divided into three zones. Zone 1 is the region dominated by the electrical delay. Zone 2 is the region where the linear junction temperature variation follows the square root time scale. When the propagating thermal wave reaches the microcooler interface, the transient junction temperature behavior of the CuW submount vanishes and we enter Zone 3. It is estimated from Figure 7b that Zone 2 ends at t =1.57 ms (= 1.25 ms$^{1/2}$). The following analytical analysis was conducted to confirm Zone 2.

The transient domain governed by the CuW submount can be calculated analytically using a time constant, which can be expressed as [31, 32]:

$$\tau_{th} = \frac{\rho c_p d^2}{k} \tag{5}$$

where τ_{th} is the thermal time constant [s]; d is the thickness along the heat transfer direction [m]; k is the thermal conductivity [W/m·K]; cp is the specific heat [J/kg·K]; and ρ is the density [kg/m^3]. Material properties, thickness, and the calculated thermal time constant of CuW are listed in Table 2. A thermal time constant value for the CuW was determined as 1.37 ms, which is defined as the heating or cooling time required to produce a temperature change at the heat source (junction) equal to 63.2% of the total temperature difference between the initial and the final temperature. This value is reasonably close to the experimental observation, which confirms the validity of the experimental data.

Table 2. Material Properties, Thickness, and Calculated Time Constant used in the Analytical Solution [19, 20]

Material	Density (kg/m^3)	Specific heat (J/kg·K)	Conductivity (W/m·K)	Thickness (μm)	Time constant (ms)
CuW	17300	160	200	300	1.37

The average junction temperature at the operating current was estimated from the linear extrapolation shown in Figure 7b; the estimated average junction temperature at 80 A was 35.6°C. The discrepancy in the repeatability of the average junction temperature measurement was less than 0.1°C, which was attributed to the probe current source inaccuracy.

The average junction temperatures were measured from 10 A to 80 A at an interval of 10 A. The results are shown in Figure 42. The connected lines between the measured data represent the trend of the results. As expected, the junction temperature increased with the current, but the rate started to decrease around the threshold current (26 A), where the stimulated emission began to occur; i.e., the higher wall-plug efficiency lead to the reduction of the heat dissipation as well as the junction temperature. The heat dissipation as a function of the forward current will be discussed further in Section 3.2.4.1.

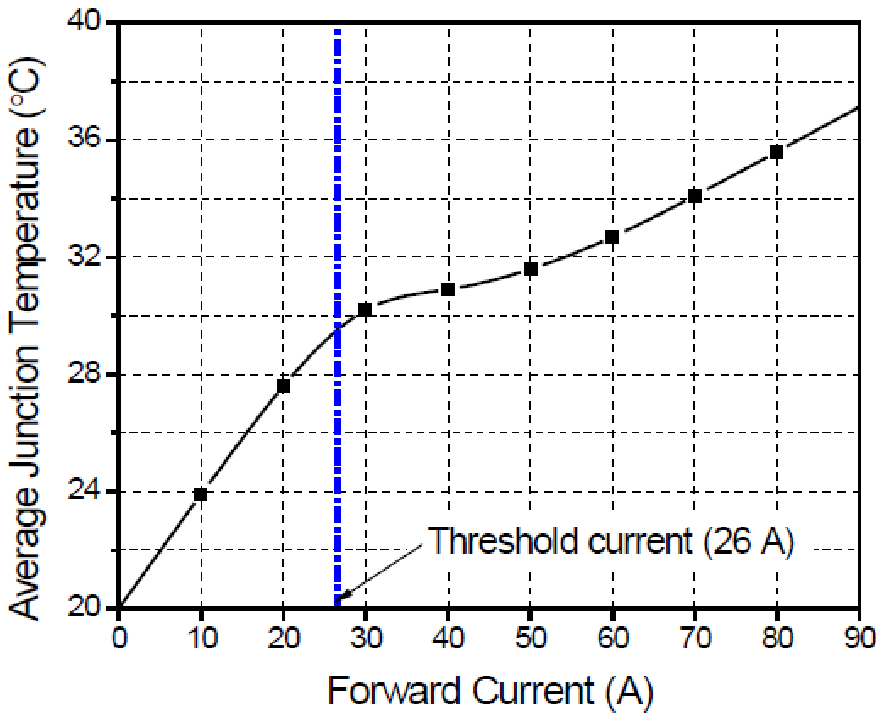

Figure 42: Average Junction Temperature at different Forward Currents

3.2.4 Heat Dissipation and Microcooler Effective Heat Transfer Coefficient

The forward voltage and the emitted radiant flux are measured to quantify the amount of heat dissipation, using the following relationship [33]:

$$P_h(T_j) = I_f \cdot V_f(T_j) - \Phi(T_j) \tag{6}$$

where P_h is the heat dissipation [W]; I_f is the forward current [A]; V_f is the forward voltage [V]; and Φ is the radiant flux [W]. After measuring the heat dissipation in Section 5.1, the effective heat transfer coefficient of the water-cooled microchannel is calculated inversely from the numerical simulation, using the measured average junction temperature and the heat dissipation in the next section.

3.2.4.1 Measurement of Heat Dissipation

The DAQ1 measured the forward voltage of the LD bar and the optical power sensor measured the optical power (the radiant flux) continuously. When the optical power and the forward voltage of the LD reached the steady state condition, the values of forward voltage and optical power were recorded, from which the heat dissipation was calculated using Equation (6).

The forward voltages, electrical input power (product of the forward voltage and the forward current), optical powers, and heat dissipations were measured as a function of current with an interval of 10 A. The results are shown in Figure 43. The forward voltage and the electrical input power increased with the current. The optical power was virtually negligible before the threshold current (26 A) and increased linearly with the operating current after the threshold current. Similar to the junction temperature, the heat dissipation increased with the current and the rate started to decrease around the threshold current.

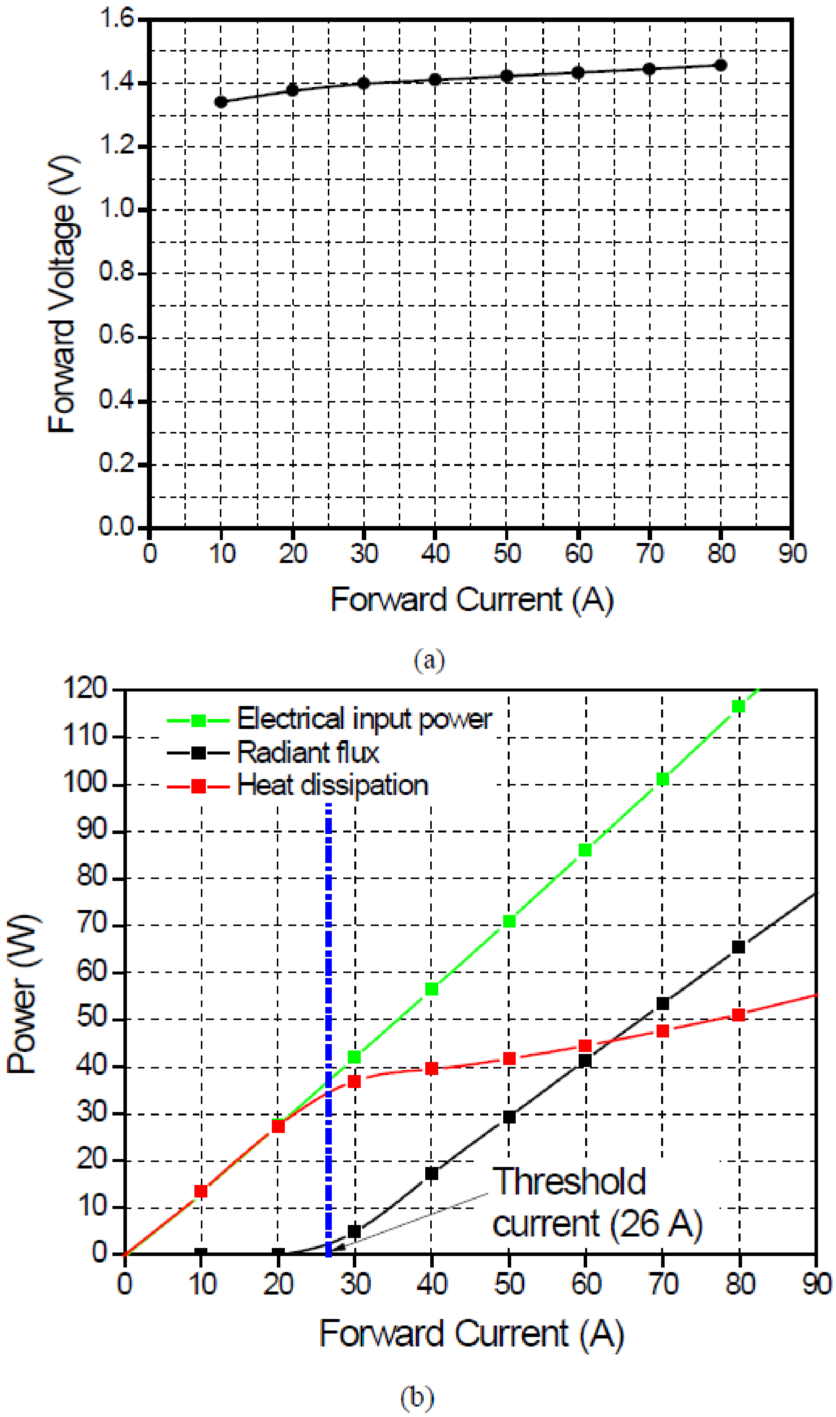

Figure 43: (a) Forward Voltage and (b) Electrical Input Power, Radiant Flux, and Heat Dissipation as a Function of Forward Current

The thermal resistances can be estimated by dividing the temperature difference between the average junction temperature (T_{jave}) and the inlet water temperature (T_{inlet} = 20°C) by the heat dissipation. The average junction temperatures, the heat dissipations, and the calculated thermal resistances (R_{th}) are summarized in Table 3. The results showed a consistent thermal resistance of 0.295 K/W ±0.015 K/W for all measured currents. The measurement uncertainty of the heat dissipation was mainly caused by the accuracy of the optical power sensor.

Table 3. Average Junction Temperature and Thermal Resistance Estimations at different Forward Currents at 20°C of the Inlet Water Temperature

I_f [A]	10	20	30	40	50	60	70	80
P_h [W]	13.4 ± 0.3	27.4 ± 0.4	37.0 ± 0.7	39.2 ± 1.2	41.7 ± 1.6	44.5 ± 2.2	47.7 ± 2.7	51.1 ± 3.1
T_j^{ave} [°C]	23.8	27.6	30.2	30.9	31.6	32.7	34.1	35.6
T_j^{ave} - T_{inlet} [°C]	3.8	7.6	10.2	10.9	11.6	12.7	14.1	15.6
R_{th} [K/W]	0.28 ± 0.01	0.28 ± 0.01	0.28 ± 0.01	0.28 ± 0.01	0.28 ± 0.01	0.29 ± 0.01	0.30 ± 0.02	0.31 ± 0.02

3.2.4.2 Effective Heat Transfer Coefficient

The numerical model (ANSYS 16.1) used in the current analysis is shown in Figure 44. The model has the same geometry as the LD bar (23 emitters; emitter width of 200 μm and the fill-factor of 50%, i.e., the pitch of 400 μm). A metallization layer (Ti/Pt/Au) layer between the emitter and the AuSn solder was not considered in the model due to the ignorable thermal resistance. The values of thermal conductivity of GaAs, CuW submount, and AuSn solder used in the analysis are 54 W/m·K [34], 200 W/m·K [19, 20], and 58 W/m·K [35], respectively.

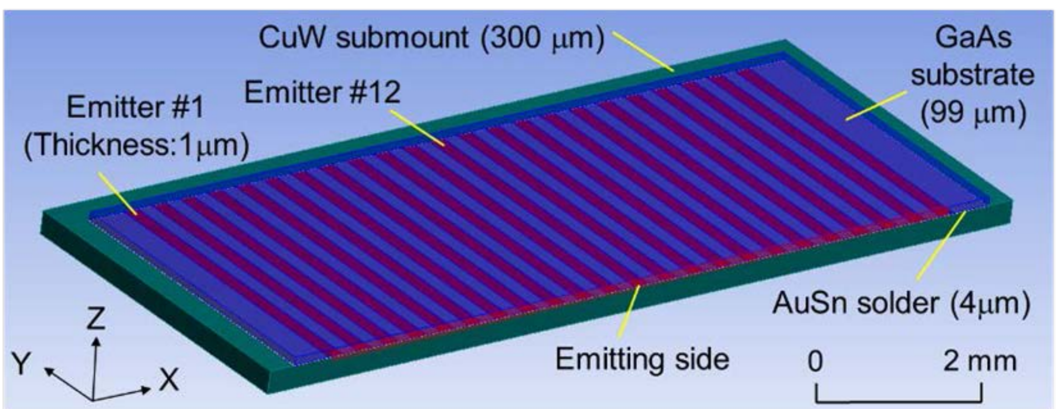

Figure 44: 3D Model

The ambient temperature was set at 20°C (the same as the inlet water temperature). The effective heat transfer coefficient of the water-cooled microchannel cooler was assumed to be uniform on the bottom of the CuW submount. The effective heat transfer coefficients for natural convection (5 W/m^2·K) and radiation (GaAs emissivity of 0.62 [36]) were set on the top and the sides of the model, albeit with the expectation of negligible effects on the junction temperature.

It is important to note that Equation (6) is applicable only when the junction temperature is uniform. In addition, the uniform heat dissipation would be desired to determine the effective heat transfer coefficient most accurately. Thus, the lowest operating current (10 A) was used to calculate the effective heat transfer coefficient.

The heat dissipation obtained in section 3.2.4.1 was applied uniformly on the emitters, and then, the effective heat transfer coefficient was adjusted until the difference between the measured average junction temperature and the numerically calculated average junction temperature reached its minimum value. The average junction temperature difference, after typically 5 iterations, was less than 0.1°C, and the resulting effective heat transfer coefficient was found to equal 98 kW/m^2K.

The junction temperature distribution at 20 A was also calculated to validate the effective heat dissipation. The difference between the average junction temperatures (experimental and numerical) was less than 0.1°C, which confirmed the validity of the effective heat dissipation.

3.2.5 Numerical Prediction of Junction Temperature Distribution

It is important to understand the effect of the junction temperature on the heat dissipation before performing numerical analyses at high operating currents because Equation (6) is applicable only when the junction temperature is uniform. The heat dissipation at 80 A was measured with three inlet water temperatures (10, 15, and 20°C). The junction temperature at each inlet temperature was also measured, and the results are summarized in Table 4.

Table 4. Heat Dissipation at 80A under different Inlet Water Temperatures

T_{inlet} [°C]	10	15	20
T_j^{ave} [°C]	25.6	29.2	35.6
V_f [V]	1.458	1.457	1.456
$I_f \cdot V_f$ [W]	116.66	116.58	116.46
Φ [W]	67.80	66.85	65.34
P_h [W]	48.9	49.7	51.1

As the average junction temperature increased from 25.6 to 35.6°C, the forward voltage as well as the radiant flux decreased. The forward voltage reduction reduced the total electrical power consumption, while the radiant flux reduction increased the fraction of the input power converted to heat. It is worth noting that the net heat dissipation increased only by 2.2 W (or 4%) corresponding to the junction temperature increase of only 0.6°C, as the two parameters compensated their effects on heat dissipation [37]. The results indicate that the junction temperature dependency on the heat generation, over a range of 10°C, is not significant, which provides a technical rationale for the following numerical study.

3.2.5.1 Temperature Distribution in LD Bar

The heat dissipation and effective heat transfer coefficient obtained in the previous section were used to predict the junction temperature distribution over the LD bar numerically under high operating currents. The junction temperature distribution of the LD bar at 80 A is shown in

Figure 45a. The GaAs substrate was not shown in order to clearly show the temperature distribution of the emitters.

The highest temperature occurred at the emitting side of the center emitter and the lowest temperature was observed at the opposite side of the edge emitter. The junction temperature decrease toward the edge emitter and the back end was attributed to the effect of the hear spreader. Because the edge emitter and the back end had cooling area enhancement from the CuW submount, the more heat could be dissipated due to the extra heat spreading. The maximum temperature difference was 10.1°C. This result confirms that the application of uniform heat dissipation across all the emitters in a multi-emitter LD bar can be expected to provide acceptable numerical results for input current of up to 80 A.

The junction temperature distribution was also calculated at the operating current of 160 A. Since the test apparatus was only capable of providing 125 A, an additional power supply (N5744A: Keysight Technologies) was connected to the operating current source in parallel to provide the additional current of 35 A. The forward voltage and the optical power at 160 A were 1.544 V and 162.4 W, respectively, and the heat dissipation was 84.7 W (65.7% of the wall-plug efficiency). It is to be noted that the average junction temperature could not be measured at 160 A because the threshold current of the MOSFET switch was around 90 A.

The junction temperature distribution of the LD bar at 160 A is shown in Figure 45b. The highest and lowest temperatures are 47.9°C and 31.7°C; the junction temperature difference is 16.2°C.

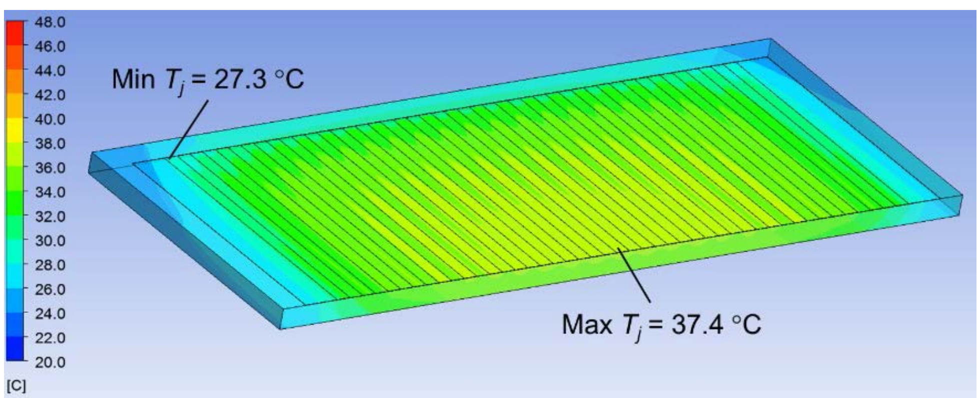

(a)

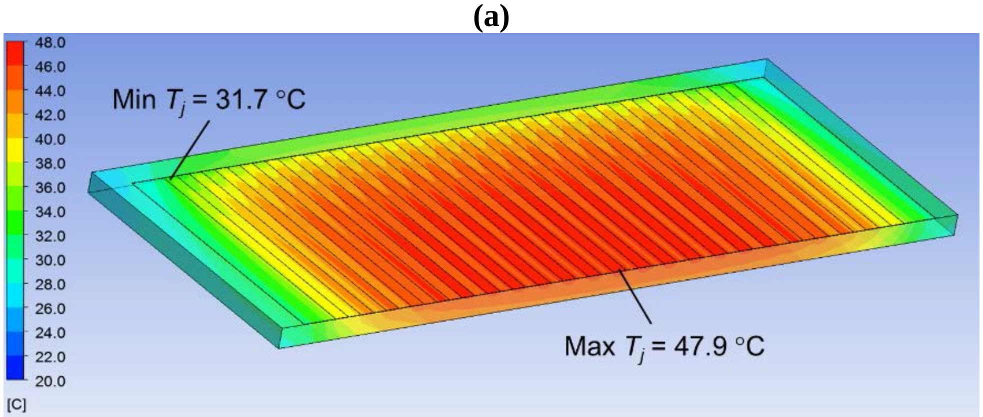

(b)

Figure 45: Temperature Distribution of the LD Bar at (a) 80 A and (b) 160 A

The average junction temperature of each emitter is compared in Figure 46, where the only left half is shown due to the symmetry. The average junction temperatures remain virtually unchanged over the center half of emitters (from #12 to #7) and then rapidly drops toward the edge emitter. The maximum average junction temperature differences among the 12 emitters are 4.9°C and 7.8°C at 80 A and 160 A, respectively.

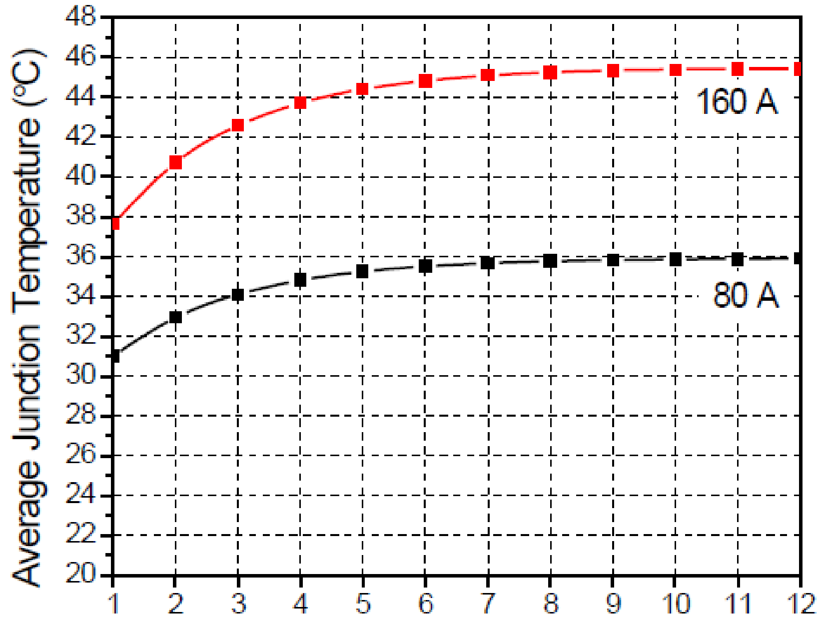

Figure 46: Average Junction Temperature of each Emitter in Left Half (symmetry)

The front-to-back junction temperature variations within the center (#12) and the edge (#1) emitter are plotted in Figure 47. The junction temperature decreases exponentially from the emitting side to the back end. The junction temperature variations within the emitter are largest at the center emitter, and the magnitude increases as the operating current increases. The junction temperature variations of the center emitter are 5.4°C and 8.7°C for 80 A and 160 A, respectively.

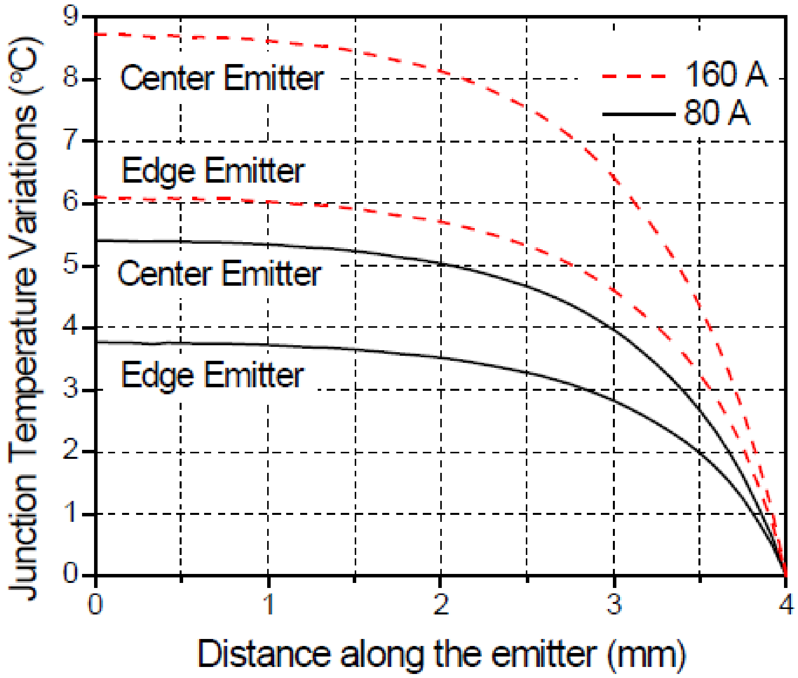

Figure 47: Junction Temperature Variations along the Emitter

The deviations of the true junction temperature from the average junction temperature of the bar were calculated with the actual non-linear temperature distribution of the LD bar. Based Equation 3 was first used to determine the true forward voltage and the forward voltage from the average junction temperature:

$V_f^{true}(80) = 1.168239$ V and $V_f^{ave}(80) = 1.168242$ V ; and

$V_f^{true}(160) = 1.157465$ V and $V_f^{ave}(160) = 1.157472$ V .

The deviations were then calculated from Equation 4; they were 0.002°C and 0.006°C for 80 A and 160 A, respectively. As expected from the small change in resistance with the temperature, the deviations were negligible. The results confirmed the validity of the proposed method.

3.2.5.2 Wall-plug Efficiency and Spectral Power Distribution

The junction temperature change affects the wall-plug efficiency, which is defined as the optical output power divided by the electrical input power. Each emitter of the LD bar tested in the study produced an optical power of ≈7.06 W at the operating current of 6.95 A (the LD bar with 23 emitters at the operating current of 160 A).

It was reported in Ref. [38] that for a single emitter (a center wavelength of 975 nm) producing 6 W at 6A, the wall-plug efficiency increased by only 3% from 275 K (71%) to 260 K (74%). Thus, it is reasonable to assume that each emitter of the LD bar tested in the study has similar behavior to that of the single emitter reported in Ref. [38], and consequently, the effect of the junction temperature distribution on the wall-plug efficiency is not significant.

The power spectrum of the LD bar was obtained by a spectrometer (AvaSpec-ULS3648- USB2: Avantes) combined with a cosine corrector (CC-UV/VIS/NIR-5.0: Avantes). The diameter of the corrector was larger than the LD bar to ensure that the spectrometer received light from all 23 emitters equally. The output obtained from the measurement system was the irradiance (W/m^2) of the LD bar as a function of wavelength. The power spectrum was obtained by normalizing the irradiance distribution by the peak irradiance. The results obtained at 30, 60, and 120 A are shown in Figure 48.

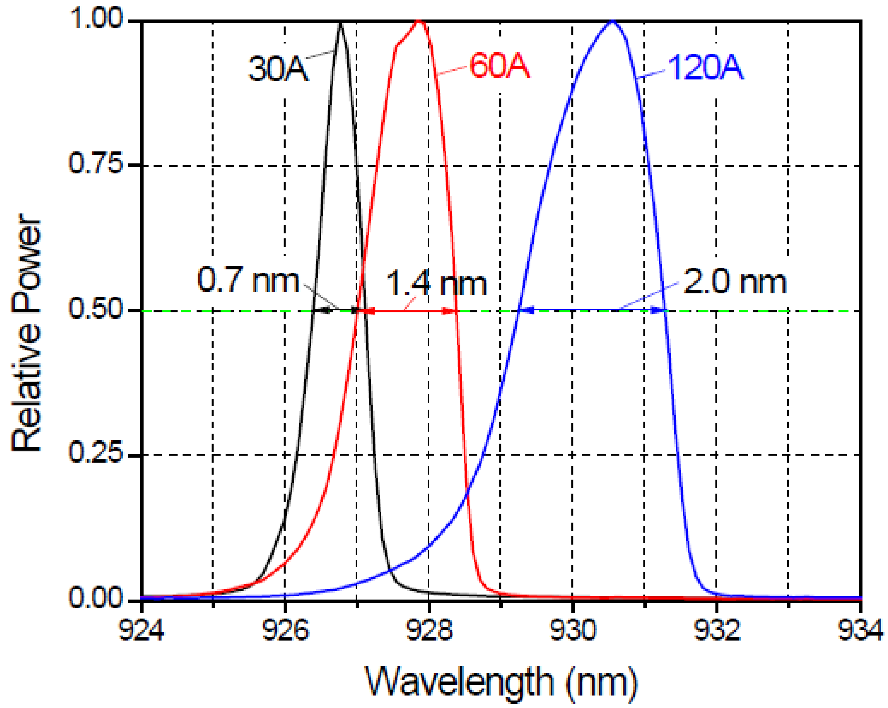

Figure 48: Normalized Power Spectrum at 30, 60, and 160 A

LDs are known to show the spectral red shift (i.e., higher peak wavelength) at higher junction temperatures due to the reduced band gap energy [39]. The spectral red shift caused by the junction temperature has been reported to be 0.28 nm/K [40] and 0.32 nm/K [41] for 808 nm and 980 nm LDs, respectively. The results in Figure 14 show the red shift of ≈0.3 nm/K, which is consistent with the reported values.

The results also show that the spectrum is broadened as the current increases; i.e., the larger full width at half maximum (FWHM) at the higher forward current. The asymmetry of the spectrum (i.e., more broadening toward the lower wavelength) become more severe as the current increases. Both broadening and asymmetry are attributed to the larger junction temperature gradient at the high currents.

The analysis was based on a very large heat transfer coefficient. In practice, various thermal solutions can be employed for cooling the LD bar. In terms of the coefficient of performance (COP), the lower heat transfer coefficients (i.e., the decreased flow rate) can reduce the operating costs. However, the junction temperature will rise and the temperature variation within the LD bar will also increase with lower heat transfer coefficients. This will increase the asymmetry of the SPD and the peak wavelength shift, which can reduce the pumping efficiency [42].

A high heat transfer coefficient is desired to increase the pumping efficiency, which can be achieved with an extreme flow rate of a coolant. However, the higher flow rate reduces the COP, which increases the operating cost. In addition, it can accelerate the erosion process of the surface structures inside microchannels, which will increase the junction temperature and will eventually reduce the lifetime of the LD bar [43, 44]. Consequently, optimization of thermal solutions for high power LD bars should be sought while considering the operating cost as well as various thermal, mechanical, and optical aspects of the system.

3.2.6 Summary

A hybrid experimental and numerical method was proposed and implemented for predicting the junction temperature distribution of a high power LD bar. A commercial water-cooled LD bar was utilized to illustrate and validate the proposed method. The average junction temperature and the heat dissipation were measured, and the effective heat transfer coefficient of the cooling system was determined inversely using numerical simulation. The characterized properties were used to predict the junction temperature distributions of the LD bar at the extreme operating currents. The results showed significant junction temperature variations not only among emitters (7.8°C) but also along each emitter (8.7°C) at 160A, which increased the asymmetry of the power spectrum. The proposed method can be used to determine the proper operation condition of the LD bar as well as to evaluate designs during packaging platform development. The future work will address a methodology to define the optimum design of LD bars considering the COP, performance, and reliability.

3.3 Spectral Power Distribution Deconvolution Scheme for High-Power LD Bar

3.3.5 Introduction

A typical LD array of 10 mm length contains 10 ~ 60 emitters with fill factors from 10% to 90%. The lateral heat spreading in an LD array causes the thermal crosstalk effect between emitters, and thus, the junction temperature distribution typically has a large variation [51]. In addition, hotter emitters in an LD array take a larger share of the total array current, and emit more optical power. The effect is known as “current competition”, which causes the non-uniform power distribution [45, 46]. Consequently, the SPDs of individual emitters would have significant variations.

The SPDs of an LD array with non-uniform temperature and power distributions are illustrated in Figure 49, where SPD^{Array}, SPD^{1} and SPD^{4} represent the SPDs of the LD array, the edge emitter and the center emitter, respectively. The junction temperature of the center emitter is always higher compared to the edge emitter. As a result, the SPD of the center emitter (SPD^{4}) would have the maximum power and the longest wavelength, while the SPD of the edge emitter (SPD^{1}) the lowest power and the shortest wavelength.

The SPD of an LD array can be readily measured by a spectrometer connected with a cosine corrector. The SPDs of individual emitters can also be measured by placing a beam baffle in front of the array. In practice, however, the distance between the beam baffle and the LD array has to be extremely small because of the small pitch between adjacent emitters and the large beam divergence of the LD array. The optical feedback from the beam baffle at such a close distance can cause degradation or even catastrophic optical mirror damage of the emitters [9,10]. In addition, translating the baffle accurately to open only one emitter while keeping the baffle at the close proximity of the array is very challenging in practice, especially for LD arrays with high fill factors (≥50%).

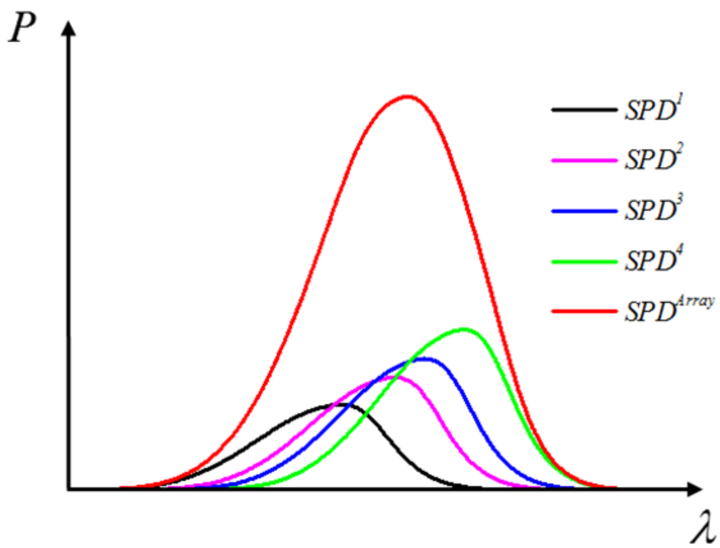

Figure 49: Illustration of SPDs for an LD Array with a Non-Uniform Temperature and Power Distributions

Where SPD^{Array}, SPD^1, and SPD^4 represent the SPDs of an LD array, the edge emitter and the center emitter, respectively

The objective of this paper is to propose a novel method to predict the SPDs of individual emitters by deconvoluting the SPD of an LD array. The proposed method takes into account the thermal cross talk effect as well as the current competition effect. A complete analytical description of the proposed method is described in Section 3. The implementation of the proposed method using a commercial LD array is presented in Section 4. Applications of the SPD deconvolution are presented in Section 5.

3.3.2 Analytical Model for Deconvolution

The SPD of an LD array, $SPD^{ARRAY}(\lambda)$, is simply the sum of the SPDs of single emitters, and can be expressed as:

$$SPD^{Array}(\lambda) = \sum_{i=1}^{N} SPD^{i}(\lambda) \tag{7}$$

where $SPD^i(\lambda)$, is the SPD of the i^{th} emitter; and N is the number of emitters.

Figure 50 illustrates schematically the SPD of a single-emitter in an LD array. The maximum power and the full FWHM of the i^{th} emitter are denoted as P^i_{max} and W^i, and λ_c^i is the central wavelength of the i^{th} emitter, which is defined as the wavelength satisfying the condition that $\Delta\lambda_L$ is equal to $\Delta\lambda_R$ at $P^i_{\max}/2$.

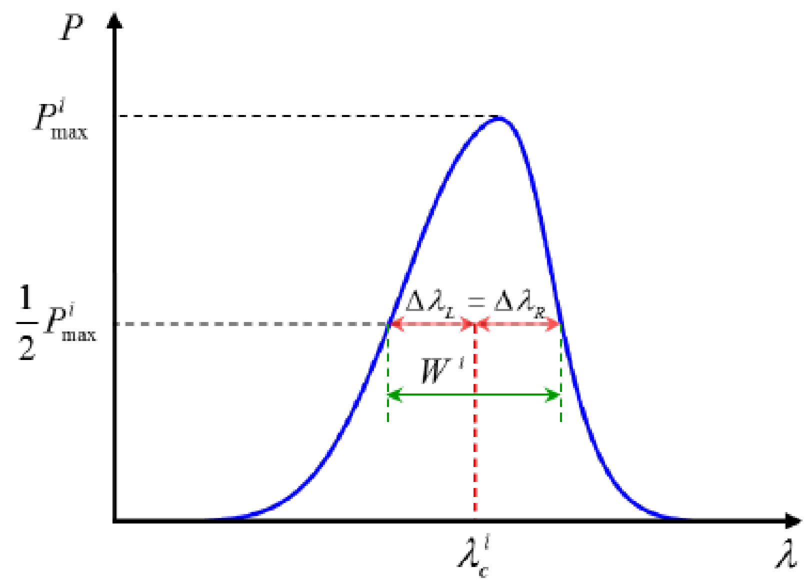

Figure 50: Schematic Illustration of the SPD of a Single-Emitter in an LD Array

In a typical LD array, an emitter located at the center of an LD array (referred to as "center emitter") has the highest junction temperature. Its normalized SPD can be defined as:

$$\overline{SPD}^{center}(\lambda) = \frac{SPD^{center}(\lambda)}{P^{center}_{\max}} \tag{8}$$

where $\overline{SPD}^{center}(\lambda)$ is the SPD of the center emitter normalized by the maximum power of the center emitter spectrum, $P^{center}_{\max}$.

The SPD of the center emitter is asymmetric because the profile of the gain spectrum is not symmetric [47]. The asymmetric SPD can be expressed using multiple Gaussian functions:[48, 49]

$$\overline{SPD}^{center}(\lambda) = \sum_{j=1}^{k} A_j \exp\left[-\left(\frac{\lambda - \Lambda_j}{w_j}\right)^2\right] \tag{9}$$

where k is the number of Gaussian functions; Aj is the normalized amplitude of the j^{th} Gaussian function; Λ_j is the central wavelength of the j^{th} Gaussian function; and w_j is proportional to the FWHM (W_j) of the j^{th} Gaussian function, which is defined as:

$$w_j = \frac{W_j}{2\sqrt{\ln 2}} \tag{10}$$

The junction temperature of each emitter varies within an LD array. It has been known that the central wavelength of the SPD changes linearly with the temperature.[47] As the junction temperature increases, the band-gap energy decreases, and the refractive index and cavity length increase. The band-gap energy reduction is the dominant factor causing the central wavelength shift. The relationship between the central wavelength shift and the junction temperature, then, can be expressed as:

$$\Delta\lambda = \lambda_c^i - \lambda_c^{center} = a\left(T^i - T^{center}\right) \tag{11}$$

where λ_c^i and λ_c^{center} are the central wavelengths of the i^{th} emitter and the center emitter T^i and T^{center} are the junction temperature of the i^{th} emitter and the center emitter; and a is the temperature coefficient of wavelength that can be determined experimentally.

As described in Refs. [45, 46], the maximum power of each emitter changes with temperature by the effect known as “current competition”. The emitters that turn on earlier take a larger share of the total array current, and emit more power because hotter emitters in an LD array have a reduced bandgap energy, and thus a lower threshold current.

Based on the theoretical and experimental results by S. Bull et al. [45, 46], the effect of current competition can be approximated described by an exponential function. The maximum powers of the i^{th} emitter and the center emitter, then, can be expressed as:

$$P_{\max}^i = C\left(e^{T^i/B} - 1\right) \tag{12}$$

$$P_{\max}^{center} = C\left(e^{T^{center}/B} - 1\right) \tag{13}$$

where B and C are constants. By combining Equations (12) and (13), the maximum power of the i^{th} emitter normalized by $P_{\max}^{center}$ can be described as:

$$\frac{P_{\max}^{i}}{P_{\max}^{center}} = \frac{\left(e^{T^{i}/B} - 1\right)}{\left(e^{T^{center}/B} - 1\right)} \tag{14}$$

The constant, *B*, will be referred to as the current competition constant that can be determined experimentally.

It was reported that the shape of the normalized gain spectrum profile remains virtually the same regardless of junction temperatures [50]. This implies that the FWHM of the normalized single emitter SPD will not be altered by the junction temperature variations with an LD array. Using Equations (9) and (11), the SPD of the i^{th} emitter, then, can be expressed as:

$$\begin{aligned} SPD^{i}(\lambda) &= P_{\max}^{i} \cdot \overline{SPD}^{center}(\lambda - \Delta\lambda) = \\ & P_{\max}^{i} \cdot \sum_{j=1}^{k} A_j \exp\left[-\left(\frac{\left(\lambda - a\left(T^{i} - T^{center}\right)\right) - \Lambda_j}{w_j}\right)^2\right] \end{aligned} \tag{15}$$

Using Equation (15), Equation (16) can be written as:

$$\begin{aligned} SPD^{i}(\lambda) &= P_{\max}^{center} \cdot \frac{\left(e^{T^{i}/B} - 1\right)}{\left(e^{T^{center}/B} - 1\right)} \cdot \\ & \sum_{j=1}^{k} A_j \exp\left[-\left(\frac{\left(\lambda - a\left(T^{i} - T^{center}\right)\right) - \Lambda_j}{w_j}\right)^2\right] \end{aligned} \tag{16}$$

3.3.3 Implementation

In order to predict the SPDs of individual emitters of an LD array using Equitation (16), four key parameters have to be determined experimentally: (1) the normalized SPD of the center emitter, (2) the temperature coefficient of wavelength, *a*, (3) the current competition constant, *B*, and (4) the maximum power of the center emitter, $P_{\max}^{center}$. The junction temperature distribution of the array is critically required to determine the four parameters. The hybrid experimental/numerical method proposed previously by the authors [51] is employed to determine the required junction temperature distribution. Detailed procedures to determine the four parameters are presented in sections 3.3.3.3 to 3.3.3.6, respectively, after describing the testing apparatus and the hybrid method for the junction temperature measurement in sections 3.3.3.1 and 3.3.3.2.

3.3.3.1 Device and Measurement Apparatus

A commercial 930 nm LD array (E11.4N-940.10-150C-SO13.1: DILAS) used in the study consists of 23 identical emitters. The width of each emitter is 200 μm and the pitch between adjacent emitters is 400 μm (a fill-factor of 50%). The maximum optical power at 160 A is 160 W. The LD chip is epi-down bonded on a CuW submount using AuSn die attach. The CuW submount (CTE): 6.5 ppm/°C) is placed between the GaAs chip (6.4 ppm/°C) and the copper microchannel heat sink (16.6 ppm/°C) to reduce the mismatch in the CTE [18, 52].

A test apparatus to measure the SPD of the central emitter is illustrated in Figure 51. The power supply (LDX-36125-12: ILX Lightwave) applies the operating current with a nominal accuracy of ±0.1%. The spectrometer (AvaSpec-3648) connected with a cosine corrector measures the spectrum. The wavelength range of the spectrometer is from 200 nm to 1100 nm, and the resolution is 0.025 nm. The chiller (ISOTEMP I 115V/60HZ PD-1: Fisher Scientific) regulates the inlet water temperature with a temperature stability of ±0.1°C. The flow meter (FLDW3211G: OMEGA Engineering) controls the flow rate from 0 to 500 mL/min.

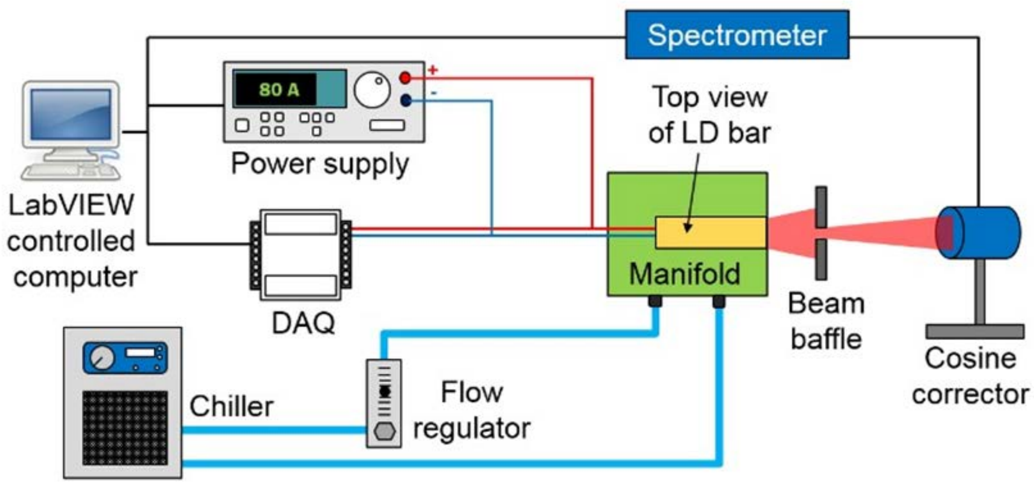

Figure 51: Schematic Illustration of the SPD of a Single-Emitter in an LD Array

When only the SPD of the center emitter is to be measured, the beam baffle is placed between the LD array and the cosine corrector. The baffle is made of graphite to minimize the optical feedback while dissipating the heat generated by the light beam effectively.

In order to measure the absolute optical power, the cosine corrector and the spectrometer are replaced to the optical power sensor (USB-PM-150-50: Coherent Laser Group). The power supply, the DAQ (USB-6212: National Instruments), and the optical power sensor are integrated into a LABVIEW program.

3.3.3.2 Determination of Junction Temperature Distribution

The hybrid experimental/numerical method [51] was developed to determine the junction temperature distribution within a high power LD array. With the method, the forward voltage method is first implemented in a unique experimental setup to measure the average junction temperatures of the LD array. After measuring the heat dissipation of the LD array, the effective heat transfer coefficients of the cooling system at different flow rates are determined inversely from the numerical simulation using the measured average junction temperature and the heat dissipation. The characterized effective heat transfer coefficients at different flow rates are used to predict the junction temperature distribution over the LD array at different inlet water temperatures. More details about the method can be found in the reference [51].

The numerical model (ANSYS Icepak 17.2) used in the analysis is shown in Figure 52. The values of thermal conductivity of GaAs, CuW submount, and AuSn solder are 54 W/m·K, 209 W/m·K, and 58 W/m·K, respectively [53-57]. The ambient temperature was set to be 20°C. The effective heat transfer coefficients for natural convection (5 W/(m^2·K)) and radiation (GaAs emissivity of 0.62) were set on the top and the sides of the model, although they had negligible effects on the junction temperature [58]. The effective heat transfer coefficient of the water-cooled microchannel was assumed uniform on the bottom of the CuW submount.

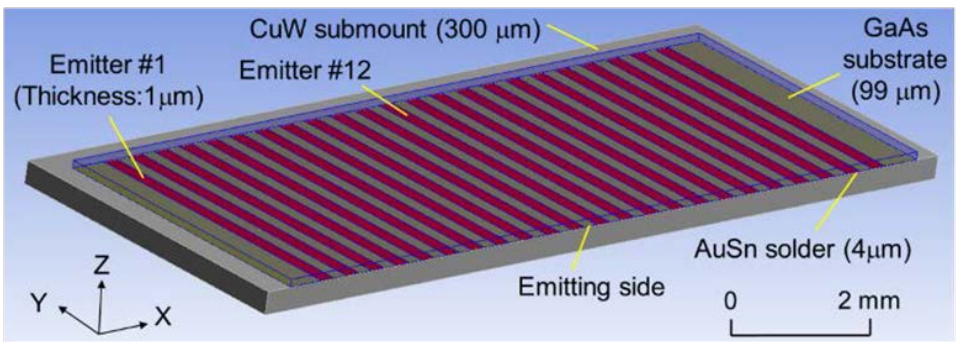

Figure 52: Schematic Illustration of the SPD of a Single-Emitter in an LD Array

The generated heat from the active region of the LD was applied uniformly on the emitters in the LD array, and the effective heat transfer coefficient was calculated using the iterative method. The forward voltage, optical power, heat dissipation, average junction temperatures, and calculated effective heat transfer coefficients at different flow rates (100, 200, 300, 400, and, 500 mL/min) are summarized in Table 5. Using the effective heat transfer coefficients and heat dissipation, the temperature distributions of the LD array at different flow rates were predicted. A representative steady-state temperature distribution of the LD array is shown in Figure 53, where I_f = 80 A, h = 80,500 W/(m^2·K), and T_{inlet} = 20°C. The maximum temperature occurred at the front facet of the center emitter. The junction temperature decreased towards the edge emitter and the rear facet due to the heat spreading effect of the CuW submount.

Table 5. Effective Heat Transfer Coefficients at different Flow Rates with an Inlet Water Temperature of 20°C

Flow rate [mL/min]	100	200	300	400	500
Forward voltage [V]	1.4135	1.4147	1.4154	1.4156	1.4160
Optical power [W]	14.675	16.215	16.707	16.986	17.153
Heat dissipation [W]	42.034	40.542	40.079	39.808	39.657
Average junction temperature [°C]	39.3	34.9	31.5	31.0	30.0
Effective heat transfer coefficient [kW/(m^2·K)]	56.25	80.50	112.65	119.90	137.60

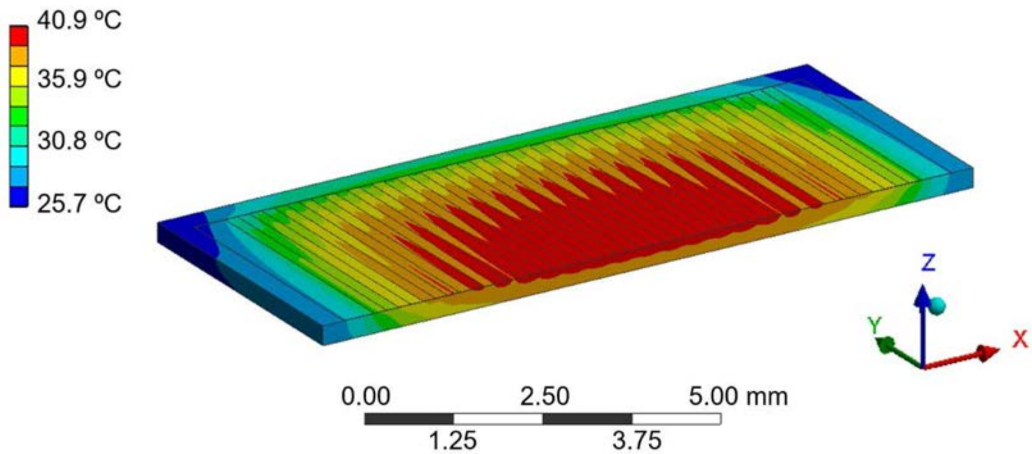

Figure 53: Temperature Distribution of the LD Array
(I_f = 80 A, h = 80,500 W/(m^2·K), and T_{inlet} = 20°C)

The simulated average junction temperature of each emitter at different heat transfer coefficients is shown in Figure 54, where the left half of the LD array is shown due to the symmetry of the LD array. The junction temperatures remain nearly unchanged in the center of the LD array, but rapidly decrease towards the edge emitters. As expected, the temperature variation between the center emitter and the edge emitter increases with the low heat transfer coefficient.

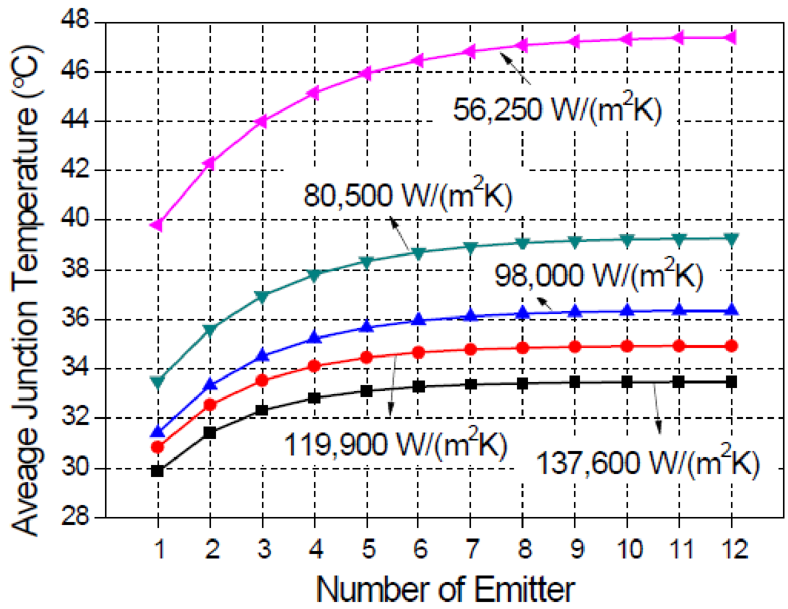

Figure 54: Average Junction Temperature of each Emitter in the Left Half (symmetry) under various Heat Transfer Coefficients

(I_f = 80 A, and T_{inlet} = 20 ℃).

3.3.3.3 Determination of Normalized SPD of Center Emitter

Considering the beam divergence along slow axis (10°) and the high fill factor (50%) of the commercial LD array, the beam baffle width and the distance between the beam baffle and the LD array should be smaller than 0.36 mm and 0.90 mm, respectively (Figure 55), which poses implementation difficulties. In order to cope with the problem, a larger baffle width of 1.5 mm was used in the actual experiments, which averaged three emitters in the middle of the array. The larger baffle width was rationalized by the fact that that a few emitters in the middle of the array were known to have a virtually identical junction temperature.[51] Two supplementary experiments were conducted to confirm the rationale.

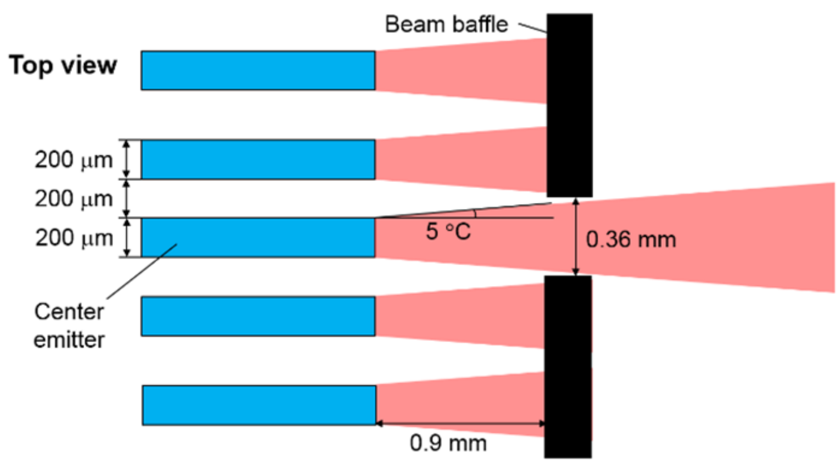

Figure 55: Illustration of the Size and Location of an Optical Baffle to Measure the SPD of a Center Emitter

In the first experiment, two baffle widths of 1.5 and 3 mm were used to record three and seven emitters in the middle, respectively. The normalized SPDs under the forward current (I_f) of 80 A, the flow rate (f) of 500 mL/min, and the inlet water temperature (T_{inlet}) of 20°C are compared in Figure 56(a). The normalized SPDs are nearly identical, which clearly indicates that even seven emitters in the center have the virtually same SPDs considering the measurement uncertainty. Accordingly, it is reasonable to conclude that the SPD obtained from three center emitters represents the normalized SPD of a single emitter.

In the second experiment, the baffle width was fixed to be 1.5 mm and the normalized SPDs of three center emitters were measured at different cooling conditions. The normalized SPD of three center emitters at two conditions are compared in Figure 56(b): flow rates and inlet water temperatures of (1) 300 mL/min and 10°C and (2) 500 mL/min and 20°C. The FWHMs of the SPDs under the above cooling conditions were determined from the SPDs. Both SPDs have the identical FWHM of 1.3 nm, which indicates that the spectrum width of the center emitters remains unchanged regardless of temperatures. The result confirms the fact [50] that the shape of the normalized gain spectrum profile is not altered by the junction temperature variation within an LD array, and thus, provides a technical rationale for Equation (15); i.e., the normalized SPD of each emitter in an LD array can be determined from the normalized SPD of the center emitter.

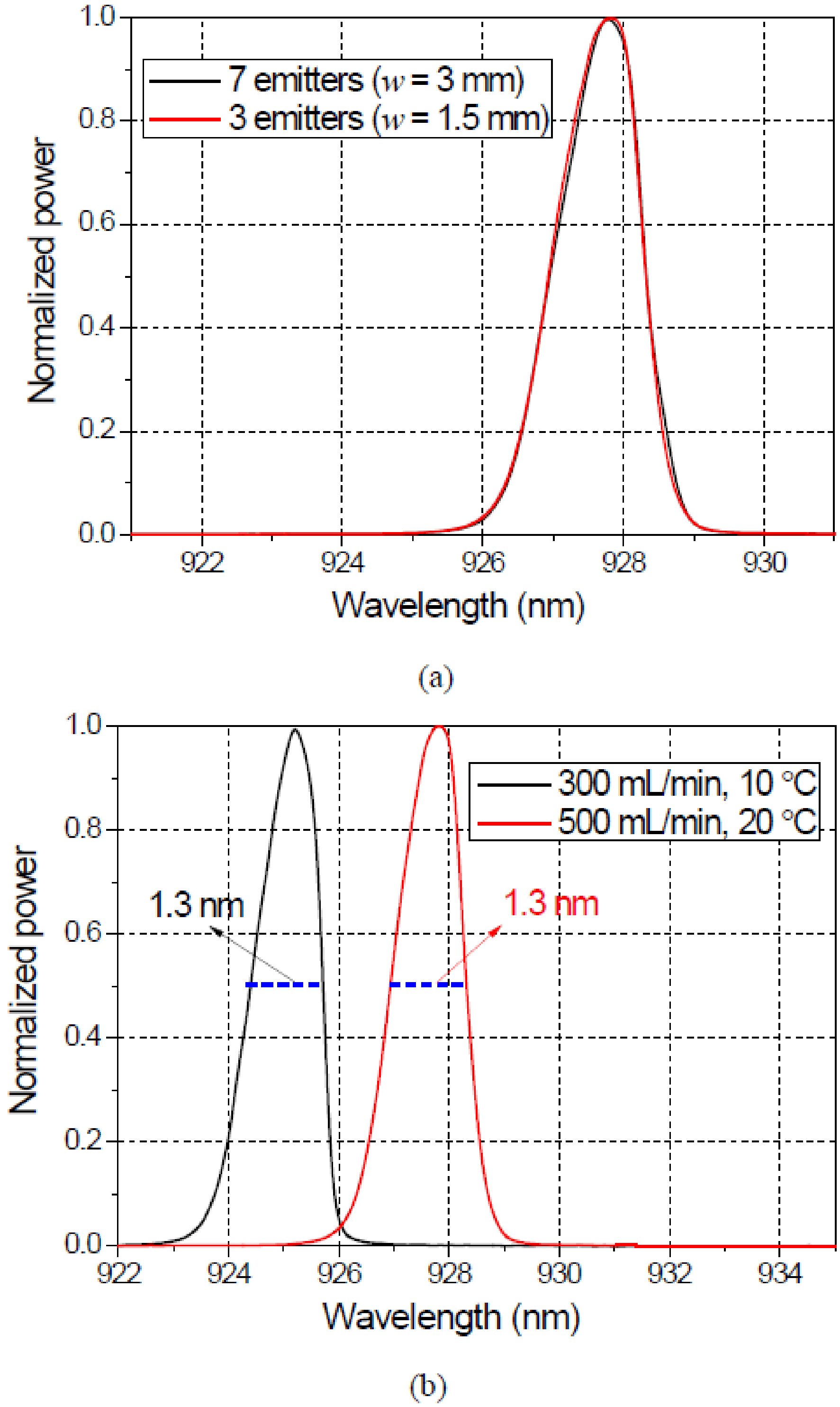

Figure 56: Normalized SPDs obtained from (a) Three and Seven Emitters in the Middle of an LD Array where the Baffle Widths are 1.5 and 3 mm, respectively (I_f = 80 A, f = 500 mL/min, and T_{inlet} = 20 °C) and (b) Three Emitters in the Middle of an LD Array at different Flow Rates and Inlet Water Temperatures

As mentioned earlier, the SPD of the center emitter is not symmetric, and multiple Gaussian functions are necessary to deconvolute the normalized SPD of the center emitter.[48] Three Gaussian functions were used to fit the normalized SPD of the center emitter in this study. The results are shown in Figure 57, where the measured SPD is compared with the Gaussian fitting. Perfect agreement is evident; the R2 value is close to 1. The Gaussian fitting parameters are shown in Table 6.

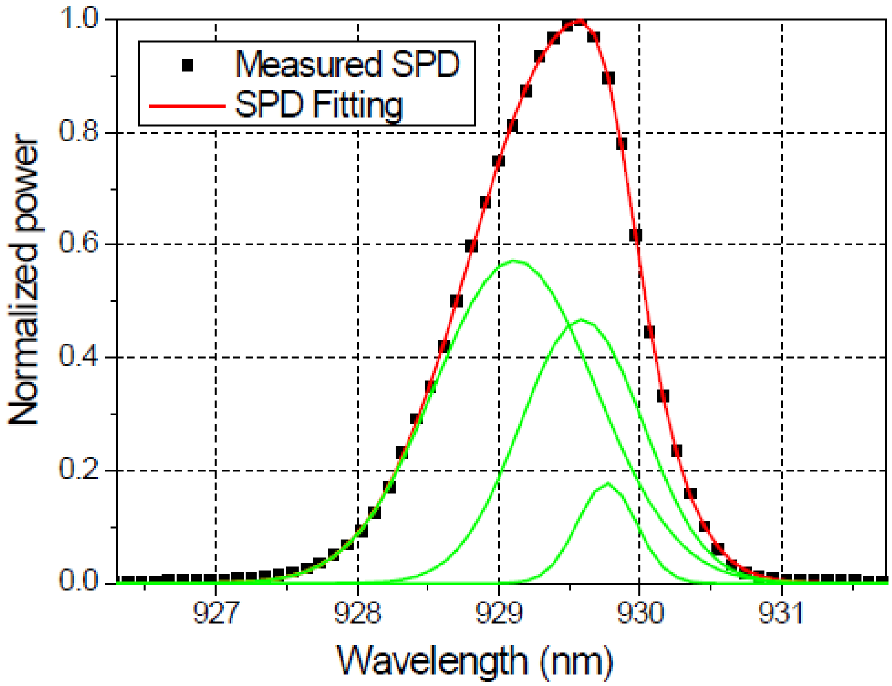

Figure 57: SPD Deconvolution of the Normalized SPD of the Center Emitter using Three Gaussian Functions

(I_f = 80A, f = 200 mL/min, and T_{inlet} = 20 ℃)

Table 6. Three Gaussian Functions used to define the Normalized SPD of the Center Emitter

Λ_1 (nm)	Λ_2 (nm)	Λ_3 (nm)
928.588	929.114	929.765
w_1 (nm)	w_2 (nm)	w_3 (nm)
0.613	0.810	0.293
A_1	A_2	A_3
0.468	0.573	0.177

3.3.3.4 Temperature Coefficient of Wavelength

The SPDs of three center emitters were measured at various junction temperatures to determine the temperature coefficient of wavelength, a. The normalized SPDs and the corresponding average junction temperatures of the center emitter are shown in Figure 58(a), from which the central wavelengths can be obtained.

The central wavelengths of center emitter are plotted as a function of average junction temperature in Figure 58(b); a linear relationship is evident. The temperature coefficient of wavelength was obtained from Figure 58(b) using Equation (11); it was 0.3 nm/K. The spectral redshift caused by the junction temperature has been reported as 0.26-0.28 nm/K [59-61], and 0.32 nm/K [62], for the LDs with the central wavelength of 808 nm and 980 nm, respectively. The measured value is consistent with the reported values.

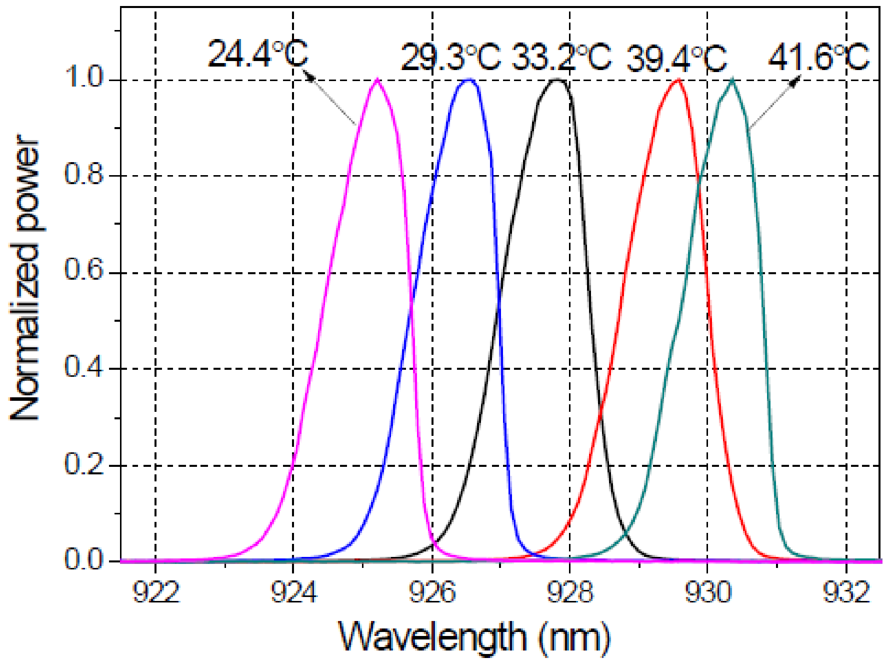

(a)

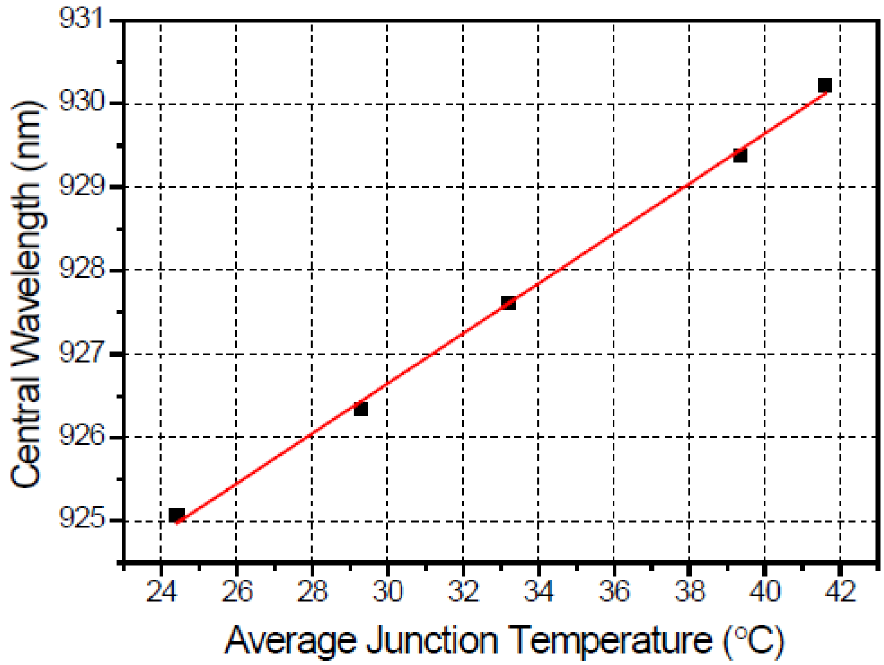

(b)

Figure 58: (a) Measured normalized SPDs representing the Center Emitter at different Average Junction Temperatures and (b) Central Wavelengths of SPDs plotted as a Function of the Average Junction Temperature of the Center Emitters; the Linear Relationship defines the Temperature Coefficient of Wavelength

3.3.3.5 Determination of Current Competition Constant

The current competition constant, *B*, cannot be determined deterministically as Equation (14) contains two unknowns. The value was determined iteratively. An initial value of *B* = 3.6 was first estimated by fitting the data in Ref. [46] through Equation (14). Then, the normalized SPD of each emitter, based on the normalized SPD of the center emitter (assuming $P_{max}^{center} = 1$), was calculated using Equation (16), and subsequently the normalized SPD of the LD array was calculated using Equation (7). Finally, a non-linear regression was performed while adjusting the values of *B* until the coefficient of determination, R^2, between the simulated result and the measured normalized SPD of the LD array reached its maximum.

The normalized SPD of the LD array at a heat transfer coefficient of 98,000 W/(m^2·K) (the operating condition recommended by the LD array manufacturer) with an inlet water temperature of 20°C was measured to determine *B*. The results from the iteration process are shown in Figure 59. The simulated SPDs of each emitter obtained from the initial value of *B* = 3.6 is shown in Figure 59(a). The predicted SPDs of the LD array with the initial and final values (*B* = 3.6 and 5.9) are compared with the measured normalized SPDs in Figure 59(b) and (c), respectively. With the correct value of *B*, the predicted SPD became virtually identical to the measured SPD.

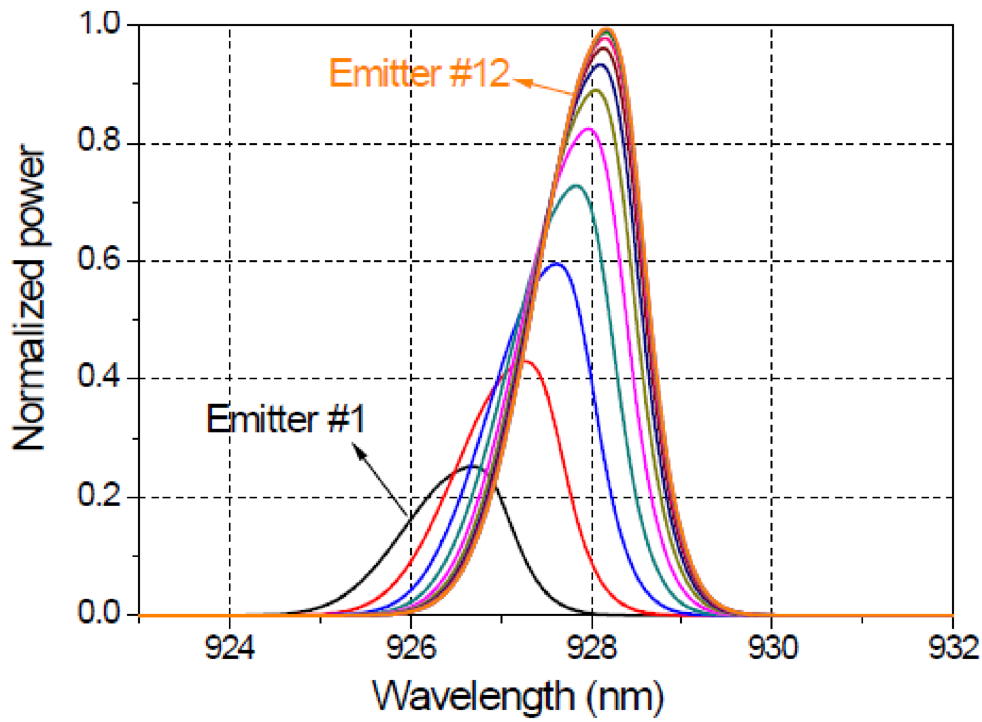

(a)

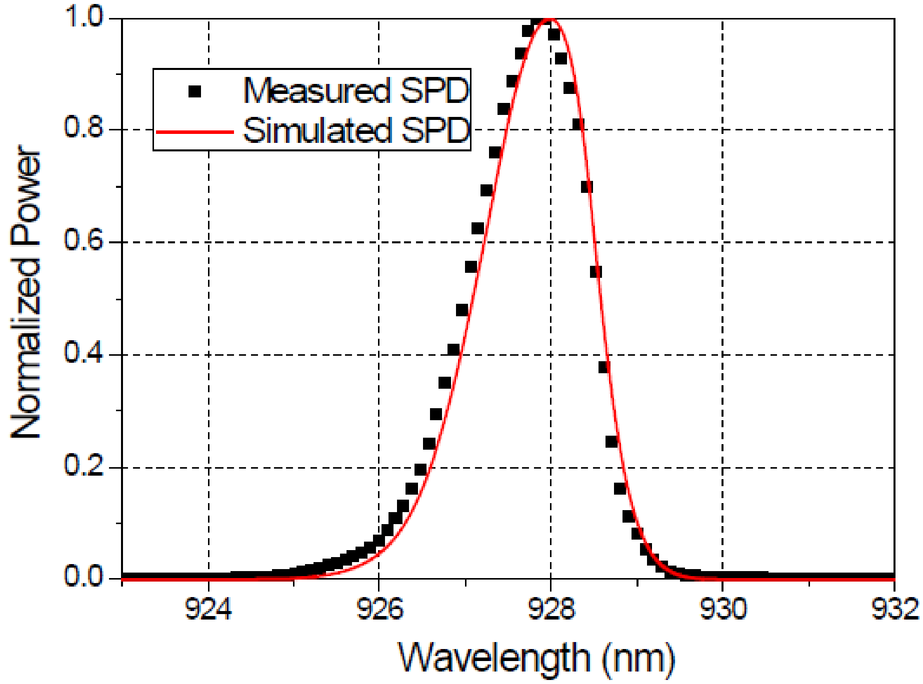

(b)

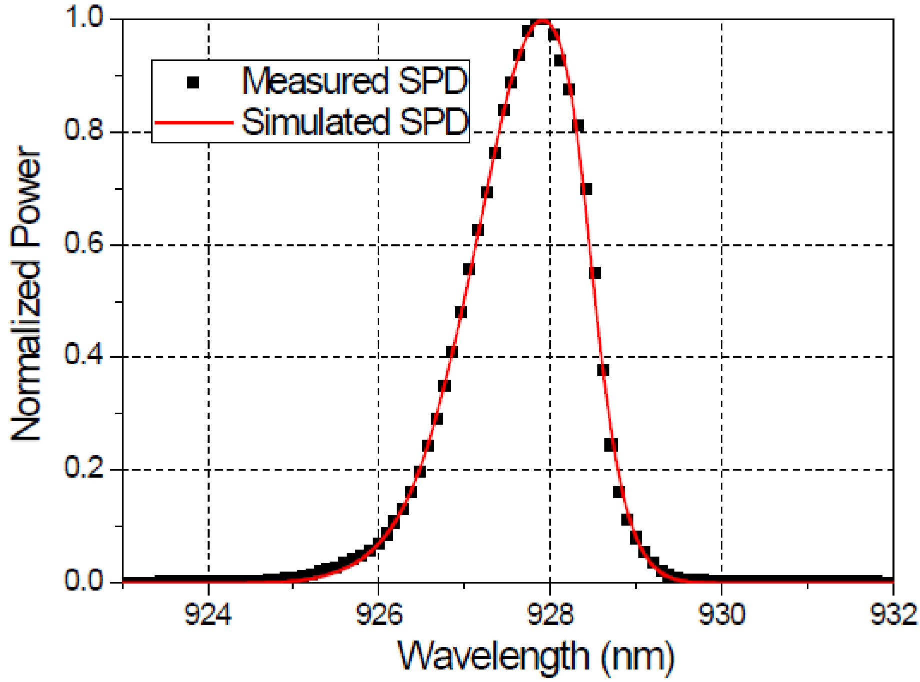

(c)

Figure 59: Predicted (a) Normalized SPDs of Emitters in the Left Half (symmetry), (b) Normalized SPD of the LD Array using an Initial Value of *B* = 3.6, and (c) Normalized SPD of LD Array using the Final Value of *B* = 5.9

(I_f = 80 A, h = 98,000 W/(m^2·K), and T_{inlet} = 20℃)

3.3.3.6 Determination of Maximum Power of Center Emitter

From Equations (1) and (10), the SPD of the LD array can be expressed as:

$$SPD^{Array}(\lambda) = \sum_{i=1}^{N} SPD^{i}(\lambda) =$$

$$P_{center}^{\max} \sum_{i=1}^{N} \left\{ \frac{\left(e^{T^i/B}-1\right)}{\left(e^{T^{center}/B}-1\right)} \cdot \sum_{j=1}^{k} A_j \exp\left[-\left(\frac{\lambda - a\left(T^i - T^{center}\right) - \Lambda_j}{w_j} \right)^2 \right] \right\} \tag{17}$$

The integration of $SPD^{Array}(\lambda)$ should be equal to the total optical power of the LD array. Therefore, the maximum power of the center emitter $P_{\max}^{center}$, can be expressed as:

$$P_{\max}^{center} = \frac{P_A}{\int_{\lambda=0}^{\infty} \sum_{i=1}^{N} \left\{ \frac{\left(e^{T^i/B}-1\right)}{\left(e^{T^{center}/B}-1\right)} \cdot \sum_{j=1}^{k} A_j \exp\left[-\left(\frac{\lambda - a\left(T^i - T^{center}\right) - \Lambda_j}{w_j} \right)^2 \right] \right\} d\lambda} \tag{18}$$

where P_A is the total optical power of an LD array, which can be measured experimentally.

Using the measured optical power of the LD array, the values of $P_{\max}^{center}$ under various cooling conditions were calculated using Equation (18). The results are summarized in Table 7. The value of $P_{\max}^{center}$ decreases with the increased flow rate, which is attributed to more uniform temperature distributions at higher flow rates. On the other hand, the value of $P_{\max}^{center}$ increases with the decreased inlet water temperature due to the higher optical power at lower junction temperatures.

Table 7. $P_{\max}^{center}$ under different Cooling Conditions

Flow rate [mL/min]	500	300	100	500	300	100	500	300	100
Inlet water temperature [°C]	20	20	20	15	15	15	10	10	10
$P_{\max}^{center}$ [W]	2.21	2.24	2.40	2.27	2.29	2.45	2.30	2.33	2.47

3.3.3.7 Prediction of the Absolute SPDs

Using the parameters determined in the previous sections, the absolute SPDs of all emitters were calculated using Equation (16). The results obtained at h = 137,600 W/(m^2·K) and T_{inlet} = 20°C are shown in Figure 60(a). The seven center emitters (#9, #10, #11 #12, #13, #14, #15) have a similar SPD (i.e., the maximum amplitude, the central wavelength, and the spectrum width), as expected from the experimental results reported in Section 3C. The SPD of the edge emitter has a lower amplitude and a shorter wavelength compared with the center emitter. The amplitude of SPD decreased rapidly towards edge emitter, which is attributed to the current competition effect. The current competition effect on individual emitters will be discussed further in the next section.

The SPD of the LD array at h = 137,600 W/(m^2·K) with T_{inlet} of 20°C was predicted using Equation (18). The result is compared with the measured SPD in Figure 60(b). The predicted SPD agrees well with the experimental data in both shape and magnitude. The result corroborates the validity of the proposed method.

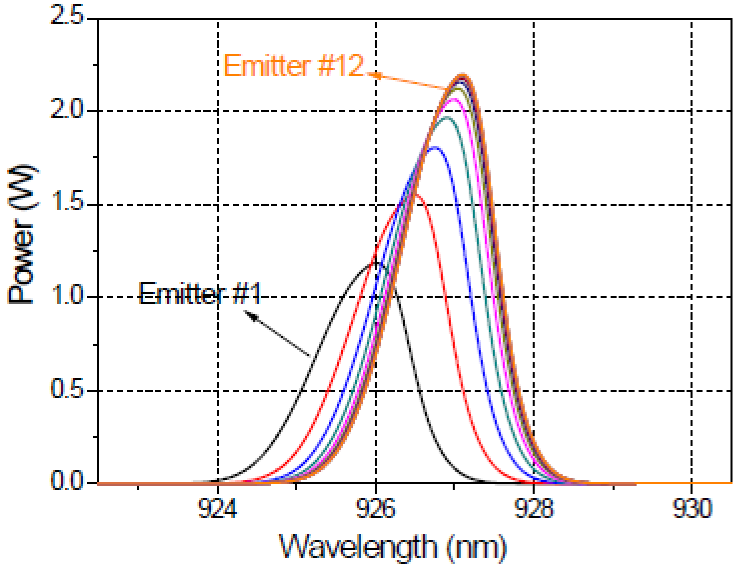

(a)

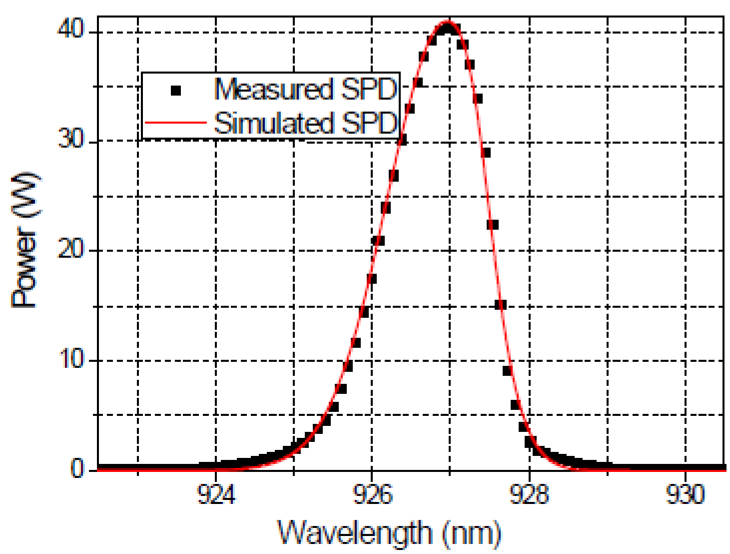

(b)

Figure 60: (a) Predicted Absolute SPDs of Individual Emitters in the Left Half (symmetry) and (b) Comparison between Predicted and Measured Absolute SPD of the LD Array
(I_f = 80 A, h = 137,600 W/(m_2·K), and T_{inlet} = 20℃)

3.3.4 SPDs of Single Emitters at Different Cooling Conditions: Results and Discussions

The SPDs of the LD array obtained at various cooling conditions are shown in Figure 61. They were measured at h_1 = 56,250, h_2 = 80,500, h_3 = 108,100, h_4 = 112,650, and h_5 = 137,600 W/(m^2·K); the corresponding flow rates were 100, 200, 300, 400, and 500 mL/min, respectively. The power reduction, the center wavelength redshift, and the increase in FWHM with smaller heat transfer coefficients are evident.

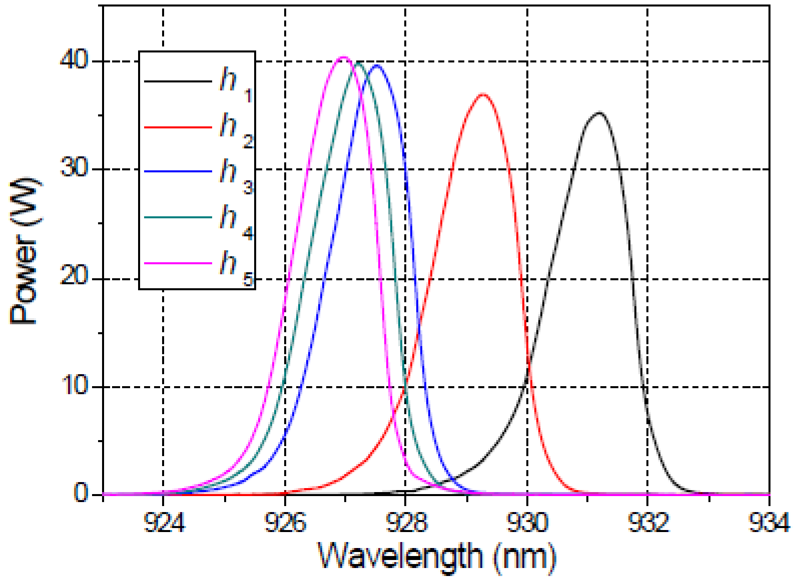

Figure 61: SPDs of the LD Array measured at Heat Transfer Coefficients
h_1 = 56,250 W/(m^2·K), h_2 = 80,500 W/(m^2·K), h_3 = 112,650 W/(m^2·K), h_4 = 119,900 W/(m^2·K), and h_5 = 137,600 W/(m^2·K) with I_f of 80 A and T_{inlet} of 20℃

The measured SPDs of the LD array were deconvoluted by the proposed method to investigate the effect of the heat transfer coefficients on the SPD of individual emitters. The results of four representative emitters (#1, #4, #8, and #12) are shown in Figure 62. It is worth noting that the maximum power of the edge emitter at h_1 was the lowest among all edge emitters, but the maximum power of the center emitter at h_1 became the highest of all center emitters. This is attributed to strong coupling between the junction temperature and power distributions.

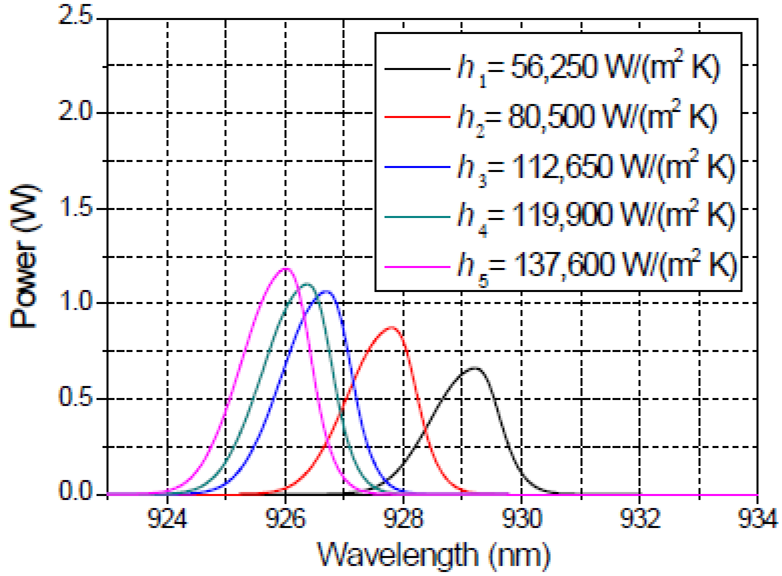

Power (W)
Wavelength (nm)
h_1= 56,250 W/(m^2 K)
h_2= 80,500 W/(m^2 K)
h_3= 112,650 W/(m^2 K)
h_4= 119,900 W/(m^2 K)
h_5= 137,600 W/(m^2 K)
2.5
2.0
1.5
1.0
0.5
0.0
924
926
928
930
932
934

(a)

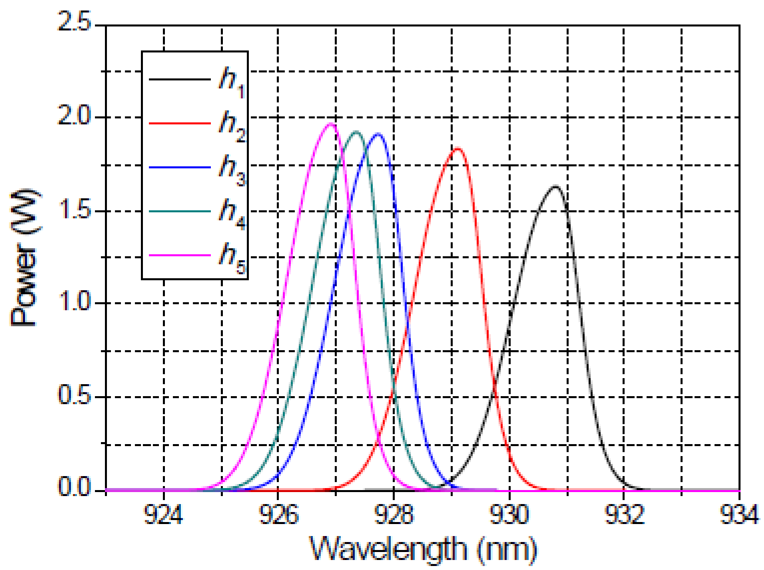

Power (W)
Wavelength (nm)
h_1
h_2
h_3
h_4
h_5
2.5
2.0
1.5
1.0
0.5
0.0
924
926
928
930
932
934

(b)

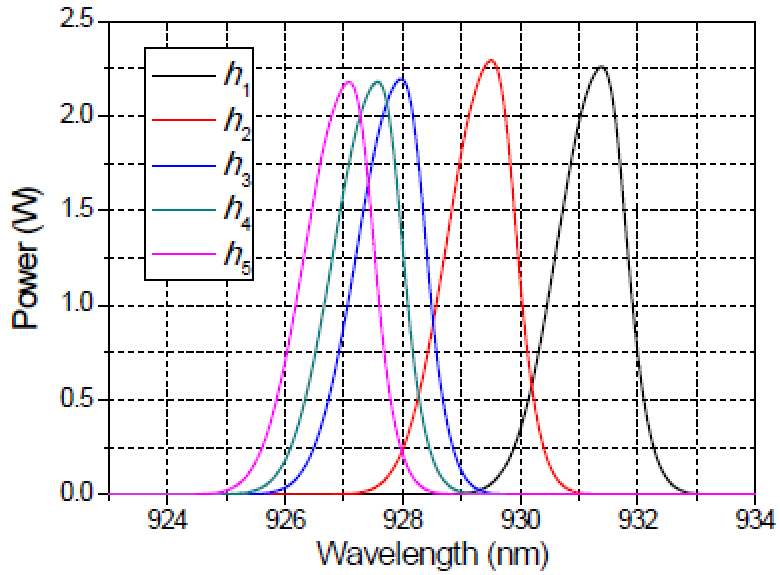

(c)

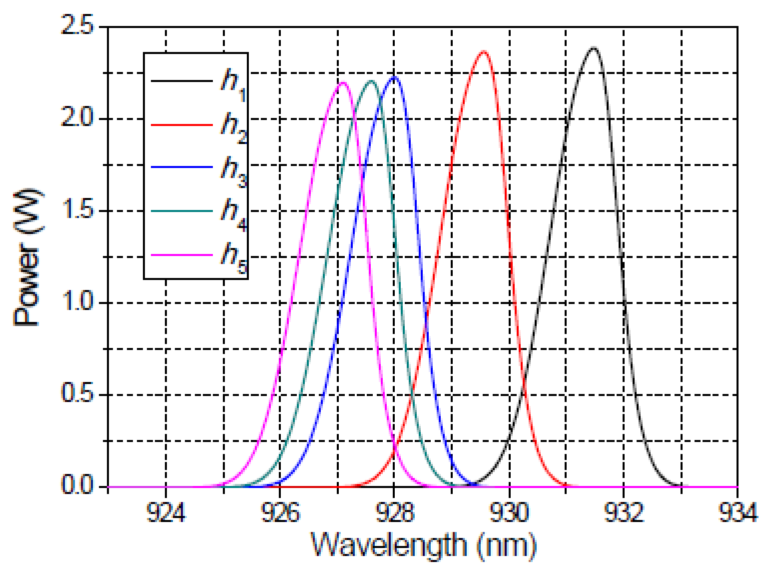

(d)

Figure 62: Predicted SPDs of Emitters #1, #4, #8, and #12 in the LD Array at h_1, h_2, h_3, h_4, and h_5

In order to put this into perspective, the maximum power of each emitter was calculated from Equation (14). The results are plotted for h_1 h_2 *and* h_5 in Figure 63 together with the junction temperatures predicted in Section 4. The current competition produces significant power variations in the LD array. The power of center emitters (from Emitter #8 to #12) is almost constant, but it decreases rapidly after Emitter #6.

At h_1 = 56,250 W/(m^2·K), the average junction temperatures of Emitter #1 and #12 are 47.4 and 39.8 °C, respectively, and the maximum power of Emitter #1 is about 28% of Emitter #12.

At h_5 = 137,600 W/(m^2·K), the average junction temperatures of Emitter #1 and #12 are 33.5 and 29.9°C, respectively, and the maximum power of Emitter #1 is about 54% of Emitter #12.

As mentioned earlier, the maximum power of Emitter #1 (edge emitter) at h_1 = 56,250 W/(m^2·K) is lower than that at h_5 = 137,600 W/(m^2·K). However, the maximum power of SPD at h_1 = 56,250 W/(m^2·K) increases much more quickly towards center emitters compared to the case of h_5 = 137,600 W/(m^2·K). As a result, the maximum power of Emitter #12 (center emitter) at h_1 = 56,250 W/(m^2·K) is higher than that at h_5 = 137,600 W/(m^2·K).

The results clearly show that the optical power ratio between center and edge emitters becomes larger as the heat transfer coefficient becomes smaller. It is known that the power efficiency reduction of each emitter caused by higher junction temperatures shown in Figure 63 is not significant.[61, 63, 64] Therefore, the larger ratio at the lower heat transfer coefficient (i.e., the larger temperature variations) is mainly attributed to the current competition. The larger power ratio between emitters are expected even at high heat transfer coefficients when operating currents much higher than 80 A are used.

The proposed method is applicable to LD arrays with higher fill factors (up to 90%) if the SPD of center emitters is determined. This method can also be employed to deconvolute the SPD of the LD array at different operating currents. It is important to recall that the SPD profile of the center emitter are altered by the operating currents since the gain spectrum changes with the carrier density [47]. The normalized SPD of the center emitter must be determined at a given operating current for successful deconvolution.

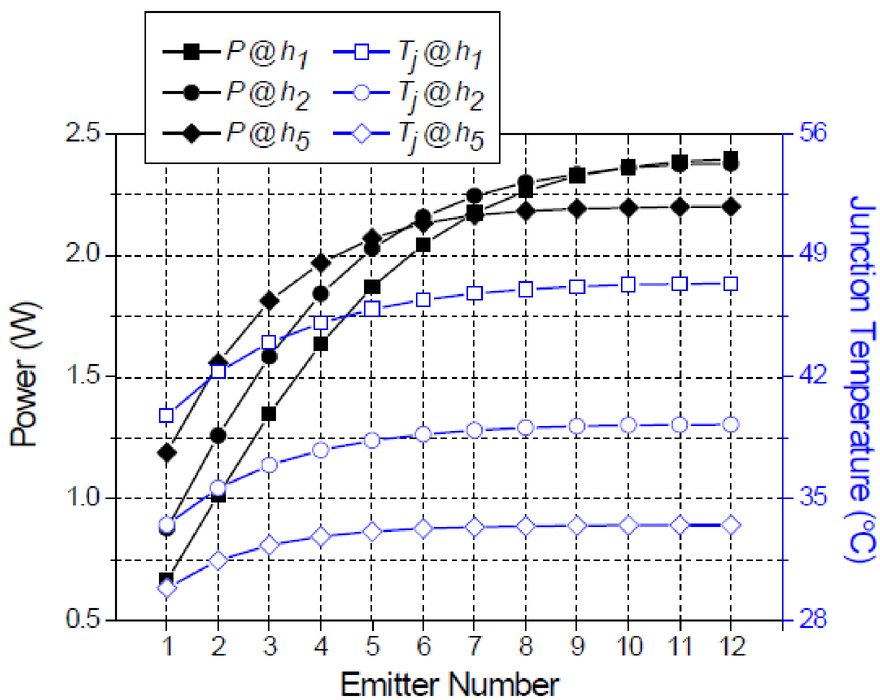

Figure 63: Junction Temperature and Power of each Emitter in the Left Half of the LD Array at h_1, h_2, and h_5
(I_f = 80 A, and T_{inlet} = 20 °C)

3.3.5 Summary

A novel method was proposed to predict the SPDs of individual emitters in high power LD arrays. The objective was achieved by deconvoluting the SPD of an LD array while taking into account the thermal cross talk effect as well as the current competition effect. A commercial water-cooled LD array was used to implement the proposed method. The SPDs of individual emitters in the LD array were deconvoluted successfully at different cooling conditions. The results indicated very strong coupling between the junction temperature and power distributions. The comparison between the predicted SPD and the experimentally measured SPD showed an excellent agreement in both shape and magnitude, which corroborated the validity of the proposed method. The proposed method can be employed to improve the packaging structure and/or to optimize the cooling conditions for enhanced pumping efficiency of laser diode pumped solid-state lasers and fiber lasers.

3.4 Lifetime Prediction of LD/Microcooler Subassembly based on PoF model

In this section, the crack propagation in the die attach caused by the thermal fatigue and its effect on the SPD change are demonstrated for the PoF-based reliability assessment.

3.4.3 Crack Propagation Model of Die Attach for LD Bar

The viscoplastic behavior of solders should be used to predict the crack propagation in the die attach. The viscoplastic behavior of solders can be modeled by Anand's model [65]. It is a unified model determined directly by combining both rate-dependent (creep) and rate-independent inelastic strains (plasticity) into a viscoplastic strain term. Anand's model requires inputs for the nine constants and can be expressed as:

$$\dot{\varepsilon}^{p} = A\exp\left(-\frac{Q}{k\theta}\right)\left\{\sinh\left(\xi\frac{\sigma}{s}\right)\right\}^{\frac{1}{m}}$$

$$\dot{s} = h_0\left(1-\frac{s}{s^{*}}\right)^{a}\dot{\varepsilon}^{p}$$

$$s^{*} = \hat{s}\left\{\frac{\varepsilon^{p}}{A}\exp\left(\frac{Q}{k\theta}\right)\right\}^{n}$$

More technical details of the Anand constants can be found in Ref. [65]. Table 8 shows constants of Anand model for SAC305.

Table 8. Constant of Anand Model for Indium and SAC305

Parameter	Name	Sn3.0Ag0.5Cu [68]
A (1/s)	Pre-exponential factor	17.994
Q/k (1/K)	Activation energy/Universal gas constant	9970
ξ	Multiplier of stress	0.35
m	Strain rate sensitivity of stress	0.153
h0 (MPa)	Hardening/softening constant	1525.98
a	Strain rate sensitivity of hardening or softening	1.69
S0 (MPa)	Initial value of the initial variable	2.15
Ŝ (MPa)	Coefficient for deformation resistance value	2.536
n	Strain rate sensitivity of saturation value	0.028

Darveaux's approach (energy-based approach) has been widely accepted to predict the crack propagation of solders caused by the thermal fatigue [69]. The energy-based approach utilizes a finite element analysis to determine the inelastic strain energy density accumulated per each thermal cycle. The strain energy density and the crack growth data are used to predict the number of cycles to initiate and propagate the cracks through a solder joint. The model can be expressed as:

$$N_0 = K_1(\Delta W_{ave})^{K_2}$$
$$\frac{da}{dN_p} = K_3(\Delta W_{ave})^{K_4}$$

where N_0 is the crack initial life, N_p is the crack propagation life, a is the length of crack. The model constants of K_1, K_2, K_3, and K_4 are determined empirically from the test data. In the model, the lifetime becomes the sum of the crack initial life and the crack propagation life ($N = N_0 + N_p$). ΔW_{ave} is the average inelastic strain energy density, which can be calculated using Anand's model [65]. The averaged inelastic energy density change per thermal cycling, ΔW_{ave}, is defined as

$$\Delta W_{ave} = \frac{\sum_{elem} \Delta W_{elem} V_{elem}}{\sum_{elem} V_{elem}}$$

where ΔW_{elem} is the inelastic strain energy density change per thermal cycling of each element in the finite element model; and V_{elem} is the volume of each element.

In the model, the lifetime becomes the sum of the crack initial life and the crack propagation life ($N_f = N_0 + N_p$). The life time can be expressed as

$$N_f = K_1(\Delta W_{ave})^{K_2} + \frac{a}{K_3(\Delta W_{ave})^{K_4}}$$

Table 9 shows the crack growth correlation constants of the SAC305 determined based on the experimental results and numerical simulations, respectively.

Table 9. Fatigue Constants for SAC305 [70]

K_1 (cycles/MPa^{K2})	K_2	K_3 (m/cycle/MPa^{K4})	K^4
37.97	-2.80	1.4E-6	1.16

Figure 64 shows the FEM model of the half model and the die attach. The die attach has thickness of 5 µm and was simulated by using three layers of elements.

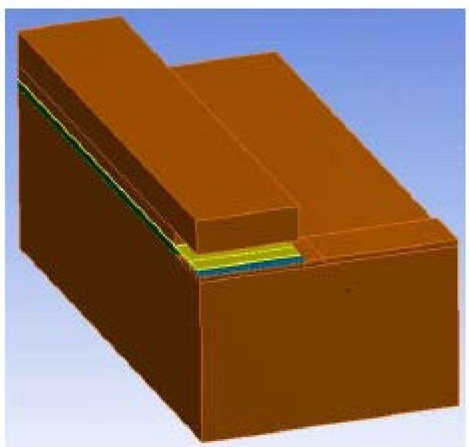

(a)

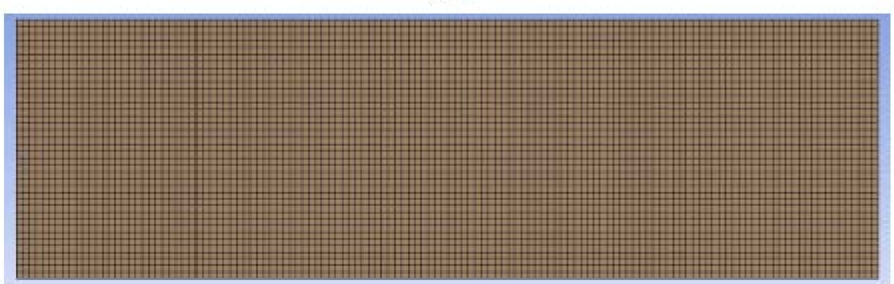

(b)

Figure 64: (a) Half Model for the Solder Model and (b) Top View of the Die Attach

Figure 65 shows the thermal cycle loading conditions used in the study. The average inelastic strain energy density was calculated subjected to the passive thermal cycles with the military standard condition (-55°C to 85°C, ramp rate 10°C/min, dwell time 15 minutes, 58 min/cycle) [66].

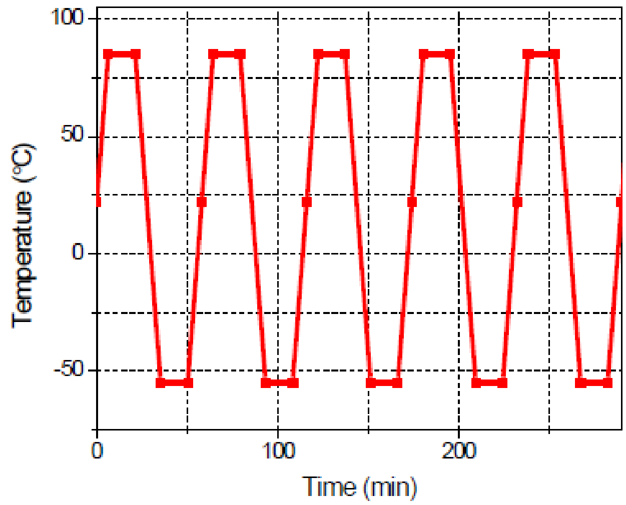

Figure 65: Thermal Cycle Loading Conditions

Three different crack lengths of 0.25, 0.75, and 1.25 mm were considered. Figure 66 shows the three crack lengths from the edge of the die attach. The crack length 0.25 mm does not reach the first edge emitter. The crack length of 0.75 mm penetrates the first edge emitter. The crack length of 1.25 mm penetrates the first and the second edge emitters. Figure 67 shows the plastic energy density distribution of the die attach at the end of the 4th cycle used for fatigue life calculation.

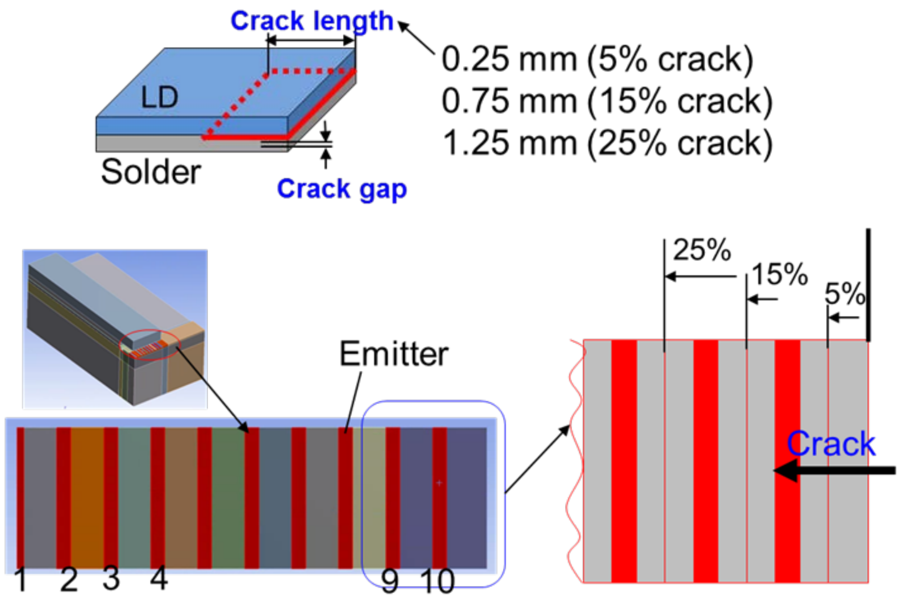

Figure 66: Crack Length Information from the Edge of the Die Attach

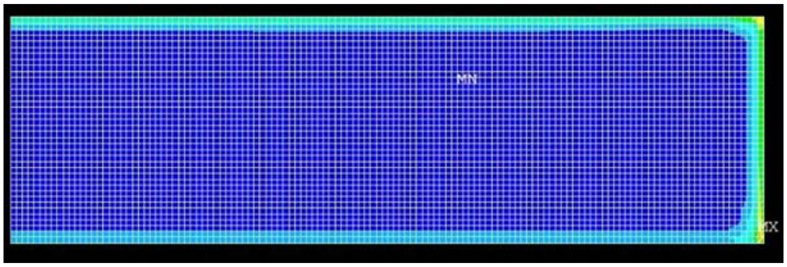

Figure 67: Plastic Energy Density Result at 4th Cycle

Table 10 shows the number of cycles required for the three crack lengths. The number of cycles to initiate the crack (N_i) was 3217. The total number of cycles (N_f) for the SAC305 was 4340, 6596, and 8832 for the crack length of 0.25, 0.75, and 1.25 mm, respectively.

Table 10. Cycles for Crack Length with SAC305

Elements for average	Averaged accumulated Strain Energy Density per Cycle ΔW (MPa)	Crack length (mm)	N_i (Cycles)	N_p (Cycles)	N_f (Cycles)
Whole top layer	0.205	0.25	3217	1123	4340
		0.75	3217	3379	6596
		1.25	3217	5615	8832

3.4.2 Junction Temperature Distribution Change from Crack Propagation

The junction temperature distribution was predicted for 4 different cases: the crack lengths of 0 (without crack), 0.25, 0.75, and 1.25 mm. Figure 68 shows the loading and boundary conditions used in the thermal model. A total heat power of 30 W was applied on the emitters of the half model, and the bottom surface temperature of an LD device was set to be 25°C. The crack area was replaced with air to simulate the crack propagation. The simulation only considered the heat conduction due to the negligible heat convection and radiation.

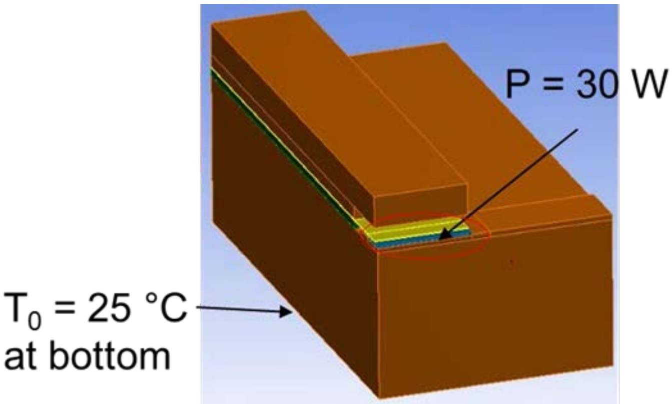

Figure 68: Loading and Boundary Conditions for the Thermal Model

Figure 69 shows (a) a 3-D representative view of the temperature distribution of the half model and (b) the junction temperature distributions of emitters without the crack and with the 1.25 mm crack in the die attach. The junction temperature decreases from the center to the edge emitter; it also does from the emitting side to the back end. The significant junction temperature increase appears at the edge emitters when the cracks are formed.

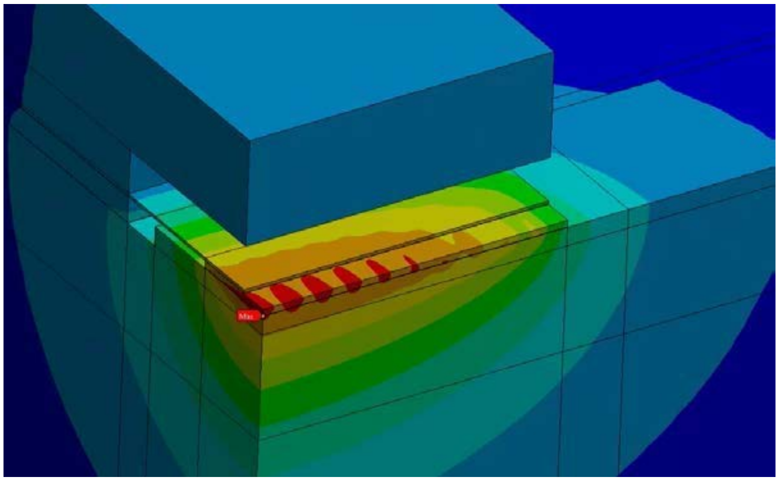

(a)

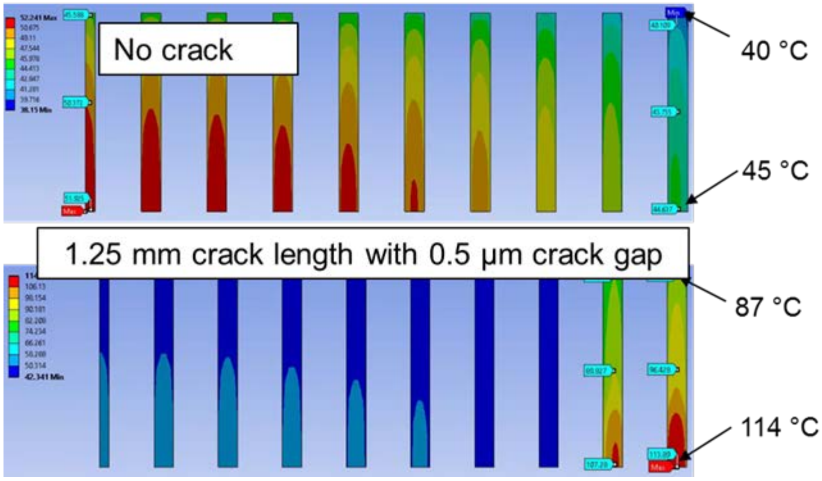

(b)

Figure 69: (a) 3-D Representative View of the Temperature Distribution of the Half Model and (b) the Junction Temperature Distributions of Emitters without the Crack and with the 1.25 mm Crack in the Die Attach

The average junction temperature of each emitter without a crack is compared with those with different crack lengths in Figure 70, where the only left half is shown due to the symmetry. The average junction temperatures remain virtually unchanged over the center half of emitters and then drops toward the edge emitter. As expected, the junction temperature increased significantly at edge emitters with the cracks.

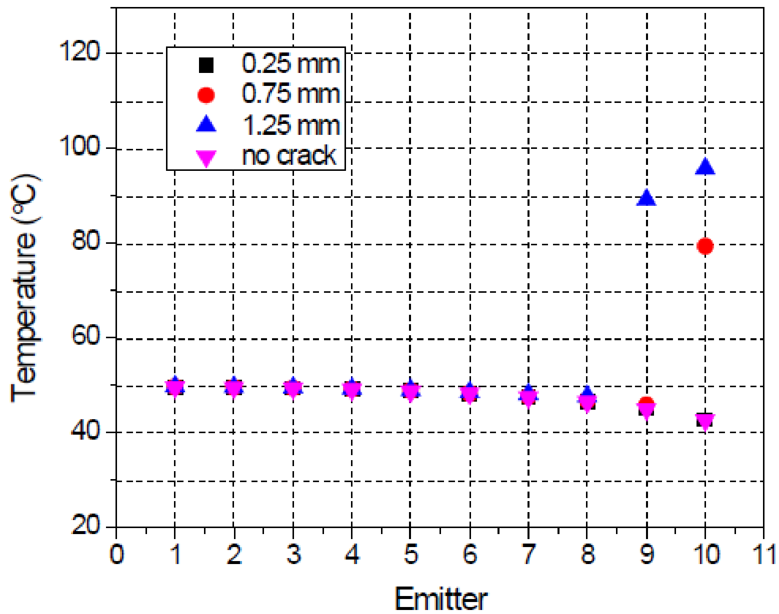

Figure 70: Average Junction Temperature of each Emitter in the Half of the LD Array without a Crack and with different Crack Lengths

3.4.3 SPD Change from Junction Temperature Distribution Change

The SPD change was predicted for 4 different cases: the crack lengths of 0 (without crack), 0.25, 0.75, and 1.25 mm. The junction temperature distribution obtained from the thermal model was used as an input for the SPD estimation.

Three Gaussian functions were used to fit the normalized SPD of the center emitter. The results are shown in Figure 71 and the Gaussian fitting parameters are shown in Table 11.

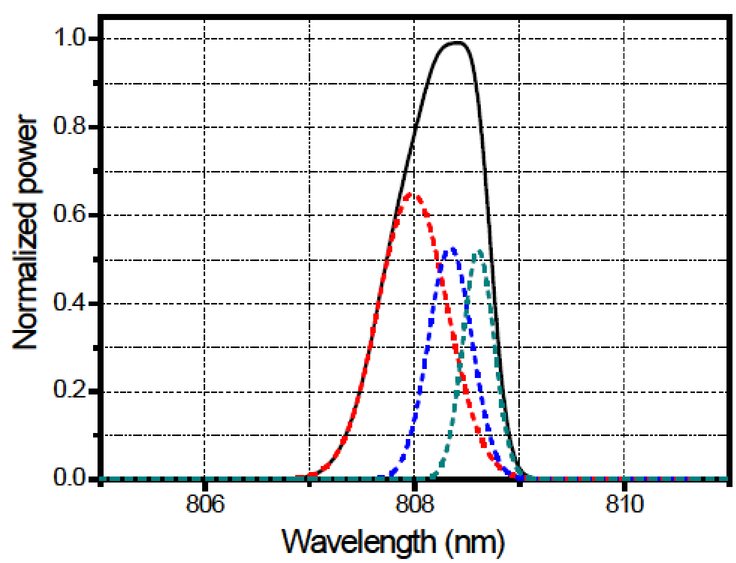

Figure 71: SPD Deconvolution of the Normalized SPD of the Center Emitter using Three Gaussian Functions

Table 11. Three Gaussian Functions used to define the Normalized SPD of the Center Emitter

Λ_1 (nm)	Λ_2 (nm)	Λ_3 (nm)
807.980	808.338	808.608
W_1 (nm)	W_2 (nm)	W_3 (nm)
0.463	0.285	0.200
A_1	A_2	A_3
0.655	0.541	0.549

Figure 72 shows the normalized SPDs of the LD array measured with different crack lengths (0.25, 0.75, and 1.25 mm). The wavelength coefficient was 0.3 nm/K and the coefficient of current the competition was 5.9. When the crack size is less than 0.25 mm, the total SPD of LD bar is nearly the same because of the negligible temperature change. It should be noted that the edge emitter works even when the crack is propagated because the emitters are connected in parallel.

The center emitter of the SPD also showed significant shift due to the junction temperature change and the current competition effect. When the crack penetrates to one emitter (the 10th emitter), the emitter temperature increases dramatically. Most of the power will be loaded at the emitter with the crack due to the current competition. Based on this study, it is expected that there is no gradual degradation due to the thermal fatigue, but the fiber laser will be failed catastrophically once the crack penetrates the first edge emitter due to the significant SPD shift (coupling efficiency).

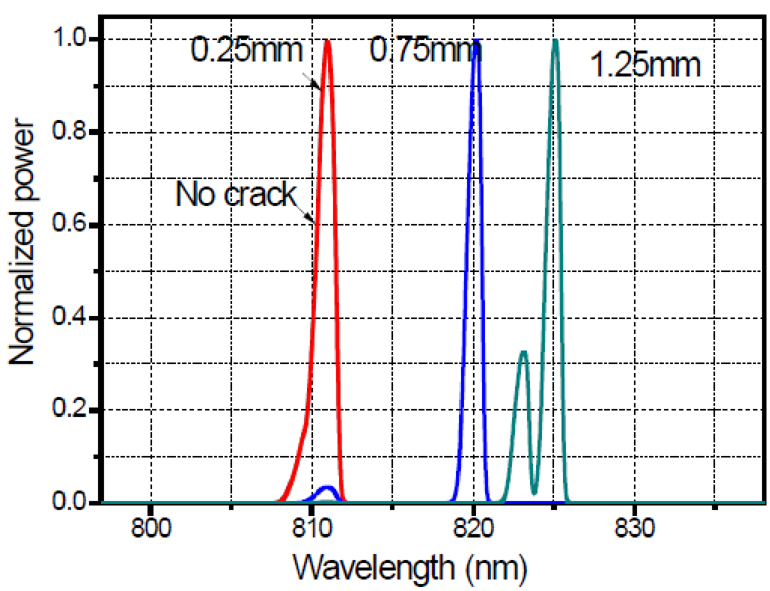

Figure 72: Normalized SPDs of the LD Array Measured with different Crack Lengths *(0.25, 0.75, and 1.25 mm)*

3.4.4 Summary

The crack propagation in the die attach due to the thermal fatigue and its effect on the spectral power distribution change were demonstrated for the PoF-based reliability assessment.

3.5 References for Part II

[1] S. Krishnamurthy and Y. Peles, "Flow boiling of water in a circular staggered micro-pin fin heat sink," International Journal of Heat and Mass Transfer, vol. 51, pp. 1349-1364, 2008.

[2] A. Reeser, et al., "High quality flow boiling heat transfer and pressure drop in microgap pin fin arrays," International Journal of Heat and Mass Transfer, vol. 78, pp. 974-985, 2014.

[3] S. L. Qi, et al., "Flow boiling of liquid nitrogen in micro-tubes: Part II – Heat transfer characteristics and critical heat flux," International Journal of Heat and Mass Transfer, vol. 50, pp. 5017-5030, 2007.

[4] S. Murata and H. Nakada, "Adding a heat bypass improves the thermal characteristics of a 50 μm spaced 8-beam laser diode array, Journal of Applied Physics 72, pp. 2514-2516, 1992.

[5] B. Siegal, "Practical Considerations in High Power LED Junction Temperature Measurements," in Electronics Manufacturing and Technology, 31st International Conference on, 2006, pp. 62-66.

[6] A. Kozlowska and A. Malag, "Investigations of transient thermal properties of conductively cooled diode laser arrays operating under quasicontinuous-wave conditions," Microelectronics Reliability, vol. 46, pp. 2079-2084, 2006.

[7] H. Y. Ryu, et al., "Measurement of junction temperature in GaN-based laser diodes using voltage-temperature characteristics," Applied Physics Letters, vol. 87, pp. 093506-1-3, 2005.

[8] J. Kim, et al., "Temperature Dependent Thermal Properties of a GaN-based Laser D Analyzed by an Electrical Method," AIP Conference Proceedings, vol. 1399, pp. 99-100, 2011.

[9] M. X. Feng, et al., "Thermal characterization of GaN-based laser diodes by forward-voltage method," Journal of Applied Physics, vol. 111, pp. 094513-1-4, 2012.

[10] Y. Qiao, et al., "The thermal properties of AlGaAs/GaAs laser diode bars analyzed by the transient thermal technique," Solid-State Electronics, vol. 79, pp. 192-195, 2013.

[11] P. Wen, et al., "High accuracy thermal resistance measurement in GaN/InGaN laser diodes," Solid-State Electronics, vol. 106, pp. 50-53, 2015.

[12] Y. Xi and E. F. Schubert, "Junction-temperature measurement in GaN ultraviolet light-emitting diodes using diode forward voltage method," Applied Physics Letters, vol. 85, pp. 2163-2165, 2004.

[13] Y. G. Xi, et al., "Junction temperature in ultraviolet light-emitting diodes," Japanese Journal of Applied Physics Part 1-Regular Papers Brief Communications & Review Papers, vol. 44, pp. 7260-7266, 2005.

[14] A. Keppens, et al., "High power light-emitting diode junction temperature determination from current-voltage characteristics," Journal of Applied Physics, vol. 104, pp. 093104-1-8, 2008.

[15] S. Todoroki, et al., "Temperature distribution along the striped active region in high-power GaAlAs visible lasers," Journal of Applied Physics, vol. 58, pp. 1124-1128, 1985.

[16] K. Takahashi, et al., "Temperature measurement of GaN-based blue-violet laser diodes in operation by Raman microprobe," physica status solidi (c), vol. 4, pp. 2802-2805, 2007.

[17] M. Horiuchi, et al., "Development of junction temperature estimation system for light-emitting LED using pulsed-laser Raman scattering," Journal of Solid State Lighting, vol. 2, pp. 1-7, 2015.
[18] D. Lisak, et al., "Bonding stress and reliability of high power GaAs-based lasers," IEEE Transactions on Components and Packaging Technologies, vol. 24, pp. 92-98, 2001.
[19] G. Jiang, et al., Advanced Thermal Management Materials. New York: Springer, 2013.
[20] R. J. Quagan, "Laser Diode Heat Spreaders," Ion Beam Milling, Inc.
[21] http://www.dilas.com/.
[22] P. Perlin, et al., "Low-temperature study of current and electroluminescence in InGaN/AlGaN/GaN double-heterostructure blue light-emitting diodes," Applied Physics Letters, vol. 69, pp. 1680-1682, 1996.
[23] S. Chhajed, et al., "Junction temperature in light-emitting diodes assessed by different methods," in Proc. SPIE 5739, Light-Emitting Diodes: Research, Manufacturing, and Applications IX, 2005, pp. 16-24.
[24] D.-S. Kim, et al., "Characterization of Die-Attach Thermal Interface of High-Power Light-Emitting Diodes: An Inverse Approach," IEEE Transactions on Components, Packaging and Manufacturing Technology, vol. 5, pp. 1635-1643, 2015.
[25] J. Bird, Electrical Circuit Theory and Technology. New York: Routledge, 2010.
[26] K. S. S. Kumar, Electric Circuit Analysis. New Delhi: Pearson, 2013.
[27] M. Glavanovics and H. Zitta, "Thermal destruction testing: An indirect approach to a simple dynamic thermal model of smart power switches," in Proceedings of the 27th European Solid-State Circuits Conference, 2001, pp. 221-224.
[28] H. Pape, et al., "Development of a standard for transient measurement of junction-to-case thermal resistance," Microelectronics Reliability, vol. 52, pp. 1272-1278, 2012.
[29] F. Daiminger, et al., "Experimental investigations on the offset correction of transient cooling curves of light emitting diodes based on JESD51-14 and simple semi-empirical approximations," Microelectronics Journal, vol. 46, pp. 1208-1215, 2015.
[30] EIA/JEDEC, "Transient Dual Interface Test Method for the Measurement of the Thermal Resistance Junction to Case of Semiconductor Devices with Heat Flow Through a Single Path," JESD51-14, p. 46, 2010.
[31] Q. Shan, et al., "Analysis of thermal properties of GaInN light-emitting diodes and laser diodes," Journal of Applied Physics, vol. 108, pp. 084504-1-8, Oct 15 2010.
[32] V. Szekely, "A new evaluation method of thermal transient measurement results," Microelectronics Journal, vol. 28, pp. 277-292, 1997.
[33] Y.-J. Lee, et al., "Determination of Junction Temperature in InGaN and AlGaInP Light-Emitting Diodes," IEEE Journal of Quantum Electronics, vol. 46, pp. 1450-1455, 2010.
[34] R. O. Carlson, et al., "Thermal Conductivity of GaAs and GaAs1−xPx Laser Semiconductors," Journal of Applied Physics, vol. 36, pp. 505-507, 1965.
[35] E. Suhir, et al., Micro- and Opto-Electronic Materials and Structures: Physics, Mechanics, Design, Reliability, Packaging: Volume I Materials Physics - Materials Mechanics. Volume II Physical Design - Reliability and Packaging: Springer US, 2007.
[36] J. W. Orton and T. Foxon, Molecular Beam Epitaxy: A Short History: Oxford University Press, 2015.
[37] D.-S. Kim and B. Han, "Effect of junction temperature on heat dissipation of high power light emitting diodes," Journal of Applied Physics, vol. 119, pp. 125104-1-8, 2016.

[38] P. A. Crump, et al., "85% Power Conversion Efficiency 975-nm Broad Area Diode Lasers at - 50°C, 76 % at 10°C," in Conference on Lasers and Electro-Optics/Quantum Electronics and Laser Science Conference and Photonic Applications Systems Technologies, Long Beach, California, 2006, p. JWB24.
[39] Y. P. Varshni, "Temperature dependence of the energy gap in semiconductors," Physica, vol. 34, pp. 149-154, 1967.
[40] L. Fan, et al., "Reliable high-power long-pulse 8XX-nm diode laser bars and arrays operating at high temperature," in Proc. SPIE 7918, High-Power Diode Laser Technology and Applications IX, 2011, pp. 791805-1-7.
[41] M. H. Hu, et al., "Transient and static thermal behavior of high-power single-mode semiconductor lasers," in Proc. SPIE 4905, Materials and Devices for Optical and Wireless Communications, 2002, pp. 32-36.
[42] H. Liu, et al., Packaging of High Power Semiconductor Lasers: Springer, 2014.
[43] G. Treusch, et al., "Reliability of water-cooled high-power diode laser modules," in Proc. SPIE 5711, High-Power Diode Laser Technology and Applications III, San Jose, CA, 2005, pp. 132-141.
[44] R. Feeler, et al., "Next-generation microchannel coolers," in Proc. SPIE 6876, High-Power Diode Laser Technology and Applications VI, San Jose, CA, 2008, pp. 687608-1-8.
[45] C. K. Amuzuvi, et al., "The impact of temperature and strain-induced band gap variations on current competition and emitter power in laser bars," Applied Physics Letters, vol. 98, p. 241108, Jun 13 2011.
[46] S. Bull, et al., "Emulation of the operation and degradation of high-power laser bars using simulation tools," Semiconductor Science and Technology, vol. 27, p. 094012, Sep 2012.
[47] R. Diehl, High-Power Diode Lasers: Fundamentals, Technology, Applications: Springer, 2000.
[48] B. M. Song and B. Han, "Spectral power distribution deconvolution scheme for phosphor-converted white light-emitting diode using multiple Gaussian functions," Applied Optics, vol. 52, pp. 1016-1024, Feb 10 2013.
[49] B. M. Song and B. Han, "Analytical/Experimental Hybrid Approach Based on Spectral Power Distribution for Quantitative Degradation Analysis of Phosphor Converted LED," Ieee Transactions on Device and Materials Reliability, vol. 14, pp. 365-374, Mar 2014.
[50] X. Huawei, "Structural Design and Epitaxial Growth of 852nm Laser Diode," Ph.D., Graduate University of Chinese Academy of Sciences, Jilin, 2012.
[51] D. S. Kim, et al., "Method for predicting junction temperature distribution in a high-power laser diode bar," Applied Optics, vol. 55, pp. 7487-7496, Sep 2016.
[52] H. Kissel, et al., "A comprehensive reliability study of high-power 808 nm laser diodes mounted with AuSn and indium," presented at the High-Power Diode Laser Technology and Applications VI, 2008.
[53] R. O. Carlson, et al., "Thermal Conductivity of GaAs and GaAs1-XPx Laser Semiconductors," Journal of Applied Physics, vol. 36, pp. 505-507, 1965.
[54] J. S. Blakemore, "Semiconducting and Other Major Properties of Gallium-Arsenide," Journal of Applied Physics, vol. 53, pp. R123-R181, 1982.
[55] M. Pecht, et al., Electronic Packaging Materials and Their Properties: Taylor & Francis, 1998.
[56] W. W. Sheng and R. P. Colino, Power Electronic Modules: Design and Manufacture: CRC Press, 2004.

[57] M. Szymanski, "Calculation of the cross-plane thermal conductivity of a quantum cascade laser active region," Journal of Physics D-Applied Physics, vol. 44, p. 085101, Mar 2 2011.
[58] J. W. Orton and T. Foxon, Molecular Beam Epitaxy: A Short Story: Oxford University Press, 2015.
[59] X. S. Liu, et al., "Study of the mechanisms of spectral broadening in high power semiconductor laser arrays," presented at the 58th Electronic Components & Technology Conference, 2008.
[60] L. Fan, et al., "Reliable high-power long-pulse 8XX-nm diode laser bars and arrays operating at high temperature," presented at the High-Power Diode Laser Technology and Applications IX, 2011.
[61] E. Farsad, et al., "Experimental parametric investigation of temperature effects on 60W-QCW diode laser," World Acad. Sci. Eng. Technol, vol. 59, pp. 1190-1196, 2011.
[62] X. S. Liu, et al., "Thermal management strategies for high power semiconductor pump lasers," Ieee Transactions on Components and Packaging Technologies, vol. 29, pp. 268-276, Jun 2006.
[63] P. A. Crump, et al., "85% Power Conversion Efficiency 975-nm Broad Area Diode Lasers at - 50°C, 76 % at 10°C," presented at the Conference on Lasers and Electro-Optics/Quantum Electronics and Laser Science Conference and Photonic Applications Systems Technologies, Long Beach, California, 2006.
[64] D. Schroder, et al., "Improved laser diode for high power and high temperature applications," presented at the High-Power Diode Laser Technology and Applications VII, San Jose, CA, United states, 2009.
[65] L. Anand, “Constitutive equations for the rate-dependent deformation of metals at elevated temperatures,” ASME Journal of Engineering Materials and Technology, Vol.104, No. 1, pp.12-17, 1982.
[66] MIL-STD-883E 1010.7
[67] Chang, Rui Wu, and F. Patrick Mccluskey. "Constitutive relations of indium in extreme-temperature electronic packaging based on Anand model."Journal of Electronic Materials 38.9 (2009): 1855-1859.
[68] K. Mysore, G. Subbarayan, V. Gupta and R. Zhang, Constitutive and aging behavior of Sn3.0Ag0.5Cu solder alloy, IEEE Trans. Electronics Packaging Manufacturing, 32 (4) (2009) 221-232.
[69] Darveaux R., “Effect of simulation methodology on solder joint crack growth correlation,” in Proceeding of 50th Electronic Components and Technology Conference, pp.1048-158, 2000.
[70] Motalab, Mohammad, et al. "Correlation of reliability models including aging effects with thermal cycling reliability data." Electronic Components and Technology Conference (ECTC), 2013 IEEE 63rd. IEEE, 2013.
[71] Rui Wu Chang, “Influence of cryogenic temperature and microstructure on fatigue failure of indium solder joint”, Doctor of Philosophy, University of Maryland, 2008

LIST OF ABBREVIATIONS, ACRONYMS, AND SYMBOLS

ACRONYM	DESCRIPTION
AFRL	Air Force Research Laboratory
COP	coefficient of performance
CTE	coefficient of thermal expansion
DAQ	data acquisition module
FWHM	full width at half maximum
HTC	heat transfer coefficient
LD	laser diode
LED	light emitting diode
MOSFET	metal-oxide-semiconductor field-effect transistor
PoF	physics-of-failure
SPD	spectral power distribution
TEC	thermoelectric cooler/cooling
TIM	thermal interface material